QUANTIFYING THE IMPACTS OF INUNDATED LAND AREA ON STREAMFLOW AND CROP DEVELOPMENT

by

Stuart D. Smith

A Dissertation

Submitted to the Faculty of Purdue University

In Partial Fulfillment of the Requirements for the degree of

Doctor of Philosophy

School of Agricultural and Biological Engineering

West Lafayette, Indiana

May 2021

THE PURDUE UNIVERSITY GRADUATE SCHOOL
STATEMENT OF COMMITTEE APPROVAL

Dr. Laura C. Bowling, Co-Chair

Department of Agronomy

Dr. Keith A. Cherkauer, Co-Chair

Department of Agricultural and Biological Engineering

Dr. Katy M. Rainey

Department of Agronomy

Dr. Andrew W. Wood

Department of Agricultural and Biological Engineering

Approved by:

Dr. Nathan Mosier

ACKNOWLEDGMENTS

This research was supported by the National Aeronautics and Space Administration and United Stated Department of Agriculture. The Planet Education and Research Program provided access to the RapidEye data.

TABLE OF CONTENTS

LIST OF TABLES

LIST OF FIGURES

ABSTRACT

The presented work quantifies the impacts of inundated land area (ILA) on streamflow and crop development in the Upper Midwest, which is experiencing a changing climate with observed increases in temperature and precipitation. Quantitative information is needed to understand how upland and downstream stakeholders are impacted by ILA; yet the temporal and spatial extent of ILA and the impact of water storage on flood propagation is poorly understood. Excess water in low gradient agricultural landscapes resulting in ILA can have opposing impacts. The ILA can negatively impact crop development causing financial loss from a reduction or total loss in yield while conversely, ILA can also benefit downstream stakeholders by preventing flood damage from the temporary surface storage that slows water movement into channels. This research evaluates the effects of ILA on streamflow and crop development by leveraging the utility of remotely sensed observations and models.

The influence of ILA on streamflow is investigated in the Red River basin, a predominantly agricultural basin with a history of damaging flood events. An inundation depth-area (IDA) parameterization was developed to parameterize the ILA in a hydrologic model, the Variable Infiltration Capacity (VIC) model, using remotely sensed observations from the MODIS Near Real-Time Global Flood Mapping product and discharge data. The IDA parameterization was developed in a subcatchment of the Red River basin and compared with simulation scenarios that did and did not represent ILA. The model performance of simulated discharge and ILA were evaluated, where the IDA parameterization outperformed the control scenarios. In addition, the simulation results using the IDA parameterization were able to explain the dominant runoff generation mechanism during the winter-spring and summer-fall seasons. The IDA parameterization was extended to the Red River basin to analyze the effects of ILA on the timing and magnitude of peak flow events where observed discharge revealed an increasing trend and magnitude of summer peak flow events. The results also showed that the occurrence of peak flow events is shifting from unimodal to bimodal structure, where peak flow events are dominant in the spring and summer seasons. By simulating ILA in the VIC model, the shift in occurrence of peak flow events and magnitude are better represented compared to simulations not representing ILA.

The impacts of ILA on crop development are investigated on soybean fields in west-central Indiana using proximal remote sensing from unmanned aerial systems (UASs). Models sensitive to ILA were developed from the in-situ and UAS data at the plot scale to estimate biomass and percent of expected yield between the R4-R6 stages at the field scale. Low estimates of biomass and percent of expected yield were associated with mapped observations of ILA. The estimated biomass and percent of expected yield were useful early indicators to identify soybean impacted by excess water at the field scale. The models were applied to satellite imagery to quantify the impacts of ILA on soybean development over larger areas and multiple years. The estimated biomass and percent of expected yield correlated well with the observed data, where low model estimates were also associated with mapped observations of ILA and periods of excessive rainfall. The results of the work link the impacts of ILA on streamflow and crop development, and why it is important to quantify both in a changing climate. By representing ILA in hydrologic models, we can improve simulated streamflow and ILA and represent dominant physical process that influence hydrologic responses and represent shift and seasonal occurrence of peak flow events. In the summer season, where there is an increased occurrence of peak flow events, it is important to understand the impacts of ILA on crop development. By quantifying the impacts of ILA on soybean development we can analyze the spatiotemporal impacts of excess water on soybean development and provide stakeholders with early assessments of expected yield which can help improvement management decisions.

1. INTRODUCTION

Low gradient agricultural areas often experience extensive ponding of water in surface depressions following snowmelt and extreme rain events. These impacts may be beneficial or adverse to stakeholders depending on conditions and perspective. Agricultural producers may be adversely impacted by depressional water storage on their land, since excess water obstructs plant development, leading to a reduction in biomass development and yield. For example, in June of 2015, excess water from heavy precipitation caused destruction to five percent of the corn and soybean in Indiana resulting in approximately $300 million in crop damage (Pack, 2015). In contrast, downstream residents and property owners adjacent to receiving streams and rivers may benefit from the temporary surface storage that slows water movement into channels. Local ponding also presents challenges to flood forecasters to accurately estimate the timing and magnitude of flood propagation for people at flood risk. In 2013, the North Central River Forecast Center had directed costs for flood mitigation in the Red River of the North to locations that were not affected by flooding. This happened because flood forecasts did not represent the impact of this depressional storage on flood propagation (NWS, 1998). Flood mitigation strategies, such as using agricultural land to temporarily store flood waters, become difficult for decision-makers to analyze and evaluate when impacts are opposing, and the information used to evaluate the impacts is not sufficient. By quantifying the integrated impacts of inundated land area (ILA) in low gradient agricultural areas, stakeholders will have a better understanding of 1) the mechanisms influencing ponded water and 2) the varying impacts of ILA on downstream flooding and crop production. Stakeholders will be able to use this further understanding as information to assess risks and evaluate agricultural water management options.

The storage and release of ponded water varies in space and time as a function of land management practices, soil moisture content, frozen soil, subsurface flow rates and evapotranspiration rates (Huffman et al., 2013; Petropoulos, 2014). The occurrence of local ponding also varies with season. In the spring and summer, high intensity and/or long duration rain events cause excess water and interflow to migrate to local surface depressions in areas with relatively low topographic variability and fills those depressions (Hansen, 2000). During the winter, depressional storage can also occur from snowmelt over frozen soils resulting in diminished infiltration capacity. Seasonal occurrences

of ILA may have a water depth of less than one meter yet expand to cover hundreds of square meters of land area, and it may remain stored on the surface up to a week or more, until it slowly drains through the subsurface or evaporates (Grimm et al., 2018; Shook et al., 2011). While agricultural producers may be impacted by occurrences of ILA in their fields during the growing season, such storage may also assist downstream stakeholders by slowing the discharge of excess water to channels resulting in lower peak flows and longer recession curves that alleviate the impact of flooding on downstream stakeholders (Huffman et al., 2013).

Agricultural water management practices such as subsurface drainage further complicate the timing and quantity of discharge in low gradient agricultural watersheds. Much of the Corn Belt contains artificial subsurface drainage that is designed to lower the water table to improve field access and growing conditions for crops in poorly drained soils (Fausey et al., 1995; Kovacic et al., 2006). Subsurface drainage is often installed in depressional areas or locations with low permeability. After high intensity or prolonged rain events, subsurface drains assist agricultural producers by removing ponded water from the surface and transporting through the subsurface to a designated outlet, such as a creek or drainage ditch. This practice makes these once flooded areas more resilient for agricultural production and reduces the occurrence of overland flow. Subsurface drainage has also been linked to increased streamflow flashiness and increased frequency of moderate flood events, however (Rutkowski, 2012).

Even with surface and subsurface drainage enhancements, agricultural producers may still be susceptible to the impacts of ILA depending on the timing and duration of a rain event, which may result in lower crop yields if it causes excess water stress to plants (Nielson, 2014). The effects of ILA on agricultural production may be to decrease crop yield or result in total crop loss in a section of a field. In cases where replanting is not an option, farmers rely on crop insurance for assistance. Agricultural producers can also repurpose unproductive cropland that can serve other benefits outside yield, especially for areas that have a high probability of inundation (Allred et al., 2003).

The influences of surface depressions and ILA on the water budget have been well studied with hydrologic models and field experiments (Darboux et al., 2002, 2005; Hansen, 2000). Hydrologic models are effective tools at simulating physical processes and quantifying the effects of surface

depressions on runoff processes (Chiu, 2013; Chu et al., 2013; Sathulur, 2008). Field experiments are effective at enhancing understanding of the physical processes involved with surface depressions (e.g., Darboux et al., 2005). Field experiments can be used to improve hydrologic models through algorithm development or parameterization using observations of critical processes. Yet acquiring field observations from an experiment is time-intensive and may also cause disturbance to the land surface through destructive sampling or construction of infrastructure for long-term monitoring. Integrating alternative forms of sampling technology is important to provide updated observations at higher spatial and temporal resolutions using non-destructive sampling procedures, such as remote sensing techniques. For example, remote sensing measurements can be used to estimate the extent of surface inundation and parameterize hydrologic models with their continuous spatial extent. But other observations, such as of weather conditions and discharge, are made at point locations with much better temporal resolution. Integrating these tools together can enhance understanding of flood propagation and impacts to stakeholders.

The extent and impacts of ILA can be evaluated at high temporal and moderate spatial resolution using remote sensing techniques from spaceborne platforms (Brakenridge et al., 2006; Nigro et al., 2014). The Moderate Resolution Imaging Spectroradiometer (MODIS) Near-Real-Time (NRT) Global Flood Mapping is a daily (2-day composite) flood product constructed using passive sensors. This flood product detects the extent of inundation at a 250 m resolution (Nigro et al., 2014). The detected flood areas can be used to assess damage and develop mitigation strategies (Brakenridge et al., 2006). A limitation with remote sensing to analyze the impacts of ILA is that optical sensors can be influenced by clouds, resulting in limited observations when ILA is occurring or requiring a multi-day composite that is not representative of the rapidly-changing current conditions in the area of interest (Nigro et al., 2014). Another limitation is the spatial resolution. ILA occurring in specific fields may not be distinguishable with moderate resolution spaceborne satellites (Chen et al., 2005), but is still an impact both on the local field and on downstream discharge.

The impacts of excess water stress on crop development and yield can be evaluated using above-ground biomass and leaf area index (LAI) (Lobell, 2013; Lobell et al., 2003; Monteith et al., 1977).

Above-ground biomass (kg/m^2) is the vegetation mass above the land surface, consisting of the stalk, leaves and seed of the plant. With conventional destructive sampling methods, biomass is measured directly after the vegetation is removed and weighed (fresh weight). Next, the biomass is dried in an oven and weighed again (dry weight). These dry weight values can be scaled to leaf and total biomass per area (m^2) using plant density, which is the average number of plants within a defined area (Han et al., 2017). Similarly, LAI (m^2/m^2), which is the total one-sided area of leaf tissue per unit ground surface area, can be measured directly using harvesting methods (Watson, 1947). Though these sampling techniques are commonly practiced, notable limitations are 1) the damaging process of collecting samples, 2) the time and expense of sample collection, and 3) the non-representativeness of samples of the total area conditions or crop types. Remote sensing has the potential to provide non-destructive sampling of larger areas over shorter times in a repeatable format that can quantify crop response to environmental stresses.

High spatial and temporal resolution monitoring are needed to analyze crop development at the field scale (Chen et al., 2005; Yilmaz et al., 2008; J. Zhang et al., 2010), because the adverse impacts of inundation can be detected in crops within two days (Griffin et al., 1988). Limitations of using remote sensing measurements to analyze crop development have been identified in both the spatial and temporal resolution of spaceborne satellites (Kross et al., 2015). Satellites with moderate spatial resolution may not be able to differentiate between fields and crop types (Chen et al., 2005). Prior research has also shown that course spatial resolution optical sensors from satellites such as MODIS have reduced sensitivity in their estimation of vegetation water content for soybean and underestimate measurements of above ground biomass (Chen et al., 2005; Yilmaz et al., 2008). In addition, high temporal resolution is needed to measure changes in the environment. Historically, high-resolution Earth sensing satellites, such as Landsat or SPOT have a temporal resolution greater than four days without considering the impact of cloud cover. In the last several years, constellations of small satellites with limited instrumentation, such as Planet's RapidEye system, have yielded the potential for daily images with resolutions of 5 meters or less. However, development of biomass estimation models for such systems still requires the collection and analysis of imagery and ground reference data for smaller field experiments. With the advent of unmanned aerial systems (UAS), field scale observations can be made daily if observation conditions permit, using proximal remote sensing. Proximal remote sensing is the indirect

measurement of an object in close proximity with a sensor (Chipman et al., 2009). Proximal remote sensing from UAS platforms provides high spatial resolution at the centimeter scale and the ability to produce near real-time updates of the crop status in a non-destructive manner.

In summary, quantitative information is needed to understand how upland and downstream stakeholders are impacted by ILA; yet the temporal and spatial extent of ILA and the impact of water storage on flood propagation is poorly understood. This gap in understanding creates errors in flood predictions and uncertainty in where to invest in flood mitigation. In order to provide enhanced streamflow and cropping information to stakeholders, tools must be adapted to better represent the effects of ILA in low-gradient, agricultural areas which are prone to surface ponding and flooding (Chu et al., 2013; USACE, 2017). The proposed work aims to better understand the impacts of ILA at different scales through model simulation, in-situ and remotely sensed observations. The knowledge gained from this research will provide better understanding of the quantitative impacts of depressional water storage on crop development and streamflow, which will provide stakeholders with more information to make informed agricultural water management decisions.

1.1 Hypotheses and Objectives

The purpose of this work is to increase our understanding of seasonal patterns in surface inundation, as well as its impacts on downstream flooding and crop development in a changing climate. Model simulation and tool development are incorporated into the work to help improve our understanding of the overall impacts of surface water storage on upland and downstream communities. The proposed work aims to test the following hypotheses:

1. Estimates of flood magnitude will be reduced by simulating land inundation processes, because surface depressions play a critical role in the volume of water reaching the channel in large river basins.
2. The seasonality of flood response has shifted in the Red River basin due to a changing climate, but this shift has been mitigated by the influence of ILA.
3. The impact of excess water stress on soybean yield is related to the above-ground biomass sensed from a UAS platform during early growth stages.

4. Quantification of above-ground biomass by spaceborne platforms can quantify impacts to crop yield at sub-field scales.

These hypotheses will be addressed through the following specific objectives:

1. Parameterize the representation of surface ponding in the Variable Infiltration Capacity (VIC) macroscale hydrologic model using remote sensing estimates of ILA.
2. Evaluate simulated seasonal trends in flood magnitude and frequency in the Red River of the North.
3. Quantify the impacts of excess water stress on soybean development based on proximal remote sensing.
4. Quantify the impacts of excess water stress on soybean development farm scale areas using satellite imagery with models developed at the field scale from UAS data.

1.2 Thesis Format

The thesis is divided into six chapters. The first chapter describes the motivation to quantify the impacts of inundated land area (ILA) on streamflow and crop development with listed hypotheses and objectives. Chapter 2 details the parameterization development to represent ILA in the Buffalo River watershed, a subcatchment of the Red River of the North basin. The model performance is evaluated using observed streamflow and ILA and is compared against two other simulation scenarios. The dominant seasonal runoff generation mechanisms are identified using the developed parameterization. A publication related to Chapter 2 is ready for submission. Chapter 3 investigates the seasonal trends and occurrence of peak flow in the Red River of the North using the developed parameterization from Chapter 2. A publication related to Chapter 3 is ready for submission. In Chapter 4, we assess the impacts of ILA on soybean development by developing crop models at the plot scale using unmanned aerial systems (UASs) in a crop rotated field in west-central Indiana. A publication has been submitted to Agricultural and Forest Meteorology and is under review. Chapter 5 expands on the analysis in Chapter 4 to quantifying soybean yield reduction from excess water over larger areas by applying the UAS models to satellite imagery. Chapter 6 provides a summary and conclusion of the work and describes future research objectives.

1.3 References

Allred, B. J., Brown, L. C., Fausey, N. R., Cooper, R. L., Clevenger, W. B., Prill, G. L., LaBarge, G. A., Thornton, C., Riethman, D. T., Chester, P. W., & Czartoski, B. J. (2003). Water table management to enhance crop yields in a wetland reservoir subirrigation system. *Applied Engineering in Agriculture*, *19*(4), 407–421.

Brakenridge, G. R., & Anderson, E. (2006). MODIS-Based Flood Detection, mapping and Measurement: The Potential for Operational Hydrological Applications. In *Transboundary Floods: Reducing Risks Through Flood Management* (pp. 1–12). Dordrecht: Kluwer Academic Publishers. https://doi.org/10.1007/1-4020-4902-1_1

Chen, D., Huang, J., & Jackson, T. J. (2005). Vegetation water content estimation for corn and soybeans using spectral indices derived from MODIS near- and short-wave infrared bands. *Remote Sensing of Environment*, *98*(2–3), 225–236. https://doi.org/10.1016/j.rse.2005.07.008

Chipman, J. ., Olmanson, L. G., & Gitelson, A. . (2009). *Remote sensing methods for lake management. Environmental Protection.*

Chiu, C.-M. (2013). Observation-Based Algorithm Development for Subsurface Hydrology in Northern Temperate Wetlands. *Journal of Chemical Information and Modeling*, *53*(9), 1689–1699. https://doi.org/10.1017/CBO9781107415324.004

Chu, X., Yang, J., Chi, Y., & Zhang, J. (2013). Dynamic puddle delineation and modeling of puddle-to-puddle filling-spilling-merging-splitting overland flow processes. *Water Resources Research*, *49*(6), 3825–3829. https://doi.org/10.1002/wrcr.20286

Darboux, F., Davy, P., & Gascuel-Odoux, C. (2002). Effect of depression storage capacity on overland-flow generation for rough horizontal surfaces: Water transfer distance and scaling. *Earth Surface Processes and Landforms*, *27*(2), 177–191. https://doi.org/10.1002/esp.312

Darboux, F., & Huang, C. (2005). Does Soil Surface Roughness Increase or Decrease Water and Particle Transfers? *Soil Science Society of America Journal*, *69*(3), 748. https://doi.org/10.2136/sssaj2003.0311

Fausey, N. R., Brown, L. C., Belcher, H. W., & Kanwar, R. S. (1995). Drainage and Water Quality in Great Lakes and Cornbelt States. *Journal of Irrigation and Drainage Engineering*, *121*(March 2015), 427–435. https://doi.org/10.1061/(ASCE)0733-9437(1995)121

Griffin, J. L., & Saxton, A. M. (1988). Response of Solid-Seeded Soybean to Flood Irrigation. II. Flood Duration. *Agronomy Journal*, *80*(6), 885. https://doi.org/10.2134/agronj1988.00021962008000060009x

Grimm, K., Tahmasebi Nasab, M., & Chu, X. (2018). TWI Computations and Topographic Analysis of Depression-Dominated Surfaces. *Water*, *10*(5), 663. https://doi.org/10.3390/W10050663

Han, J., Wei, C., Chen, Y., Liu, W., Song, P., Zhang, D., Wang, A., Song, X., Wang, X., & Huang, J. (2017). Mapping above-ground biomass ofwinter oilseed rape using high spatial resolution satellite data at parcel scale under waterlogging conditions. *Remote Sensing*, *9*(3). https://doi.org/10.3390/rs9030238

Hansen, B. (2000). Estimation of surface runoff and water-covered area during filling of surface microrelief depressions. *Hydrological Processes*, *14*(November 1999), 1235–1243.

Huffman, R. L., Fangmeier, D., Elliot, W. J., & Workman, S. R. (2013). *Soil and Water Conservation Engineering* (7th ed.). American Society of Agricultural and Biological Engineers. https://doi.org/10.13031/swce.2013.f.Soil

Kovacic, D. a., Twait, R. M., Wallace, M. P., & Bowling, J. M. (2006). Use of created wetlands to improve water quality in the Midwest—Lake Bloomington case study. *Ecological Engineering*, *28*(3), 258–270. https://doi.org/10.1016/j.ecoleng.2006.08.002

Kross, A., McNairn, H., Lapen, D., Sunohara, M., & Champagne, C. (2015). Assessment of RapidEye vegetation indices for estimation of leaf area index and biomass in corn and soybean crops. *International Journal of Applied Earth Observation and Geoinformation*, *34*(1), 235–248. https://doi.org/10.1016/j.jag.2014.08.002

Lobell, D. B. (2013). The use of satellite data for crop yield gap analysis. *Field Crops Research*, *143*, 56–64. https://doi.org/10.1016/j.fcr.2012.08.008

Lobell, D. B., Asner, G. P., Ortiz-Monasterio, J. I., & Benning, T. L. (2003). Remote sensing of regional crop production in the Yaqui Valley, Mexico: Estimates and uncertainties. *Agriculture, Ecosystems and Environment*, *94*(2), 205–220. https://doi.org/10.1016/S0167-8809(02)00021-X

Monteith, J. L., & Moss, C. J. (1977). Climate and the Efficiency of Crop Production in Britain [and Discussion]. *Philosophical Transactions of the Royal Society B: Biological Sciences*, *281*(980), 277–294. https://doi.org/10.1098/rstb.1977.0140

Nielson, R. L. (2014). Flood or Ponding Damage to Corn Late in the Growing Season - Corny News Network (Purdue University). Retrieved May 1, 2018, from https://www.agry.purdue.edu/ext/corn/news/timeless/FloodDamageLateCorn.html

Nigro, J., Slayback, D., Policelli, F., & Brakenridge, G. R. (2014). *NASA/DFO MODIS Near Real-Time (NRT) Global Flood Mapping Product Evaluation of Flood and Permanent Water Detection*. Retrieved from https://floodmap.modaps.eosdis.nasa.gov/documents/NASAGlobalNRTEvaluationSummary_v4.pdf

NWS. (1998). *Service assessment and hydraulic analysis Red River of the North 1997 floods*. book, Silver Spring, MD: U.S. Dept. of Commerce, National Oceanic and Atmospheric Administration, National Weather Service.

Pack, D. J. (2015). About $300 million in Indiana crops' value lost to flooding so far - Parke County - Purdue Extension. Retrieved May 16, 2018, from https://extension.purdue.edu/Parke/pages/article.aspx?intItemID=10734

Petropoulos, G. P. (2014). *Remote sensing of energy fluxes and soil moisture content*.

Rutkowski, S. (2012). Role of Climate Variability on Subsurface Drainage and Streamflow Patterns in Agricultural Watersheds, *9*.

Sathulur, K. (2008). *The spatial distribution of water table position in northern Eurasian wetlands using the Variable Infiltration Capacity Model*. Purdue University.

Shook, K. R., & Pomeroy, J. W. (2011). Memory effects of depressional storage in Northem Prairie hydrology. *Hydrological Processes*, *25*(25), 3890–3898. https://doi.org/10.1002/hyp.8381

USACE. (2017). *Flood Risk Management and Hydrology Appendix A*.

Watson, D. J. (1947). Comparative Physiological Studies on the Growth of Field Crops: I. Variation in Net Assimilation Rate and Leaf Area between Species and Varieties, and within and between Years. *Annals of Botany*. Oxford University Press. https://doi.org/10.2307/42907002

Yilmaz, M. T., Hunt, E. R., & Jackson, T. J. (2008). Remote sensing of vegetation water content from equivalent water thickness using satellite imagery. *Remote Sensing of Environment*, *112*(5), 2514–2522. https://doi.org/10.1016/j.rse.2007.11.014

Zhang, J., Xu, Y., Yao, F., Wang, P., Guo, W., Li, L., & Yang, L. (2010). Advances in estimation methods of vegetation water content based on optical remote sensing techniques. *Science China Technological Sciences*, *53*(5), 1159–1167. https://doi.org/10.1007/s11431-010-0131-3

2. PARAMETERIZING DEPRESSIONAL STORAGE AND EVALUATING STREAMFLOW RESPONSE IN LOW GRADIENT AGRICULTURAL AREAS

Abstract

Depressional storage of water in low gradient agricultural areas influences the storage and release of water to nearby channels. During peak flow events, the inundated land area (ILA) creates challenges to flood forecasts that do not represent the impact of this depressional storage on flood propagation in hydrologic models, thereby increasing uncertainty in the timing and magnitude of peak flow events. Parameterizing the temporary storage of ILA can improve prediction of the timing and magnitude of streamflow response and enhance our understanding of flood propagation and associated runoff generation mechanisms. A methodology to parameterize the depth-area relationship of ILA using remotely sensed and in-situ observations is introduced and implemented in the Variable Infiltration Capacity (VIC) model. The parameterization methodology is tested in a subcatchment of the Red River basin and compared with different parameterizations representing and not representing depressional storage. The objectives of the study are to: (1) Develop a consistent and updatable parameterization methodology to represent the influence of ILA on streamflow using accessible remotely sensed observations and in-situ observations; (2) Evaluate the ability of alternative parameterizations to reproduce observed streamflow and ILA using statistical measures; (3) Explore simulated runoff generation mechanisms within the Buffalo River watershed and (4) Integrate the ILA algorithm into the enhanced NASA Land Information System - based Variable Infiltration Capacity (LIS-VIC) model. The adaptable parameterization to represent ILA has marked improvement of simulated streamflow and ILA and has the utility to represent the seasonal occurrence of peak flow events.

2.1 Introduction

From 2000 to 2013, the Red River basin of the North has experienced flood damages in all but two years, including 100-year and 500-year flood levels within the last decade. Floods in the Red River basin have resulted in billions of dollars in damage to infrastructure and agricultural productivity, where compounding variables such as inundated land area (ILA), changes in agricultural drainage

practices and climate change have made hydrologic modeling and flood forecasting challenging in the basin (Commission, 2011; Lakshmi, 2016; Todhunter, 2001). The basin area is over 100,000 km^2 and drains parts of three states (Minnesota, North Dakota, and South Dakota) flowing north through Manitoba, Canada (Pielke, 1999; USACE, 2017). The basin area is composed of low slope topography where land use is primarily agricultural and is prone to seasonal ponding. ILA presents challenges to flood forecasters to accurately estimate the timing and magnitude of flood propagation for people at flood risk. In 2013, the North Central River Forecast Center overestimated costs for flood mitigation to the Red River of the North by sending it to locations that were not affected by flooding. This happened because flood forecasts did not represent the impact of this depressional storage on flood propagation.

The spatial and temporal dynamics of ILA are important factors to consider when quantifying the land surface water budget and understanding flood propagation (Chu et al., 2013; Du et al., 2018; Sun et al., 2011). Distinct from flooding from overbank flow, ILA develops as localized flooding in depressional areas due to local rainfall excess. It may occur following a high intensity rainfall event, after extended periods of rain leading to saturated soils and/or snowmelt over frozen soils resulting in the accumulation of water within local surface depressions. The accumulated water is often less than one meter in depth yet can expand throughout the field. The ponded water may remain stored on the surface up to a week or more, until it slowly drains through the subsurface or evaporates which can damage planted crops and decrease yield in low gradient agricultural areas such as the Red River basin (Grimm et al., 2018; Shook et al., 2011).

During peak flow events, ILA influences the storage and release of water to nearby channels, which creates uncertainty in the timing and magnitude of peak flow events. This depressional storage presents challenges to flood forecasters to accurately estimate the timing and magnitude of flood propagation for people at flood risk. Yet the depressional storage is often not represented in hydrologic models (NWS, 1998; Pagano et al., 2014). For models that do represent temporary storage, parameterizing of the depth and extent of inundation is needed to accurately simulate the potential volume of water that can be stored on the land surface (Hay et al., 2018). Improving the parameterization of inundation extent and the total storage volume can help reduce the uncertainty

in hydrologic models by quantifying depressional storage on the land surface and enhancing our understanding of the effects on flood propagation.

The role of parametrization in hydrologic models is to: (1) Represent and link dominant physical processes which influence hydrologic responses, (2) Readily incorporate information from new datasets, and (3) Reflect local characteristics to provide the right answer for the right reason. Parameterization often incorporates look-up tables or physically measured values to simulate local characteristics but may not capture the spatial variability within the study region. Hay et al. (2018) highlights the importance of understanding local characteristics, since by not representing physical processes that influence hydrologic response, the "right" answer can be given for the "wrong" reasons. For example, ILA can be identified on the land surface and remotely using optical, passive and active sensors from spaceborne platforms (Grimaldi et al., 2016; Policelli et al., 2017; Watts et al., 2012). Advances in remote sensing technology, enhances the ability to incorporate spatial variability within a study region, and provide unique parameterizations for distributed hydrologic models. Not all study areas have useful in-situ observations that can be used for parameterization, and by incorporating remotely sensed observations such as surface-water extent, parameterization could be improved.

In addition to a legacy of seasonally frozen ground and in-field flooding, the Red River region is experiencing a changing climate with increased average annual temperature and precipitation, which is driving changes in land use such as increased subsurface agricultural drainage (USACE, 2015). Further research is needed to better understand the runoff mechanisms involved during peak flow events and the influence of ILA on streamflow. By parameterizing the extent of ILA into hydrologic models, improved predictions can be made of the timing and magnitude of peak flow events. The objectives of this study are to: (1) Develop a consistent and updatable parameterization methodology to represent the influence of ILA on streamflow using accessible remotely sensed observations and in-situ observations, (2) Evaluate the ability of alternative parameterizations to reproduce observed streamflow and ILA using statistical measures, and (3) Explore simulated runoff generation mechanisms within the Buffalo River watershed.

2.1.1 Site description

The Buffalo River watershed near Dilworth, MN (USGS 05062000) is the area of interest for this study. The watershed is located in the east-central uplands of the Red River basin and has a watershed area of approximately 2525 km^2. The low gradient topography slopes east to west, where the highest elevations are in the northeastern and eastern watershed causing the Buffalo River to flow northward (Figure 2.1). The land use within the watershed is predominantly cropland (66.7%) spanning the northeast, central and northwest watershed. Land use mixtures of wetlands, grasslands, forest, residential/commercial and open water (33.3%) are found in the northeast and eastern portion of the watershed. Soil texture and drainage transitions from east to west, with the east predominantly well drained glacial till. The central portion of the watershed is a transition zone made of a complex mixture of silts and glacial till where the drainage ranges from well drained to poorly drained. The western portion of the watershed is poorly drained consisting of predominately clay and silt soils. Annual precipitation is approximately 635 mm. Combined with low gradient topography and poorly drained soils, this results in a high potential for saturated soil conditions makes the watershed prone to flooding (USDA-NRCS, 2018). The physical characteristics of the watershed, history of flooding and period of record of streamflow observations (1931-present) makes the Buffalo River watershed an appropriate study location to analyze the influence of ILA on streamflow. The inundation investigated in this study is the temporary storage of water on the landscape in predominately upland agricultural areas, which is in contrast to the overbank flow resulting from discharge exceeding the channel capacity that occurs along the main stem of the channel and in this region is often associated with ice jams.

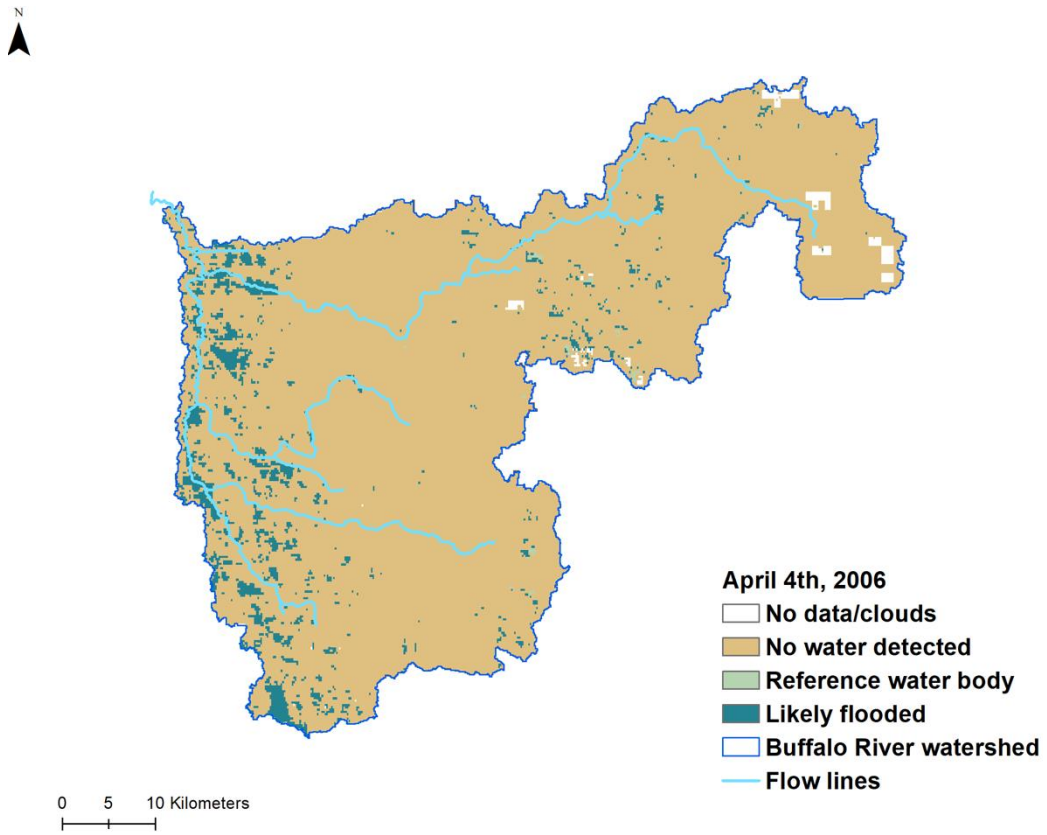

Figure 2.1: Detected flooded area along the western border of the Buffalo River watershed from the MODIS Near Real-Time (NRT) Global Flood Mapping product. The low gradient watershed is predominantly used for agriculture and is also prone to flooding. Data provided by the NASA Goddard Global Flood Mapping project, Hydrology Lab, NASA Goddard Space Flight Center, Greenbelt MD (Policelli et al., 2017).

2.2 Methods

The Variable Infiltration Capacity (VIC) model is a large-scale hydrologic model that represents surface and subsurface processes, such as lakes/wetlands and frozen soils (Bowling et al., 2010; Cherkauer et al., 2003; Liang et al., 1994). A lake and wetland class can be added to a grid cell that represents permanent or seasonally flooded areas by providing the following physical description of the lake and wetland: (1) the extent of the permanent and seasonally ponded areas, (2) the water depth of the permanent and seasonally flooded areas and (3) the width of outflow, based on the equation for flow over a broad-crested weir, from the seasonally flooded areas to the stream. In this study, permanent ponded areas such as lakes were not represented, instead only the impact of seasonally ponded areas were investigated. Prior to parameterizing the lake/wetland extent, a depth-area relationship associated with surface inundation was developed and analyzed

using remotely sensed and in-situ data. The depth-area relationship was used to better understand the storage and release of surface runoff from local surface depressions to downstream channels during flood events.

In order to describe the effects of local depressions, observed ILA and stream discharge were used to estimate a depth-area relationship. Remotely sensed observations from the Moderate Resolution Imaging Spectroradiometer (MODIS) were used to estimate inundated area and discharge data from the United States Geological Survey (USGS) gaging station for the watershed were used to estimate volume of water during peak flow events. Further details of the MODIS observations and discharge measurements are described in the following sub-sections. MODIS observations from water years 2005 to 2009 were used to identify the depth-area relationship.

2.2.1 Data sources

The MODIS Near Real-Time (NRT) Global Flood Mapping product used for this study was a daily product generated from a two-day composite (2D2OT) where the observation date was the last date of observation. A total of 3652 images were obtained from the Buffalo River watershed between water years 2005 and 2014 with a spatial resolution of 250 m. Terrain shadow masking was applied to remove false detections of pixels classified as inundated. The flood product consists of four classes with non-flooded and flooded surfaces identified (Figure 2.1). Pixels with insufficient data such as cloudy or bad data are described as Class 0. Pixels with no water detected correspond with Class 1. Pixels that coincide with the MODIS land water mask (MOD44W) are considered to be unflooded reference water bodies (Class 2; Carroll et al., 2017). Pixels that are identified beyond the reference body are likely flooded and labeled as Class 3 (Nigro et al., 2014). MODIS observations were used to estimate fractional values for each class as the ratio of total pixels associated with the class over the total number of pixels in a model grid cell with a resolution of $1/8^{th\circ}$ latitude and longitude.

Since the official designation of reference water body (Class 2) oscillated in area over time, a permanent water fraction was estimated using the 90th percentile of Class 2 area for observation dates with low cloud coverage (<10%). Pixels were classified as inundated land area by calculating the difference between the MODIS total water fraction (Class 2 and Class 3) and the estimated

permanent water fraction. Figure 2.2 shows a time series of the fractional inundated land area for the entire Buffalo River watershed between 2005 and 2009. The percent of inundated area in the watershed ranged from 0.0 to 18% with an average of 0.3%. This study analyzed moderate to large size flood events with inundated percentage greater than 1% (Figure 2.2). High cloud coverage (Class 0-insufficient data) influenced retrievals of ILA during consecutive days which were often correlated with flood events. These events were identified and removed, as described in Section 2.2.

Discharge measurements were obtained from the Buffalo River near Dilworth (USGS 05062000) from water years 2005 to 2014 (U.S. Geological Survey, 2018). The Web-based Hydrograph Analysis Tool (WHAT) with the applied recursive digital filter method was used to separate the streamflow hydrograph into stormflow and baseflow components to analyze stormflow response with respect to the change of fractional flooded area observed from the MODIS observations (Eckhardt, 2005; Jae et al., 2005).

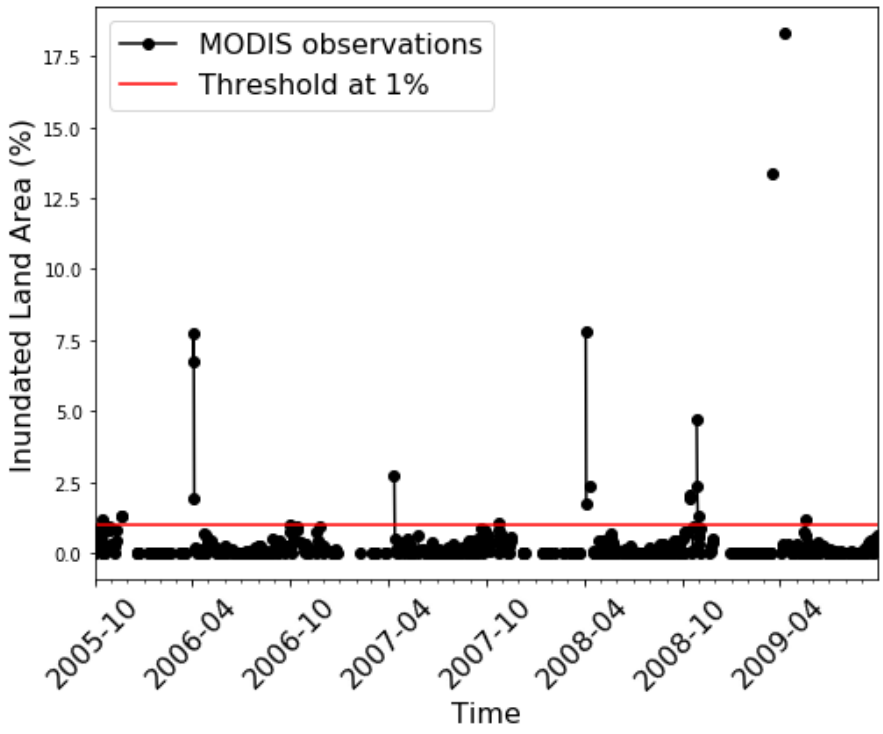

Figure 2.2: The time series of fractional flooded area for the Buffalo River watershed over the calibration period (water years 2006-2009) shows that a majority of floods are small to moderate in size. Peak flow events analyzed were above the 1% threshold.

2.2.2 Inundated depth-area parameterization

A four-step filtering process was used to identify high quality observations of surface inundation used to develop the inundated depth-area (IDA) parameterization. First, only ILA fractional values greater than 1% (indicated by the red line in Figure 2.2) were evaluated from the MODIS time series. Second, MODIS observations with cloud coverage greater than 30% within the watershed were removed from the analysis. Third, images that captured flooding associated with winter and spring ice jams were discarded. Ice jam floods were identified by analyzing the record notes of the discharge data and flood monitoring reports of the Red River basin. Flooding associated with ice jams occurred during the winter and spring and were often associated with days of estimated rather than measured discharge. Discharge values that were estimated during the winter (December-February) and spring (March-May), were assumed to be related to winter ice cover and spring ice jams and removed. The fourth filter applied was related to antecedent rainfall conditions. This filter was applied to improve quality of observations by assessing remotely sensed observations related to high intensity or long duration rainfall events. A seven-day antecedent rainfall threshold was used to remove data values below the precipitation threshold during the growing and dormant seasons. The seven-day antecedent threshold values used were 13 mm and 36 mm for the dormant and growing seasons, respectively.

After filters were applied, the incremental volume, V (m^3) of water stored on the landscape associated with the estimated flooded area and depth of inundation can be derived from two consecutive images from the ILA recession, as shown in equation 2.1:

$$\Delta V = \left(\frac{A_{t_1} + A_{t_1}}{2}\right) * \ (Z_{t_1} - Z_{t_1}) \tag{2.1}$$

Where A_{t_1} and A_{t_1}, were MODIS observations of inundated land area (m^2) from consecutive overpasses (t_1 and t_2), where $A_{t_2} < A_{t_1}$ and Z was the mean depth of ponded water (m) in the watershed over the period of subsequent MODIS retrievals. The depth of water is unknown but can be estimated by rearranging equation 1 and solving for the change in depth, dZ, based on the assumption that the decrease in volume stored on the surface is equal to the observed stormflow (m^3) during this period. This relationship is expressed in equation 2.2:

$$dZ = \frac{2 * \left(\int_{t_1}^{t_2} Q \, dt\right)}{\left(A_{t_1} + A_{t_2}\right)} \tag{2.2}$$

where Q is the observed fast response runoff that is assumed to be released from the total flooded area identified by MODIS (A_{t_1}) within the timeframe to estimate dZ. Here we assume that ΔV is equivalent to the accumulated Q_{t_i} between consecutive MODIS retrievals. Equation 2.2 represents the change over time in thickness of the water level (dZ) in local depressions as a depth (m) over the flooded area, which can be used to calculate the change in depth of depressional storage within the watershed from the change in flooded extent from subsequent overpasses.

In order to isolate the cumulative depth of ponded water for increasing ponded area A, it is necessary to normalize dZ by the change in flooded extent ($dA = A_{t_1} - A_{t_2}$). The dA was captured with MODIS from consecutive overpasses. A change in dA represents ponded water leaving local depressions through stormflow. The ponded depth of ILA from flood events can be calculated by integrating the gradient, $\frac{dZ}{dA}$ (m^{-1}), with respect to flooded extent, A, to get the cumulative depth of water for different flood extents.

Figure 2.3 shows this gradient (m^{-1}) and flooded area (km^2) relationship of observed events coded by the season of occurrence. Gradient values range from 2.3×10^{-11} m^{-1} to 4.0×10^{-9} m^{-1}. Inundated area ranges from 2 km^2 to 138 km^2. The largest flood in our record was a spring flood which occurred in 2006. Floods in the spring period ranged from small to large extent (6 - 138 km^2). Floods during the fall ranged from small to moderate (2 - 50 km^2). Floods during the summer were predominantly small (2 - 11 km^2).

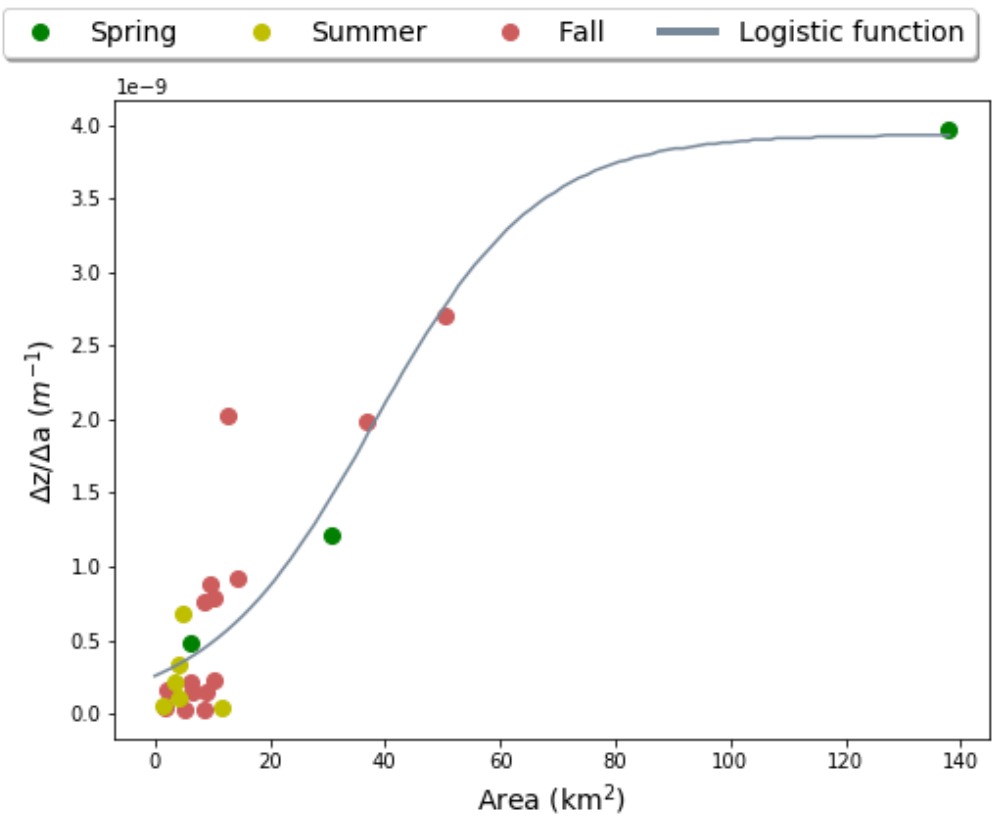

Figure 2.3: The gradient (m^{-1}) and flooded area (km^2) relationship. Colors indicate the season in which the flood events occurred, and the grey line is the logistic function fit to the observations

The ratio of change in ponded depth to change in flooded area observed for the Buffalo River watershed can be used to estimate water storage on the land surface. Fitting a logistic function to the observations resulted in the following descriptive function, where parameters are estimated by minimizing the least square error using MATLAB functions (Silva, 2020):

$$\frac{dZ}{dA}(A) = \frac{K}{1 + e^{-G(A-D)}} \tag{2.3}$$

where K is the maximum gradient, G represents the rate of growth along the curve and D is the midpoint of the curve. Fitted parameters based on the data in Figure 2.3 were found to be 3.93×10^{-9} m^{-1}, 7.01×10^{-8} m and 3.80×10^{7} m^2 for K, G and D, respectively.

In order to use the gradient function to parameterize the grid cell-based VIC model, the watershed logistic curve had to be mapped to each model grid cell in the watershed. The fitted grid cell

parameters: k_i, g_i and d_i were used similarly to the related variables in equation 3 to solve for the grid cell gradient, $\frac{dz_i}{da_i}(a_i)$ as shown in equation 2.4

$$\frac{dz_i}{da_i}(a_i) = \frac{k_i}{1 + e^{-g_i(a_i - d_i)}} \tag{2.4}$$

where i represents the index of each grid cell, k is the maximum gradient for each grid cell. The rate of growth along the curve (g) and midpoint value on the curve (d) are also estimated for each grid cell. A detailed derivation of the grid cell specific relationships is provided in the Appendix. To preserve the maximum watershed storage, such that the sum of grid cell storage is equal to the watershed storage, the maximum gradient for each grid cell, k, the rate of growth along the curve, g and the midpoint value on the curve, d, are calculated as:

$$k_i = K \frac{A_{max}}{a_{i_{max}}} \tag{2.5.1}$$

$$g_i = G \frac{A_{max}}{a_{i_{max}}} \tag{2.5.2}$$

$$d_i = D \frac{a_{i_{max}}}{A_{max}} \tag{2.5.3}$$

This method was found to preserve watershed storage when mapped to grid cell storage with less than 3% difference. This was confirmed by integrating $\frac{dz_i}{da_i}$ to a volume (m^3) for all grid cells and comparing the summed storage value with the storage calculated over the watershed. The results of the scaling provided a parameter file representing the seasonally flooded area with a unique storage profile for each grid cell. The parameterization technique has three important characteristics. First, the ability to link dominant process using physical parametrization from remotely sensed data. Second, the parameter file can be easily updated with new remotely sensed observations. Third, it has the ability to represent storage observed in the watershed with a unique distribution of storage at the grid cell level based on the observed spatial distribution of surface inundation.

2.2.3 VIC model parameterization scenarios

The VIC model is a large scale hydrologic model that quantifies the land surface water and energy balance for each vegetation class within each model grid cell (Liang et al., 1994). A limitation of

previous hydrologic models used in the Red River has been the inability to simulate frozen soils and ponding on the land surface. The VIC model has the ability to simulate these features with inclusion of a lake and wetland algorithm and frozen soils algorithm (Cherkauer et al., 2003).

As part of this work, the lake and wetland algorithm has been integrated into the enhanced NASA Land Information System - based Variable Infiltration Capacity (LIS-VIC) model. The previous LIS-VIC model did not have the ability to represent lakes and wetlands. The lake and wetland algorithm uses physical parameters that describe the bathymetric profile of both perennially and intermittently flooded land. This depth-area profile can be parametrized in different ways such as through direct elevation profiles, using elevation profiles that are a function of topographic wetness index (TWI), and the option of using remotely sensed data described above.

Three parameterization scenarios were compared in this study. The three scenarios are: no parameterization of inundated depth-area (No IDA), ILA parameterized using TWI (TWI), and ILA parameterized using remotely sensed data (IDA). For the No IDA scenario, runoff moves downslope and is not delayed by local depressions. In the VIC model, the lake and wetland algorithm is not activated, so runoff from the grid cell exits the cell in the timestep it is generated, resulting in downstream flow. Differences between the TWI and IDA depth-area profiles used in the lake and wetland algorithm are shown in Figure 2.4 for a single grid cell.

TWI is a function of the contributing drainage area per unit contour length, a, over the surface slope, $\tan\beta$, so that $TWI = \ln(a/\tan\beta)$. Areas that contain low gradients and convergent flow result in a high TWI value and are areas of temporary water storage which can also contribute to runoff by saturation excess overland flow. Locations with similar TWI values are assumed to have hydrologically similar behaviors (Beven et al., 1979). For this parameterization, TWI values were calculated using an unprojected 30 m resolution digital elevation model (DEM) from the Shuttle Radar Topography Mission (SRTM) (Farr et al., 2007). The maximum percentage (ILA_{max}) of seasonally flooded area in each grid cell was defined using the MODIS ILA observations. The TWI values within each model grid cell were ranked, and the elevations associated with the highest ILA_{max} percent of pixels was used to define the relative depth-area profile in the VIC model. Because this method tends to overestimate surface storage capacity the relative depths were

rescaled using a maximum ILA depth of 1.0 m (Figure 2.4). A depth-area profile defined based on the lowest ILA_{max} pixels assumes that it is the lowest pixels in the landscape that pond water first, this methodology assumes that the highest TWI pixels will flood first, regardless of elevation. The TWI parametrization has a non-linear profile where approximately 90% of the depth is reached within 50% of the flooded area (Figure 2.4).

The IDA parameterization uses remotely sensed data observations of ILA. The local depressions delay runoff to downstream discharge by temporarily storing the water within the landscape until local depressions reach capacity. The depressions have varying storage capacities for each grid cell based on the maximum extent of the flooded area and estimated depth using equation 2.4. Figure 2.4 shows a maximum depth of approximately 0.4 m for the example grid cell. The IDA parameterization also has a non-linear profile. Ponded storage is distributed more proportionally within the grid cell fraction representing ILA compared to the TWI parameterization, where over 30% of the depth is reached within 50% of the flooded area (Figure 2.4).

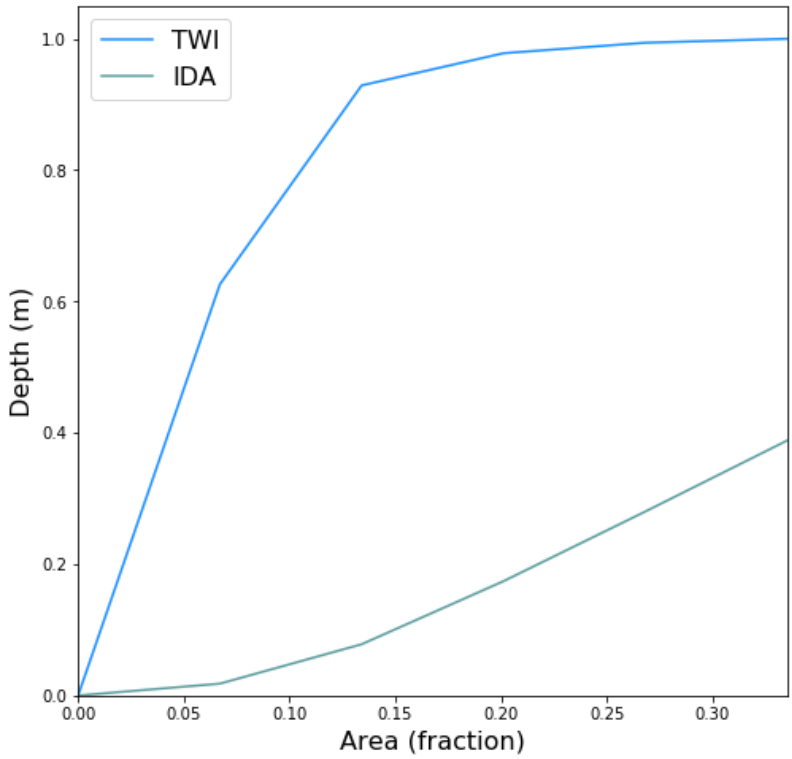

Figure 2.4: Example of the depth-area parameterization profile for a simulated grid cell representing seasonally flooded area. The topographic wetness index (TWI) parameterization based on surface topography alone has a greater storage capacity than the inundated depth-area (IDA) parameterization that incorporates remotely sensed of inundation area. Area of inundation increases more quickly with the IDA than the TWI parameterization.

The storage and distribution vary spatially between the TWI and IDA parameterizations which control the retention and release of water during peak flow events. Figure 2.5 shows that the TWI parameterization has a higher storage capacity than the IDA parameterization. For the IDA parameterization, the average storage is approximately 5 million cubic meters per grid cell, while the average storage for the TWI parameterization is approximately 12 million cubic meters per grid cell. The spatial distribution of storage increases from east to west for both parameterizations, where the highest storage is in the western portion of the watershed. In the western portion of the watershed soils are poorly drained and elevation gradient is low. The TWI parameterization shows an isolated area of higher storage capacity in the eastern portion of the watershed, whereas the IDA parameterization represents lower storage capacity (Figure 2.5). Grid cells representing seasonally ponded areas with a higher storage capacity will allow for more storage during peak flow events and reduce the magnitude of simulated peak flows.

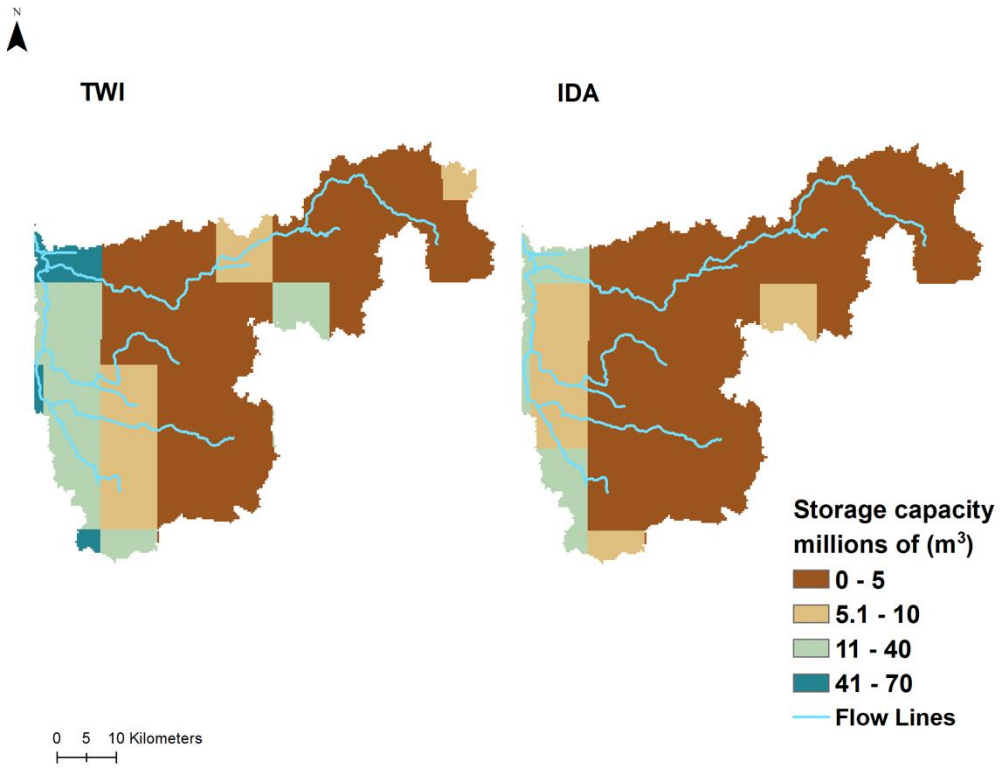

Figure 2.5: Spatial map of storage capacity (m^3) for simulated VIC grid cells using the TWI and IDA parameterizations of surface inundation. Simulated grid cells are 1/8th° latitude and longitude and masked to the extent of the watershed boundary.

2.2.4 Model calibration and evaluation

The VIC model was calibrated for the Buffalo River watershed from water years 2006 to 2009 and evaluated from water years 2010 to 2014 for each scenario. The calibration and evaluation period were selected based on available MODIS data in order to accurately represent and assess model performance of simulated discharge and ILA during peak flow events. A GIS based routing model was used to compare simulated and observed discharge (Yang et al., 2011). Model performance was analyzed using routed and observed streamflow as well as simulated and observed ILA. Table 2.1 lists the VIC model parameters that underwent calibration.

Automated calibration was performed using the Multi-Objective Complex Evolution (MOCOM-UA) to ensure calibration was objective amongst compared parameterization scenarios (Yapo et al., 1998). MOCOM-UA provides a set of objective Pareto solutions by minimizing objective functions with respect to model parameters. The objective functions used for the optimization of

streamflow were Nash-Sutcliffe efficiency (NSE), the NSE of the natural log data (LNSE) and percent bias (PBIAS). NSE was selected for calibration because of its sensitivity to peak flow events. LNSE was selected for calibration of baseflow. PBIAS was selected to evaluate the total streamflow using the difference in mean streamflow. The objective function used for calibrating ILA was absolute average error. Absolute average error was selected to analyze the average difference between observed and simulated ILA from peak flow events. Peak flow events were identified using peaks over threshold which is described in more detail in the following section.

Table 2.1: VIC model parameters selected for calibration for streamflow and ILA. Final optimized values for each test case are provided. No lake and wetland parameters were used for the No IDA case.

Parameter name	Description	Calibrated value for each scenario		
		No IDA	IDA	TWI
b_infil	Variable infiltration curve parameter, no units	0.08	0.17	0.08
Ds	Value at which non-linear baseflow begins, listed as a fraction of Dsmax	0.004	0.02	0.05
Dsmax	Maximum velocity of baseflow, listed as mm/day	1.0	9	1.2
Ws	Maximum soil moisture where non-linear baseflow begins, listed as a fraction	0.6	0.9	0.8
wfrac	Width of lake outlet, listed as a fraction of the lake perimeter	N/A	0.0002	0.0001
rpercent	Runoff that enters lake and wetland, listed as a fraction of the grid cell	N/A	2.7×rpercent	2.0×rpercent

2.2.5 Assessing peak flow events

In this study, peaks over threshold (POT) were used to analyze the occurrence of peak flow events and compare model performance with respect to observed data. POT was used to identify peak flow events using simulated and observed streamflow and MODIS ILA data. Daily discharge data

from USGS Station 05062000 were used to identify peaks above a threshold of 55 m^3/s. POT were evaluated seasonally, where seasons were defined as: spring (March–May), summer (June-August), fall (September-November) and winter (December-February). Peak discharge may differ temporally between compared parameterizations and observed peak flow, as a result a five-day window was used to identify peak events for the parameterization scenarios. For analysis of ILA, a threshold of 1% with a three-day moving average from the MODIS ILA time series was used to identify ILA events. The ILA event maxima from the MODIS three-day average was used to compare simulated ILA from the parameterization scenarios with the observed event maxima, and measure model performance from the same peak flow event. The three-day moving average was used to reduce noise and missing values caused by dates of high cloud coverage (>30%), which often occur during flooding events. The resulting smoothed dataset was able to provide a daily estimate of ILA.

2.3 Results

2.3.1 Model calibration and evaluation

The Pareto solutions generated by MOCOM-UA provide many sets of parameters. The parameter set used in calibration and evaluation was selected manually by comparing simulated streamflow and ILA with observed streamflow and ILA during the calibration period. The selected parameter values generated by MOCOM-UA along with calculated statistics for each simulated scenario are listed in Table 2.1 and Table 2.2. The test case without representing inundation (No IDA) was calibrated with MOCOM-UA for streamflow using four parameters: *b_infil*, *Ds*, *Dsmax* and *Ws*, whereas the parameterizations representing surface ponding (ILA and TWI) used two additional parameters, *wfrac* and *rpercent*. For the calibration period (water years 2006-2009), the IDA parameterization overall has the highest model performance with NSE, LNSE, PBIAS and absolute average error of 0.65, 0.55, 8% and < 1%, respectively. The No IDA and TWI have similar model performance but with different limitations. The No IDA scenario has a noticeably lower bias, yet the TWI scenario has a better LNSE. The calibration results of the TWI scenario are 0.66, 0.61, -24% and 2% for the NSE, LNSE, PBIAS and absolute average error, respectively. The NSE, LNSE and PBIAS for the No IDA scenario are 0.68, 0.27 and -2%, respectively. For the evaluation period (water years 2010-2014), the IDA parameterization again has the highest performance,

followed by the No IDA and TWI parameterizations. The calculated statistics for the IDA parameterization are 0.64, 0.70, 8% and 1% for NSE, LNSE, PBIAS and absolute average error, respectively. Overall, TWI has improved model performance than the No IDA scenario, yet the bias is higher. During the evaluation period, the IDA test case has a better NSE, LNSE and PBIAS than the other two scenarios. The TWI scenario represents baseflow satisfactorily during calibration and evaluation with respective LNSE values of 0.61 and 0.54, but has a high bias compared with the other two scenarios. The low LNSE for the No IDA parameterization can be explained by the overestimation of baseflow.

Table 2.2: Calculated objective function values quantifying model performance for the calibration and evaluation datasets. These represent the final set of parameters (Table 2.1) selected from the Pareto set generated by the MOCOM-UA optimization scheme. NSE, LNSE, and PBIAS were used to evaluate the streamflow simulation, while ILA Absolute Average Error was used to evaluate the simulation of ILA.

Parameterization	**Calibration (2006-2009)**				**Evaluation (2010-2014)**			
	NSE	LNSE	PBIAS (%)	ILA Absolute Avg. Error (%)	NSE	LNSE	PBIAS (%)	ILA Absolute Avg. Error (%)
No IDA	0.68	0.27	-2	N/A	0.47	-0.14	-8	N/A
IDA	0.65	0.55	8	<1	0.64	0.70	8	1
TWI	0.66	0.61	-24	2	0.61	0.54	-28	2

The routed streamflow for the three different scenarios and comparison with USGS streamflow is shown in Figure 2.6, for both the calibration and evaluation periods. For large peak flow events, all parameterizations were able to represent the events adequately, for example the high flow events in water years 2006 and 2009 (Figure 2.6). The IDA and TWI cases tend to have lower magnitudes as compared to the No IDA case, as the representation of surface ponding delays runoff and thereby reduces flood magnitude.

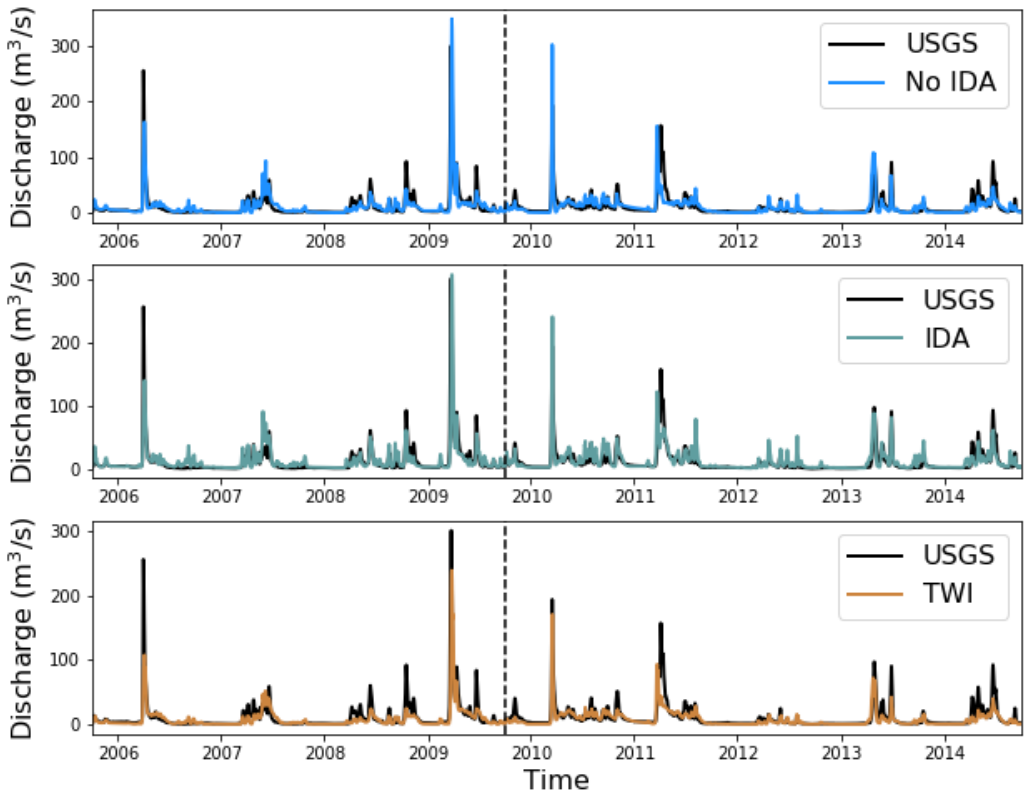

Figure 2.6: Time series comparing simulated streamflow from the three test case scenarios (No IDA, IDA and TWI) with observed USGS streamflow during calibration (left of dotted line) and evaluation (right of dotted line) periods.

The observed fractional ILA from the MODIS three-day average and simulated fractional ILA from the test cases representing surface ponding parameterizations are shown in Figure 2.7 for water years 2006 to 2014. A total of 24 peak ILA events were compared, where MODIS ILA values range from 1% to 10%. The IDA scenario is able to represent the range of observed ILA values, while the TWI scenario is not. The IDA scenario has a bias of -16% compared to the TWI scenario with a bias of -62% (Figure 2.7). Simulated peaks from the IDA parameterization compare better with the peaks from MODIS, than peaks simulated using the TWI parameterization.

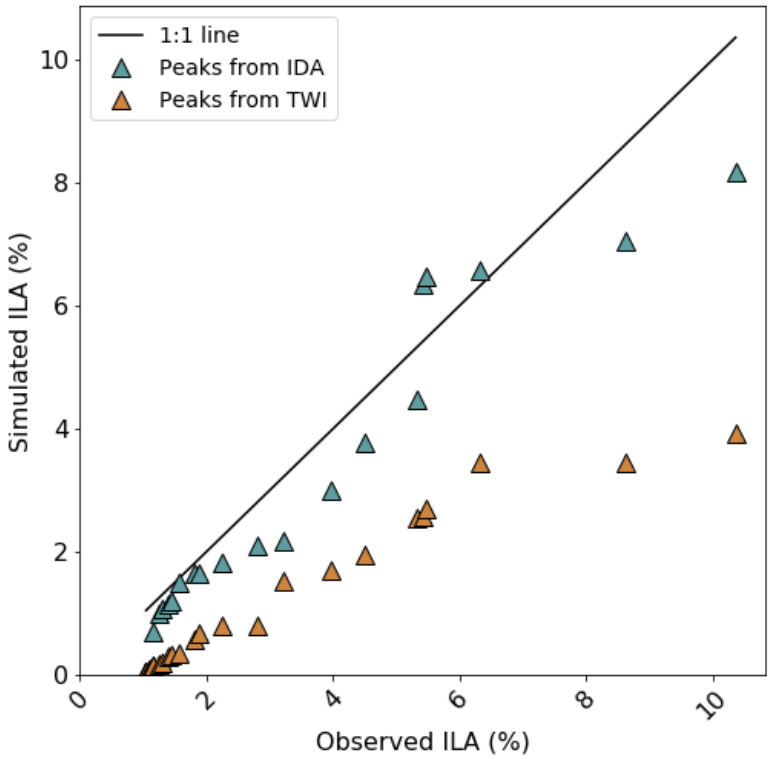

Figure 2.7: Comparison of simulated inundated land area from two parameterizations (IDA and TWI) with MODIS three-day average series using simulated peaks of ILA above the 1% threshold compared to the 1:1 line over the evaluation period (water years 2006-2014).

A spatial comparison of observed and simulated ILA from the IDA scenario is shown in Figure 2.8 from a spring flood event in 2009. The MODIS three-day composite (3D3OT) was used to generate the ILA map due to high occurrence of cloud coverage during the flood event. In general, ILA increases from east to west for both the observed and simulated data. ILA at the western portion of the watershed slightly underestimates the flooded extent during the spring 2009 flood event using the IDA parameterization. However, the spatial average of simulated and observed ILA are both approximately 4%. Figure 2.8 illustrates that the simulated ILA from the VIC model agrees with the MODIS observations in representing the spatial variability of ILA within the watershed.

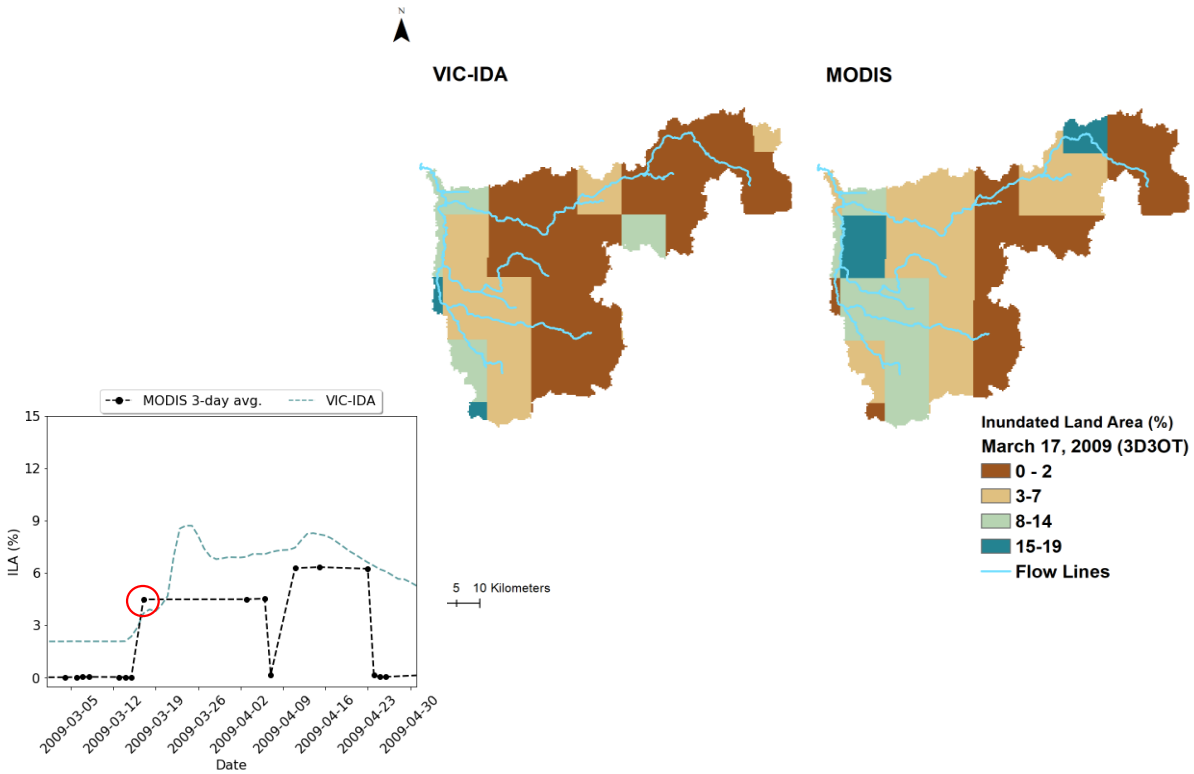

Figure 2.8: A comparison of simulated and observed ILA from a spring flood event March 17, 2009. A three-day composite (3D3OT). Simulated grid cells are 1/8$^{th°}$ latitude and longitude and masked to the extent of the watershed boundary.

2.3.2 Peak flow evens

The parameterization scenarios were evaluated for the ability to represent the occurrence and magnitude of observed peak flow events. Peak flow events are analyzed using simulated discharge from water years 2006 to 2014. Summary statistics of 14 corresponding peak flow events are shown in Figure 2.9. Simulated peaks were extracted only for these observed events, so there may have been simulated peaks above this threshold that were not included in this analysis. The USGS streamflow data have 14 peaks over the 55 m3/s threshold from water years 2006 to 2014. The identified peaks have a right-skewed distribution with a median value of 91 m3/s and an average of 120 m3/s. For the three simulated scenarios (No IDA, IDA and TWI), the distribution of maximum values for these 14 events is also right-skewed for each, but the IDA parameterization is the most representative of the interquartile range, mean and median peak flow events as shown in Figure 2.9. The similarity of the box plots for the IDA parameterization and USGS data using POT, demonstrates the ability to represent the variability of observed peak flow events.

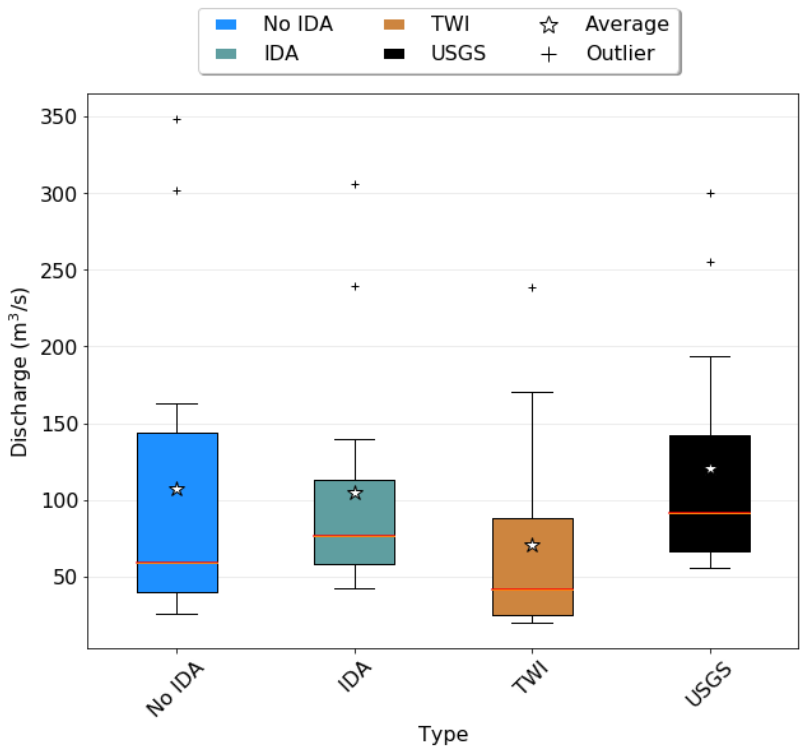

Figure 2.9: Box plot comparing three different scenarios, no inundated depth-area (No IDA), IDA and topographic wetness index (TWI) with observed discharge (United States Geological Survey 05062000) from corresponding peak flow events (n=14). Peak flow events were identified using a threshold of 55 m^3/s. The star in each box represents the average value, the red line in the box plot represents the median value and the plus marks indicate outlier values for each scenario.

The number of peak flow events by season for water years 2006 to 2014 is shown in Figure 2.10. In contrast to the previous POT analysis, the same threshold was applied to all time series, so the total number of events is different for each. The total number of events exceeding the threshold are 9, 15, and 7 for the No IDA, IDA and TWI parameterizations, respectively. In comparison, there were 14 observed peaks exceeding the threshold in the USGS data. Most peak flow events occurred in the Spring, followed by summer and then fall (Figure 2.10). Overall, the seasonal occurrences of peak flow events highlight that the IDA parametrization is the only scenario that captures the seasonal range of peak flow events observed in the USGS data. The IDA parameterization slightly overestimates the occurrence of peak flow events in the spring but has equal occurrences of exceedance with the observed data in the summer and fall. In contrast, the TWI scenario captures the same number of occurrences of peak flow events in the spring but does

not represent the occurrences of peak flow events in the summer and fall. For the No IDA scenario, the number of peak flow events matches the observed record in the spring, but also underestimates occurrences in the summer and does not simulate peak flow events in the fall.

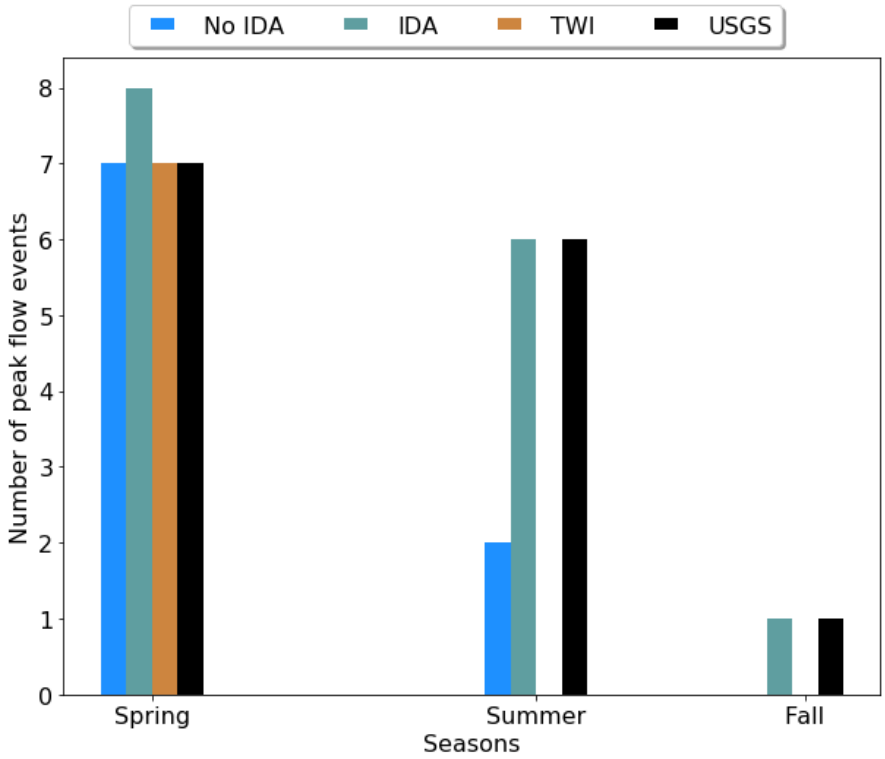

Figure 2.10: Seasonal occurrences of peak flow events identified using peaks over threshold. Threshold set at 55 m^3/s.

2.3.3 Hydrologic analysis of peak flow events

Peak flow events in the Buffalo River watershed are most commonly associated with snowmelt in the late winter-spring, and to a lesser extent in the summer-fall associated with persistent wet weather (Figure 2.10). Runoff generation mechanisms are expected to be different between these seasons. To illustrate the difference in runoff generation mechanisms, we analyzed two peak flow events each for the winter-spring and summer-fall seasons to identify the simulated runoff generation mechanism. The two winter-spring events (March 2009 and March 2010) and two summer-fall events (October 2008 and June 2014) are analyzed by representing the seasonal ponding from the IDA parameterization and comparing simulated streamflow and ILA with the interactions of rainfall plus snowmelt (mm) and frost depth (cm). Rainfall plus snowmelt

represents the total amount of available water used in the model simulation. Observed data is used to support the determination of the runoff generation mechanism using USGS discharge and ILA from MODIS.

Figure 2.11 displays the winter-spring simulations, where ILA increases over frozen soils approximately two weeks prior to peak flow. After ILA reaches its maxima, both simulated and observed discharge increase rapidly, as the ILA declines. The timing of observed ILA with simulated ILA is difficult to compare due to the influence of high cloud coverage which prevents the retrieval of ILA observations during the observed peak flow events. For each of the peak flow winter-spring events, only three MODIS observations were available for estimation of surface ponding (indicated by black circles in Figure 2.11). Though limited with observations during winter-spring events, the MODIS time series can be used to provide a general assessment of the duration ponded water remains stored on the surface. Once peak discharge is reached, ILA continues to decrease more gradually as the frost depth decreases. The variable source area (VSA) concept, describes the runoff generation mechanisms behind the winter-spring peak flow events (Dunne et al., 1975). The saturated areas increase from precipitation and snowmelt on frozen soils that limit infiltration (Cherkauer et al., 1999). The outputs from the IDA parameterization represent the VSA concept in Figure 2.11, where ILA increases over the frozen soils, and stored water on the land surface accumulates prior to peak discharge. After peak discharge is reached, ILA gradually decreases as frost depth decreases enabling infiltration and subsurface drainage. The increase in ILA is related to the low permeability from the soil ice content. In addition, to the VSA concept, another runoff generation mechanism is represented in the simulated and observed data. The rise and fall of ILA after peak flow simulates the fill and spill mechanism, where local depressions in low gradient areas contribute to runoff generation once depressions reach capacity following the peak flow event and continue to spill and fill (Coles et al., 2018; Mcdonnell, 2013; Tromp-van Meerveld et al., 2006). The spill and fill mechanism is most noticeable in the spring 2009 event and are also captured with the observed discharge and ILA data as surface ponding increases (fill) before each increase in discharge (spill) (Figure 2.11). It is also important to note that the IDA parameterization does simulate a delay in peak flow for the spring event in 2009. The delay is a limitation in the model performance and potential area of improvement.

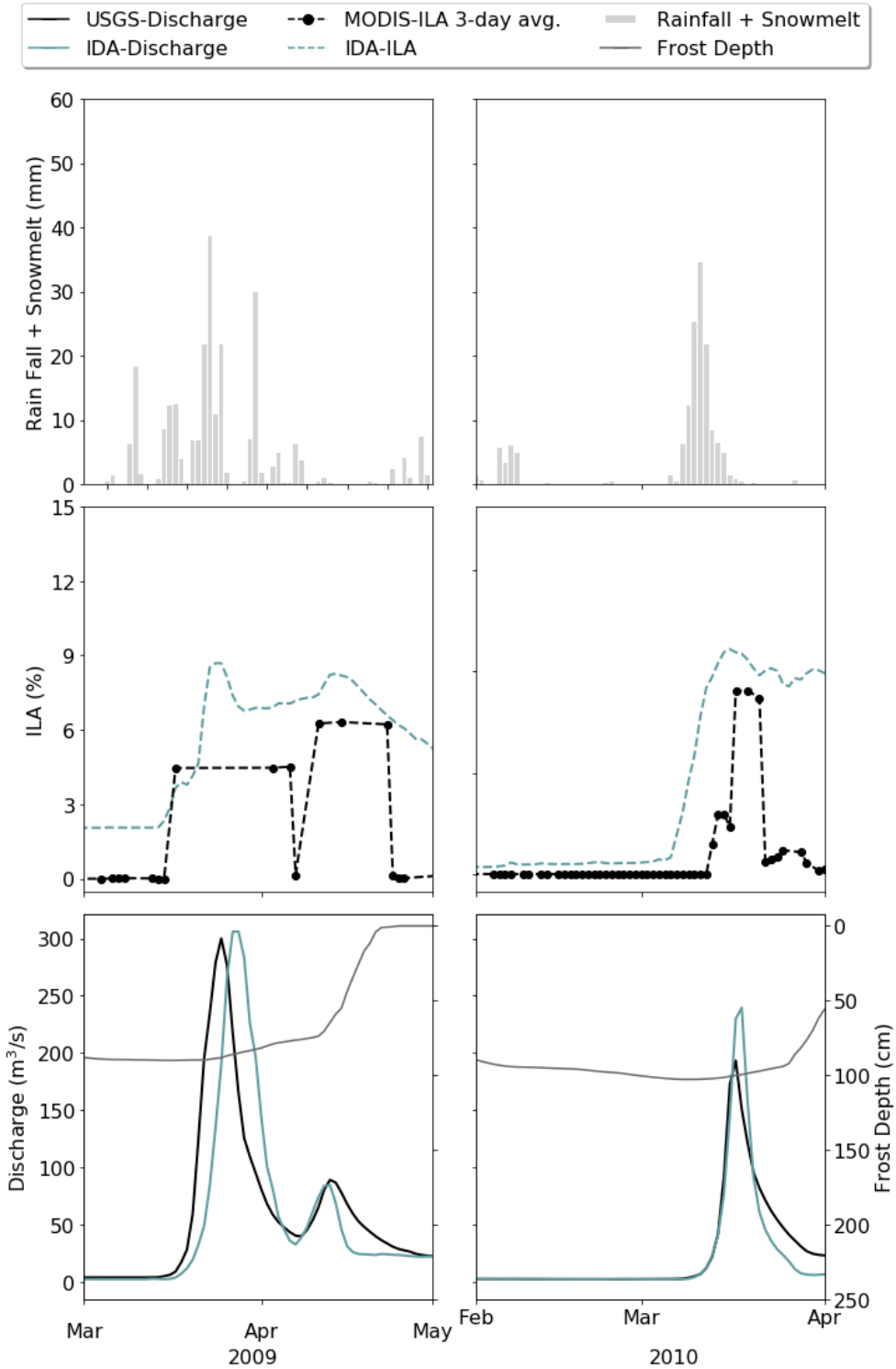

Figure 2.11: Observed and simulated discharge (m^3/s) and inundated land area (%) with interactions of frost depth (cm) and rainfall plus snowmelt (mm) for flood events in winter-spring seasons. Black circles indicate available cloud-free MODIS observations to estimate the three-day average.

Figure 2.12 shows the summer-fall simulations, where ILA increases rapidly approximately a week prior to peak flow. After ILA peaks, discharge increases but at a lower rate and magnitude compared to simulated discharge in the winter-spring, as ILA decreases through reinfiltration into drier soils. Infiltration-excess overland describes the runoff generation mechanism for summer-fall peak flow events (Horton, 1933). In these events, fractional ILA increases from runoff of excess precipitation causing an increase in storage on the land surface. After peak discharge, ILA decreases rapidly as infiltration is no longer limited. The observed discharge and ILA support infiltration excess overland flow as the runoff generation mechanisms for the summer-fall events shown in Figure 2.12. Though high cloud coverage affects the retrievals of ILA observations during the summer-fall events, the MODIS time series is able to capture the short durations of ponded water on the landscape. During the summer-fall events, the duration of ponded water on the surface is shorter than the winter-spring as frozen soils are not a factor restricting infiltration and rainfall events are shorter in duration. The duration of ponded water is influenced by the total precipitation and infiltration capacity where the ponded extent decreases after precipitation subsides and infiltration is no longer limited. The response of the simulated discharge with the IDA parametrization is representative of the observed discharge for the fall and summer events in 2008 and 2014, respectively (Figure 2.12). Though simulated ILA generally overestimates when compared to the MODIS three-day average, the IDA parameterization is able to represent the rapid increase and decrease of ponded water on the surface for summer-fall events.

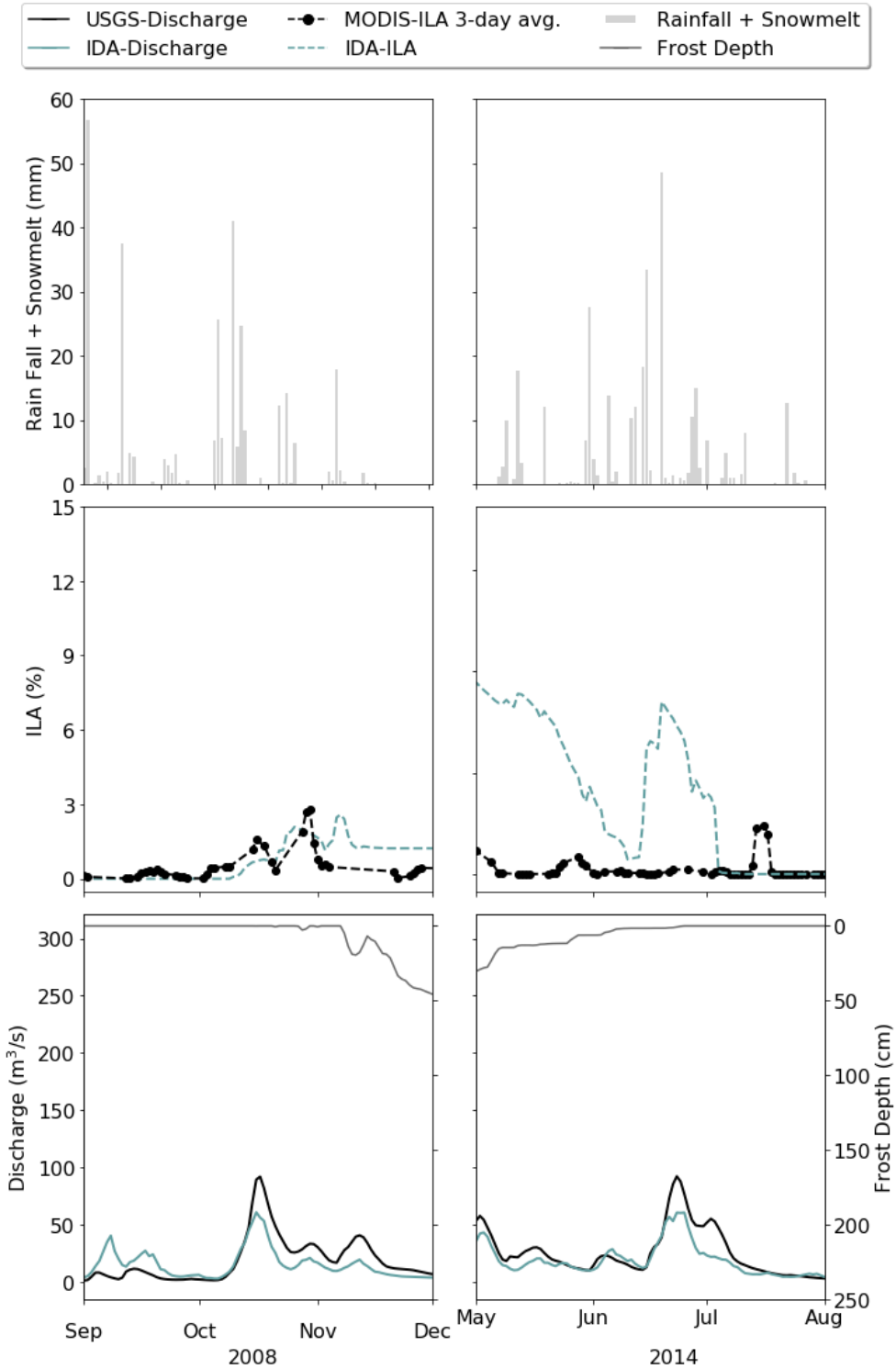

Figure 2.12: Observed and simulated discharge (m^3/s) and inundated land area (%) with interactions of frost depth (cm) and rainfall plus snowmelt (mm) for flood events in the summer-fall seasons. The black circles indicate available cloud-free MODIS observations to estimate the three-day average.

2.4 Discussion

In this study we develop a parameterization methodology to represent the influence of ILA on streamflow. The IDA parametrization uses readily available remotely sensed and in-situ observations. The methodology used to represent surface ponding is transferable to other locations and physically constrains the amount of surface water storage based on observations. Moreover, the IDA parameterization generates a unique distribution of storage for each simulated grid cell based on the watershed's physical characteristics. The depth-area relationship for the test watershed is developed using 24 peak flow events of varying size from water years 2005-2009 (Figure 2.4). Due to high cloud coverage (>30%), ILA observations from MODIS are often missed during observed peak discharge. These observations are important in generating the logistic fit and parameterizing the seasonally ponded extent and depth into the VIC lake and wetland algorithm. Future work may be able to replace these missing observations using active sensors to update and improve the representation of surface ponding. The daily MODIS NRT Global Flood Mapping product provides data with flooded and non-flooded area. The four-step filtering process helps reveal the highest quality MODIS observations of ILA. Analyzing the discharge record helps discard observations from the parameterization that the VIC model cannot represent, such as overbank flow. The seven-day antecedent rainfall filter improved the quality of the data by removing noisy data below the precipitation threshold for the growing and dormant seasons.

To examine the influence of ILA on streamflow, daily time series of routed streamflow and ILA are evaluated for three simulated scenarios (No IDA, IDA and TWI) and compared with observed data. In the No IDA scenario, runoff is not delayed by local depressions. By not representing local depressions, the routed streamflow overestimates low and high flows compared to the observed streamflow and alternative test cases. In the TWI scenario, local depressions are represented as a function of the contributing drainage area per unit contour length, over the surface slope. The routed streamflow underestimates high flows but simulates low flows better compared to the No IDA scenario and observed streamflow. The simulated ILA also underestimates peak flow events compared to the observed ILA and IDA scenario. For the IDA scenario, local depressions are represented using remotely sensed observations of ILA. For routed streamflow, the new IDA parameterization outperforms comparative parameterizations. The statistical analysis of the routed streamflow during the calibration and evaluation periods demonstrates that the IDA

parameterization has a higher performance and the ability to represent low and high flows compared to the alternative test cases. The statistical analysis of ILA reveals that the IDA parameterization outperforms the TWI parameterization.

In the development of the IDA parameterization, a logistic function was fit to observations of the gradient (m^{-1}) and flooded extent (m^2) to provide an estimate of surface water storage in the watershed for varying flood events. The surface water storage is not estimated by describing the shape of the landscape, but by calculating the derivative of the landscape (i.e., slope). The depth-area profile after integration of the logistic function describes the non-linear increase of surface water storage, which gradually increases in low topography areas of the floodplain, followed by a steeper increase in storage as flooding expands up onto the valley slopes. The logistic function was selected in this study to represent the limited amount of storage capacity within the watershed's low gradient agricultural landscape. In addition, the logistic function was able to preserve the cumulative watershed storage when mapped to represent individual grid cell storage. The TWI parametrization estimated surface water storage using a DEM, which tends to overestimate the storage capacity compared to the IDA parameterization and generally underestimated the extent of the flooded area compared to the observed ILA. Though the TWI parameterization represents the distribution of land pixels that are likely to be flooded, because that distribution is essentially removed from the spatial context, it is difficult to estimate the depth of inundation. The depth of inundation then becomes a separate parameterization, and in this study was set to a constant (1.0 m). Future research may work to improve the estimate of the storage capacity with the TWI parameterization by using the IDA parameterization to estimate the storage capacity. This would allow users to retain the depth-area profile associated with the TWI with improved estimates of the storage capacity from observed flood events.

Through the analysis of peak flow events, we are able to investigate the utility of each parameterization to represent the occurrence and magnitude of peak events. Overall, the IDA parameterization captures the variability in magnitude of peak flow events and accurately represents surface ponding observed within the watershed. Regarding the seasonal occurrence of peak flow events, the IDA scenario is the only parameterization that captures peak flow events for all seasons, whereas TWI and No IDA were not able to represent summer and fall peak flow events

above the defined threshold (55 m^3/s). Previous studies have investigated the use of remotely sensed retrievals of water level and inundated area to improve flood forecasting skill (Andreadis et al., 2007, 2014; Grimaldi et al., 2016; Neal et al., 2009; Schumann et al., 2009). Andreadis et al. (2014) used synthetic observations of ILA at the same spatial resolution (600 m) and observation accuracy (< 20%) as the proposed Surface Water Ocean Topography (SWOT) mission and assimilated the data into a hydrologic model for evaluation of flood forecast skill in the Ohio River basin. Analysis of the largest flood event in the study shows that the forecasted ILA does not represent the flood dynamics represented in the observations, and forecast skill is shown to increase within two to three days of the forecast, demonstrating the importance of retrieval time as described by Grimaldi et al. (2016). Though high cloud coverage often prevented MODIS retrievals of ILA within two-three days of peak flow, the development of a parameterization using a range of remotely sensed ILA observations demonstrates the utility to represent the seasonal occurrence and range in flood magnitude as well as the potential to increase forecast skill.

Schumann et al. (2009) discusses the challenges of obtaining quality remotely sensed observations needed to increase flood forecast skill and suggests understanding the runoff generating mechanisms to improve flood forecast skill. The results of our case study provide better understanding of the underlying mechanisms causing runoff generation within the study domain. The results further reveal that the VSA concept and fill and spill are the dominant runoff generation mechanisms during the winter-spring seasons in the Buffalo River watershed (Coles et al., 2018; Dunne et al., 1975; Mcdonnell, 2013; Tromp-Van Meerveld et al., 2006). On the other hand, infiltration-excess overland is the dominant runoff generation mechanism during the summer-fall seasons in the Buffalo River watershed (Horton, 1933). The IDA parameterization is able to represent peak flow events for different seasons when compared with observed discharge. However, the delay in peak discharge during the winter-spring events reveal a limitation within the model. Identifying the cause of the delay is beyond the scope of this study but may be of interest in future work. The simulated ILA in the case study shows that the IDA parameterization can represent the seasonal variation in ILA and provide inferences that help determine runoff generation mechanisms. For the summer-fall event in 2014, the MODIS time series shows little change in ILA compared to the simulated data. Newspaper articles reported heavy rainfall in mid-June resulting in flooded fields, where the USDA estimated damaged crops to approximately seven

percent of the corn and soybean in the state of Minnesota (Meersman, 2014; Thiesse, 2014; Webb, 2014). The increase in precipitation and discharge were captured in the observed data but missed in the MODIS ILA. In a watershed where land use is predominately agriculture, the shallow ILA may be obscured from satellite sensors under vegetation. Detection of ILA under vegetation is a known cause of omission leading to errors of estimating ILA (Lakshmi, 2016; Nigro et al., 2014). Policelli et al. (2017) are exploring other approaches to obtain accurate retrievals associated with flooded vegetation. The MODIS and simulated ILA are estimates, where different factors can influence the estimate of water extent. The simulated ILA demonstrates the potential to support remotely sensed retrievals of ILA.

2.5 Conclusions

In this study, we describe an adaptable methodology to parameterize the depth-area relationship of ILA in an existing large-scale hydrologic model using remotely sensed and in-situ observations. The Buffalo River watershed, which is prone to flooding due to the topography's low gradient, high intensity rainfall events, saturated soil conditions and/or snowmelt over frozen soils, is the area of interest. The influence of ILA on streamflow is investigated and reveals the following:

1. Accessible remotely sensed and in-situ observations can provide adaptable parameterizations to represent inundated land area. The developed parameterization technique delivers three important characteristics. (1) The ability to link dominant processes using physical parametrization from remotely sensed data. (2) The parameter file can be easily updated with new remotely sensed observations. (3) The capability of representing realistic storage observed in the watershed with unique distribution of storage at the grid cell level.
2. Simulated streamflow is well-represented and improved by representing ILA in the VIC model. Model performance (NSE, LNSE, PBIAS, and absolute average error) results shows that the IDA parameterization outperforms compared test cases after optimization.
3. The IDA parameterization improves representation of the seasonal pattern of peak flow events and range in magnitude. The IDA parametrization has the ability to represent peak flow events in all seasons, with a tendency to overestimate the number of occurrences in the spring.

4. Results of the case study demonstrate two dominant runoff generating mechanisms in the Buffalo River watershed. The VSA concept describes the runoff generation mechanism behind the winter-spring peak flow events, while infiltration excess overland flow describes the runoff generation mechanism for summer-fall peak flow events.

Adaptable parameterizations are needed for hydrologic models to mirror the increasing changes in water resources in a changing climate. Remotely sensed observations can help facilitate updatable parameterizations in hydrologic models by capturing and characterizing variables represented in hydrologic models. In this study, we demonstrate the use of incorporating the MODIS NRT Global Flood Mapping product with discharge data to parameterize inundated land area occurring in agricultural uplands. The parameterization methodology uses available data to describe the local ponding characteristics and evaluate the influence of the upland inundation on downstream flow. The results of the study demonstrate the utility of the parameterization to represent the occurrence of peak flow events during different seasons and to represent the range in magnitude while accurately simulating daily streamflow following events.

2.6 Supplementary materials

2.6.1 Equations used to calculate gradient and scale logistic function

Inundated Depth-Area Relationship Theory

Variables used to describe analysis at the watershed scale are capitalized, whereas lowercase variables are used to describe analysis at the grid cell scale.

Observed change in water depth with respect to change in inundated area

The depth-area relationship begins by first deriving the incremental volume, ΔV (m^3) of water stored on the landscape associated with the estimated flooded area and depth of inundation as shown in equation A1.1

$$\Delta V = \left(\frac{A_{t_1} + A_{t_2}}{2}\right) * \ (Z_{t_1} - Z_{t_2}) \qquad \text{(A1.1)}$$

Where A_{t_1} and A_{t_2}, are MODIS observations of inundated land area (m^2) from consecutive overpasses (t_1 and t_2), and z is the depth of water (m) in the watershed over the period of subsequent

MODIS retrievals. The ΔV calculated in equation A1.1 is assumed to be equivalent to the accumulated Q between consecutive retrievals as show in equation A1.2

$$\Delta V = \int_{t_1}^{t_2} Q(t)\, dt \tag{A1.2}$$

where Q is the observed fast response runoff that is assumed to be released from the total flooded area identified by MODIS (A_{t_1}) within the timeframe (t_1 to t_2).

The change in depth, ($dz = Z_{t_1} - Z_{t_2}$) from equation A1.1 uses the relationship of observed stormflow (m^3) over the flooded extent (m^2), based on the assumption that the change in volume on the surface is equal to the observed stormflow during this period. This relationship is expressed in equation A2.

$$dZ = \frac{2 * \left(\int_{t_1}^{t_2} Q\, dt\right)}{\left(A_{t_1} + A_{t_2}\right)} \tag{A2}$$

The estimated gradient, $\frac{dZ}{dA}$, can be used to determine the volume of water stored the land surface. The change in flooded extent ($dA = A_{t_1} - A_{t_2}$) was captured with MODIS from consecutive overpasses. A change in dA represents ponded water leaving local depressions through stormflow. The ponded depth of ILA associated with different flood extents was calculated by integrating the gradient, $\frac{dZ}{dA}$, with respect to flooded extent, A, to get the cumulative depth of water for different flood extents.

Parameter and depth estimation using logistic fit

The gradient and flooded relationship can be used to estimate water storage on the land surface. The fitted equation is listed in equation A3

$$\frac{dZ}{dA}(A) = \frac{K}{1 + e^{-G(A-D)}} \tag{A3}$$

where K is the maximum gradient value from the fitted curve. K had a fitted value of $3.93*10^{-9}$ m^{-1}. The parameter value for G was $7.01*10^{-8}$ m. The parameter value of the midpoint on the logistic curve, D was $3.8*10^7$ m^2 (38 km^2).

After integration of equation A3, the ponded depth of ILA for the watershed is calculated as shown in Equation A4.

$$Z(A) = K\left\{A + \frac{1}{G} ln\left(e^{-G(A-D)} + 1\right) - \frac{1}{G} ln(e^{GD} + 1)\right\} \quad \text{(A4)}$$

The total storage, V_{total}, can be calculated with integration of Z from 0 to A_{max}, as shown in Equation A5,

$$V_{total} = \int_0^{A_{max}} Z(A)\, dA \quad \text{(A5)}$$

Scaling procedure within grid cells to preserve storage

To represent the storage within each grid cell, we scale the storage of the entire watershed. We do this by calculating the ponded depth, *z*, and the volume, *v*, of each grid cell, using the maximum observed flooded area for each grid cell, $a_{i_{max}}$. The approach is the same as estimating storage for the watershed and is shown below:

$$\frac{dz_i}{da_i}(a_i) = \frac{k_i}{1 + e^{-g_i(a_i - d_i)}} \quad \text{(A6)}$$

$$z_i = k_i\left\{a_i + \frac{1}{g_i} ln\left(e^{-g_i(a_i - d_i)} + 1\right) - \frac{1}{g_i} ln(e^{g_i d_i} + 1)\right\} \quad \text{(A7)}$$

$$v_{i\ total} = \frac{a_{i_{max}}}{A_{max}} V_{total} = \int_0^{a_{i_{max}}} z_i(a_i)\, da_i \quad \text{(A8)}$$

To preserve the watershed storage, such that $\sum_{i=1}^{N} v_{i_{total}} = V_{total}$, with the assumption that the volume of storage in each grid cell is proportional to the fraction of flooded area in each grid cell, the maximum gradient for each grid cell, *k*, the rate of growth along the curve, *g* and the midpoint value on the curve, *d*, are calculated as:

$$k_i = K\frac{A_{max}}{a_{i_{max}}} \quad \text{(A9.1)}$$

$$g_i = G\frac{A_{max}}{a_{i_{max}}} \quad \text{(A9.2)}$$

$$d_i = D\frac{a_{i_{max}}}{A_{max}} \quad \text{(A9.3)}$$

2.7 References

Andreadis, K. M., Clark, E. A., Lettenmaier, D. P., & Alsdorf, D. E. (2007). Prospects for river discharge and depth estimation through assimilation of swath-altimetry into a raster-based hydrodynamics model. *Geophysical Research Letters*, *34*(10), 1–5. https://doi.org/10.1029/2007GL029721

Andreadis, K. M., & Schumann, G. J. P. (2014). Estimating the impact of satellite observations on the predictability of large-scale hydraulic models. *Advances in Water Resources*, *73*, 44–54. https://doi.org/10.1016/j.advwatres.2014.06.006

Beven, K. J., & Kirkby, M. J. (1979). A physically based, variable contributing area model of basin hydrology. *Hydrological Sciences Bulletin*, *24*(1), 43–69. https://doi.org/10.1080/02626667909491834

Bowling, L. ., & Lettenmaier, D. P. (2010). Modeling the Effects of Lakes and Wetlands on the Water Balance of Arctic Environments. *Journal of Hydrometeorology*, *11*(2), 276–295. https://doi.org/10.1175/2009JHM1084.1

Carroll, M. L., DiMiceli, C. M., Wooten, M. R., Hubbard, A. B., Sohlberg, R. A., & Townshend, J. R. . (2017, January 1). MOD44W MODIS/Terra Land Water Mask Derived from MODIS and SRTM L3 Global 250m SIN Grid V006. https://doi.org/https://doi.org/10.5067/MODIS/MOD44W.006

Cherkauer, K. A., Bowling, L. C., & Lettenmaier, D. P. (2003). Variable infiltration capacity cold land process model updates. *Global and Planetary Change*, *38*(1–2), 151–159. https://doi.org/10.1016/S0921-8181(03)00025-0

Cherkauer, K. A., & Lettenmaier, D. P. (1999). Hydrologic effects of frozen soils in the upper Mississippi River basin. *Journal of Geophysical Research Atmospheres*, *104*(D16), 19599–19610. https://doi.org/10.1029/1999JD900337

Chu, X., Yang, J., Chi, Y., & Zhang, J. (2013). Dynamic puddle delineation and modeling of puddle-to-puddle filling-spilling-merging-splitting overland flow processes. *Water Resources Research*, *49*(6), 3825–3829. https://doi.org/10.1002/wrcr.20286

Coles, A. E., & McDonnell, J. J. (2018). Fill and spill drives runoff connectivity over frozen ground. *Journal of Hydrology*, *558*, 115–128. https://doi.org/10.1016/j.jhydrol.2018.01.016

Commission, R. R. B. (2011). *RED RIVER BASIN COMMISSION ' S LONG TERM FLOOD SOLUTIONS For the Red River Basin Final Report to the States of Minnesota Pursuant to Session North Dakota Chapter Counties Interstate Engineering*.

Du, J., Kimball, J. S., Galantowicz, J., Kim, S. B., Chan, S. K., Reichle, R., Jones, L. A., & Watts, J. D. (2018). Assessing global surface water inundation dynamics using combined satellite information from SMAP, AMSR2 and Landsat. *Remote Sensing of Environment*, *213*(March), 1–17. https://doi.org/10.1016/j.rse.2018.04.054

Dunne, T., Moore, T. R., & Taylor, C. H. (1975). Recognition and Prediction of Runoff-Producing Zones in Humid Regions The dynamics surface processes in response to the declining Dead Sea level View project. *Hydrological Sciences Bulletin*, *20*(3), 305–327.

Eckhardt, K. (2005). How to construct recursive digital filters for baseflow separation. *Hydrological Processes*, *19*(2), 507–515. https://doi.org/10.1002/hyp.5675

Farr, T. G., Rosen, P. A., Caro, E., Crippen, R., Duren, R., Hensley, S., Kobrick, M., Paller, M., Rodriguez, E., Roth, L., Seal, D., Shaffer, S., Shimada, J., Umland, J., Werner, M., Oskin, M., Burbank, D., & Alsdorf, D. (2007). The Shuttle Radar Topography Mission. *Rev. Geophys*, *45*, 2004. https://doi.org/10.1029/2005RG000183

Grimaldi, S., Li, Y., Pauwels, V. R. N., & Walker, J. P. (2016). Remote Sensing-Derived Water Extent and Level to Constrain Hydraulic Flood Forecasting Models: Opportunities and Challenges. *Surveys in Geophysics*, *37*(5), 977–1034. https://doi.org/10.1007/s10712-016-9378-y

Grimm, K., Tahmasebi Nasab, M., & Chu, X. (2018). TWI Computations and Topographic Analysis of Depression-Dominated Surfaces. *Water*, *10*(5), 663. https://doi.org/10.3390/W10050663

Hay, L., Norton, P., Viger, R., Markstrom, S., Steven Regan, R., & Vanderhoof, M. (2018). Modelling surface-water depression storage in a Prairie Pothole Region. *Hydrological Processes*, *32*(4), 462–479. https://doi.org/10.1002/hyp.11416

Horton, R. E. (1933). The Role of infiltration in the hydrologic cycle. *Transactions, American Geophysical Union*, *14*(1), 446. https://doi.org/10.1029/TR014i001p00446

Jae, K., Engel, B. A., Tang, Z., Choi, J., Kim, K.-S., Muthukrishnan, S., & Tripathy, D. (2005). *Automated Web GIS Based Hydrograph Analysis Tool. WHAT. Journal of the American Water Resources Association* (Vol. 41).

Lakshmi, V. (2016). *Remote Sensing of Hydrological Extremes. Springer Remote Sensing/Photogrammetry*.

Liang, X., Lettenmaier, D. P., Wood, E. F., & Burges, S. J. (1994). A simple hydrologically based model of land surface water and energy fluxes for general circulation models. *Journal of Geophysical Research*, *99*(D7), 14,415-14,428. https://doi.org/10.1029/94JD00483

Mcdonnell, J. J. (2013). Are all runoff processes the same? *Hydrological Processes*, *27*(26), 4103–4111. https://doi.org/10.1002/hyp.10076

Meersman, T. (2014, June 20). Minnesota farmers await dry weather. *TCA Regional News*. Retrieved from https://search.proquest.com/wire-feeds/minnesota-farmers-await-dry-weather/docview/1537603021/se-2?accountid=13360

Neal, J., Schumann, G., Bates, P., Buytaert, W., Matgen, P., & Pappenberger, F. (2009). A data assimilation approach to discharge estimation from space. *Hydrological Processes*, (23), 3641–3649. https://doi.org/10.1002/hyp.7518

Nigro, J., Slayback, D., Policelli, F., & Brakenridge, G. R. (2014). *NASA/DFO MODIS Near Real-Time (NRT) Global Flood Mapping Product Evaluation of Flood and Permanent Water Detection*. Retrieved from https://floodmap.modaps.eosdis.nasa.gov/documents/NASAGlobalNRTEvaluationSummary_v4.pdf

NWS. (1998). *Service assessment and hydraulic analysis Red River of the North 1997 floods*. book, Silver Spring, MD: U.S. Dept. of Commerce, National Oceanic and Atmospheric Administration, National Weather Service.

Pagano, T. C., Wood, A. W., Ramos, M.-H., Cloke, H. L., Pappenberger, F., Clark, M. P., Cranston, M., Kavetski, D., Mathevet, T., Sorooshian, S., & Verkade, J. S. (2014). Challenges of Operational River Forecasting. *Journal of Hydrometeorology*, *15*(4), 1692–1707. https://doi.org/10.1175/JHM-D-13-0188.1

Pielke, R. a. (1999). Who decides? Forecasts and responsibilities in the 1997 Red River flood. *Applied Behavioral Science Review*, *7*(2), 83–101. https://doi.org/10.1016/S1068-8595(00)80012-4

Policelli, F., Slayback, D., Brakenridge, B., Nigro, J., Hubbard, A., Zaitchik, B., Carroll, M., & Jung, H. (2017). The NASA Global Flood Mapping System. In V. Lakshmi (Ed.), *In Remote Sensing of Hydrological Extremes* (pp. 47–63). Stanford: Springer, Cham. https://doi.org/10.1007/978-3-319-43744-6_3

Schumann, G., Bates, P. D., Horritt, M. S., Matgen, P., & Pappenberger, F. (2009). Progress in integration of remote sensing-derived flood extent and stage data and hydraulic models. *Reviews of Geophysics*, *47*(3), 1–20. https://doi.org/10.1029/2008RG000274

Shook, K. R., & Pomeroy, J. W. (2011). Memory effects of depressional storage in Northern Prairie hydrology. *Hydrological Processes*, *25*(25), 3890–3898. https://doi.org/10.1002/hyp.8381

Silva, V. De. (2020, October 20). Fit Logistic Curve to a Data Set - File Exchange - MATLAB Central. MATLAB Central File Exchange. Retrieved from https://www.mathworks.com/matlabcentral/fileexchange/31399-fit-logistic-curve-to-a-data-set

Sun, D., Yu, Y., & Goldberg, M. D. (2011). Deriving Water Fraction and Flood Maps From MODIS Images Using a Decision Tree Approach. *IEEE Journal of Selected Topics in Applied Earth Observations and Remote Sensing*, *4*(4), 814–825. https://doi.org/10.1109/JSTARS.2011.2125778

Thiesse, K. (2014, June 25). Severe storms, excessive rainfall plague many areas. *Swift County Monitor News*. Retrieved from http://www.swiftcountymonitor.com/articles/2014/06/25/severe-storms-excessive-rainfall-plague-many-areas

Todhunter, P. E. (2001). A Hydroclimatological Analysis of The Red River of The North Snowmelt Flood Catastrophe of 1997. *JOURNAL OF THE AMERICAN WATER RESOURCES ASSOCIATION*, *37*(5). https://doi.org/10.1111/j.1752-1688.2001.tb03637.x

Tromp-van Meerveld, H. J., & McDonnell, J. J. (2006). Threshold relations in subsurface stormflow: 2. The fill and spill hypothesis. *Water Resources Research*, *42*(2). https://doi.org/10.1029/2004WR003800

Tromp-Van Meerveld, H. J., & McDonnell, J. J. (2006). Threshold relations in subsurface stormflow: 2. The fill and spill hypothesis. *Water Resources Research*, *42*(2), 1–11. https://doi.org/10.1029/2004WR003800

U.S. Geological Survey. (2018). USGS's National Water Use Information Program, National Water Information System. Retrieved October 1, 2018, from https://waterdata.usgs.gov/nwis/

USACE. (2015). *Recent US Climate Change and Hydrology Literature Applicable to US Army Corps of Engineers Missions – Water Resources Region 09, Souris-Red-Rainy Rivers.* Washington, D.C.

USACE. (2017). *Flood Risk Management and Hydrology Appendix A*.

USDA-NRCS. (2018). Rapid Watershed Assessment Resource Profile Buffalo Watershed (MN) HUC : 09020106. Retrieved January 9, 2018, from https://www.nrcs.usda.gov/Internet/FSE_DOCUMENTS/nrcs142p2_022744.pdf

Watts, J. D., Kimball, J. S., Jones, L. A., Schroeder, R., & McDonald, K. C. (2012). Satellite Microwave remote sensing of contrasting surface water inundation changes within the Arctic-Boreal Region. *Remote Sensing of Environment*, *127*, 223–236. https://doi.org/10.1016/j.rse.2012.09.003

Webb, T. (2014, June 22). Heavy rains take toll on Minnesota crops . *Saint Paul Pioneer Press.* Retrieved from https://search-proquest-com.ezproxy.lib.purdue.edu/docview/1539523457?pq-origsite=summon

Yang, G., Bowling, L. C., Cherkauer, K. A., & Pijanowski, B. C. (2011). The impact of urban development on hydrologic regime from catchment to basin scales. *Landscape and Urban Planning*, *103*(2), 237–247. https://doi.org/10.1016/j.landurbplan.2011.08.003

Yapo, P. O., Gupta, H. V., & Sorooshian, S. (1998). Hydrology Multi-objective global optimization for hydrologic models. *Journal of Hydrology*, *204*, 83–97.

3. EVALUATING SEASONAL TRENDS AND FREQUENCY OF PEAK FLOW IN THE RED RIVER BASIN

Abstract

The Red River of the North basin is prone to inundated land area (ILA) and flooding due to the flat terrain, low soil permeability and influence of soil freeze/thaw action. In a region that is experiencing a changing climate, understanding the propensity of peak flow events is critical for agricultural producers and water resource managers. In this study, the Variable Infiltration Capacity (VIC) model with a transferable parameterization to simulate streamflow and ILA are used to analyze seasonal trends, occurrence and magnitude of peak flow events in the Red River basin and compared with observed streamflow and ILA from the MODIS Near-Real Time Global Flood Mapping product. We test for trend and rate of change of peak flow events at six gaging stations within the Red River basin using the Mann-Kendall test and Sen slope estimator, respectively. The occurrence and magnitude of peak flow events are analyzed using peaks over threshold and flood frequency, where observed results are compared with the VIC model under difference scenarios (ILA and No ILA). Results show an increasing trend of summer peak flow events within the Red River basin, and a shift in occurrence of peak flow events from the spring season (unimodal) to spring and summer seasons (bimodal). The transferable parameterization simulates streamflow and ILA satisfactorily and the results demonstrate the importance of the ILA parameterization in representing the shift and seasonal occurrence of peak flow events as well as range in magnitude.

3.1 Introduction

Understanding the occurrence and magnitude of flooding is important in the Upper Midwest, where a changing climate and land use affect streamflow and can shift occurrence and magnitude of peak flow events. For instance, the Red River of the North basin, which is a low gradient basin, is prone to inundated land area (ILA) and flooding (Figure 3.1) due to extreme rain events, snowmelt and the influence of frozen soils. From 2000 to 2013, the Red River basin experienced major flooding in 11 of the 13 years. In addition, the tributaries of the river have experienced both 100-year and 500-year flood levels during this time period (Commission, 2011; USACE, 2017).

This predominantly agricultural area is located in the Upper Midwest within the states of Minnesota, North Dakota and South Dakota. The seasonal occurrences of ILA can have a water depth of less than one meter yet expand up to hundreds of square meters and water may remain stored on the surface up to a week or longer, until it slowly drains through the subsurface or evaporates (Grimm et al., 2018; Shook et al., 2011). Previous flood events in the basin have occurred mainly in the spring, where damages caused by the floods have reached financial costs as high as 4 billion dollars (Commission, 2011; Tuttle et al., 2017). According to the 2015 U.S Army Corps of Engineers regional climate change impact assessment report, annual precipitation is projected to increase in the Red River basin. The findings in the report suggest that the increase in annual precipitation events will coincide with an increase in temperature, causing a decrease in snow water equivalent (SWE) (Alberto et al., 2015). With a changing climate in the low-gradient region, the increase in precipitation can impact crop production in the summer and fall from a temporal shift in flood patterns, resulting in an increasing frequency in summer and fall peak flow events.

Figure 3.1: View of inundated land area in the Red River Basin. Photo taken in May 2013.

Peak flow events are often linked to their hydrometeorological settings, though climate, land use and land cover changes can also influence the occurrence and magnitude of peak flow (Villarini

et al., 2011). Cunderlik et al. (2009) studied the Red River basin and found historical peak flow events were most common in the spring season due to snowmelt, while in recent decades there has been a shift with more peak flow events occurring in the fall season associated with excess rainfall. In a more recent study of peak flow in the basin, Kelly et al. (2017) found an increase in magnitude of peak flow events, beginning in the mid-1990's. The in-field flooding resulting from excess water can affect the occurrence and magnitude of flood propagation as well as impact crop production in low gradient agricultural areas.

In order to understand the changing nature of flood occurrence in this low gradient environment, it is necessary to use a model that explicitly represents the ILA. Previous studies in the Red River basin have used observed data such as precipitation, temperature and discharge data to investigate hydrologic changes resulting from changes in climate and land use and land cover (Kelly et al., 2017; Kunkel et al., 2013; Villarini et al., 2011). However, separating and measuring the influence of each on streamflow is difficult with observed data. Hydrologic models can be used to parse and measure the influence of land use and land cover on streamflow or changes in climate on streamflow. These models can also be used to assess the potential impacts from changes in land use, land cover and climate on flood frequency (Alberto et al., 2015). For instance, large-scale models that calculate water and energy fluxes and represent land use change such as the installation of subsurface drainage, have been used to analyze the influence of climate and land use and land cover changes on streamflow in the Red River basin (Liu et al., 2015; Rahman et al., 2014). Previous studies have analyzed the influence of lakes and wetlands on streamflow with hydrologic models that can represent temporary storage (Bowling et al., 2010; Mishra et al., 2010). However, few studies have investigated the effects of ILA on streamflow using hydrologic models that can represent temporary storage of water on the land surface while also simulating constant land use and land cover. In a region where a changing climate may lead to more frequent extreme summer rain events and flooding that can impact stakeholders, further research is needed in order to determine how a changing climate and ILA are influencing the seasonality and magnitude of flood events in the Red River of the North. The reported changing climate and history of flooding makes the Red River basin a good case to understand the occurrence and magnitude of peak flow events and is the focus of this study. The objectives of this study are to: (1) Assess model performance to represent observed streamflow and ILA in the Red River basin using statistical measures, (2)

Analyze observed seasonal trends and investigate observed shifts in magnitude and timing of peak flow events in a region experiencing a changing climate, (3) Evaluate how ILA influences the magnitude and occurrence of peak flow events using a hydrologic model capable of representing ILA.

3.2 Data and Methods

3.2.1 Data

In this study, measured daily discharge from six United States Geological Survey (USGS) gaging stations within the Red River basin and a period of record with at least 57 years were used in the analysis (Table 3.1(U.S. Geological Survey, 2018).

Table 3.1: United States Geological Survey (USGS) gaging locations within the Red River basin used for analysis.

USGS Gaging Locations	Drainage area (km^2)	Period of record (water years)
USGS 05092000 Red River of the North at Drayton, ND	90,132 km^2	1936-2018
USGS 05064500 Red River of the North at Halstad, MN	56,462 km^2	1961-2018
USGS 05054000 Red of the North at Fargo, ND	17,612 km^2	1901-2018
USGS 05062000 Buffalo River Near Dilworth, MN	2,525 km^2	1931-2018
USGS 05061500 South Branch Buffalo River at Sabin, MN	1,176 km^2	1945-2018
USGS 05061000 Buffalo River Near Hawley, MN	841 km^2	1945-2018

The location of each gaging station used in this study is shown in Figure 3.2. Watersheds range in size from small (841 km^2) to large (90,132 km^2) (Table 3.1). The watersheds are all nested within the larger Red River basin. Discharge from Sabin, MN and near Hawley, MN flow merge into the

Buffalo River station near Dilworth, MN. The Buffalo River and the Red River at Fargo, ND converge and flow through the gage at Halstad, MN. Discharge from all sub-watersheds flows through the gage at Drayton, ND (Figure 3.2).

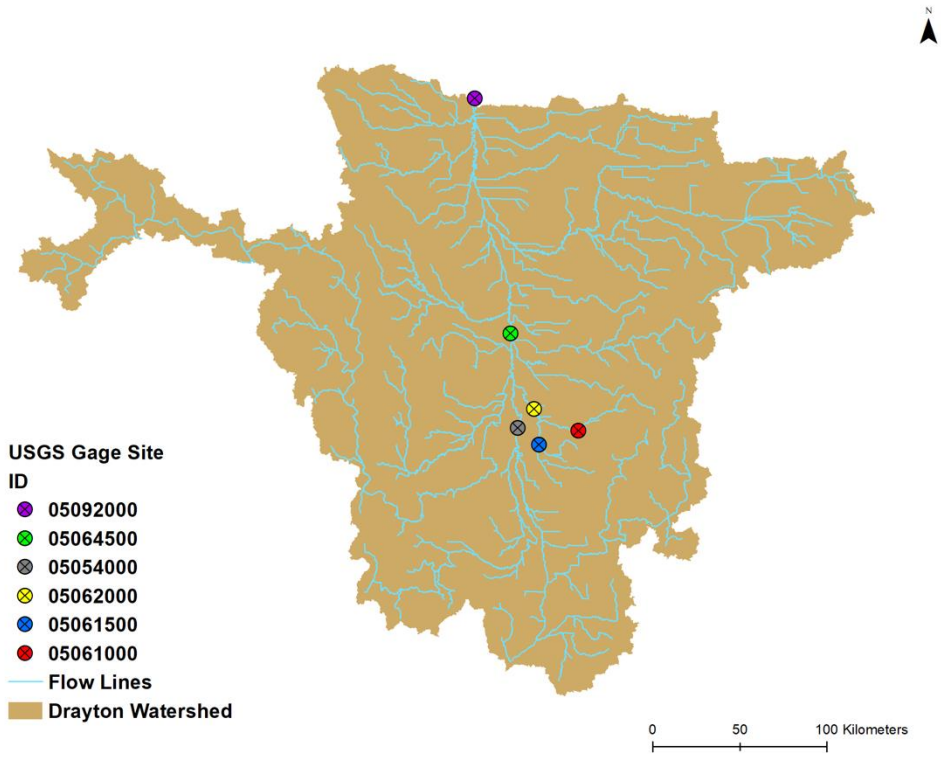

Figure 3.2: Location of gaging stations used in study along with flow lines. Drayton, ND (05092000), Halstad, MN (05064500), Fargo, ND (05054000), Dilworth, MN (05062000), Sabin, MN (05061500), Hawley, MN (05061000).

The extent of ILA was determined for the region using the MODIS Near Real-Time (NRT) Global Flood Mapping product. The MODIS data used for this study were a daily product generated from a two-day composite (2D2OT) where the observation date was the last date of observation. The flood product had a 250 m resolution and consisted of four classes with non-flooded and flooded surfaces identified. Pixels with insufficient data such as cloudy or bad data were described as Class 0. High cloud coverage (Class 0) retrievals greater than 30% within the watershed were removed. Pixels with no water detected corresponded with Class 1. Pixels that coincided with the MODIS land water mask (MOD44W) were considered to be the reference water extent but not flooded were Class 2. The reference water extent oscillated over time; a permanent water fraction was estimated using the 90th percentile of data with low cloud coverage (<10%). Pixels that were

identified beyond the reference extent were likely flooded and labeled as Class 3 (Nigro et al., 2014). For this work, pixels were classified as inundated land area by calculating the difference between the MODIS total water fraction (Class 2 and Class 3) and the estimated permanent water fraction. The MODIS imagery was then used to estimate fractional extent of ILA for a model grid cell of 1/8th degree latitude and longitude.

3.2.2 Detecting trends and shifts

Nonparametric tests were used to determine if evidence of increasing trend in the magnitude of peak flow events could be detected within the Red River basin. Each gaging station was evaluated for statistical significance of trend and rate of change in the annual maxima series using the Mann-Kendall test and Sen slope estimator, respectively. The annual maxima series was then sub-divided to evaluate the annual maxima during the spring and summer seasons. The spring season was selected because peak flow events commonly occur in the spring in the Red River basin. The summer season was selected to investigate if a change in trend in peak flow from spring to summer could be detected, which may impact crop production in the growing seasons. Spring months evaluated were March and April, while Summer months evaluated were June and July. The seasonal analysis to test for trend and magnitude of peak flow events was conducted for a 50-year period from water years 1969 to 2018.

Peaks over threshold (POT) can be used to characterize the occurrence of peak flow events with respect to time and help determine if peak flow events are shifting in response to a changing climate. POT was used to assess the occurrence of peak flow events and determine if a shift in occurrence of peak flow could be identified seasonally. POT was assessed annually using the largest watershed at the Drayton, ND gaging station. The period of analysis was water years 1984 to 2015. The number of peak occurrences were also evaluated monthly for two time-periods (1984 to 1999 and 2000 to 2015) to identify seasonal shifts of peak flow. A hydrologic model was compared with the observed data over the same period to determine if a similar shift in occurrence of peak flow could be represented using a model that does not simulate change in land use.

3.2.3 Model calibration and evaluation

The Variable Infiltration Capacity (VIC) model is a large scale hydrologic model which quantifies the water and energy balance of a watershed as discrete grid cells (Cherkauer et al., 2003; Liang et al., 1994). A limitation of previous hydrologic models used in the Red River was the inability to simulate ponding on the land surface (NWS, 1998). The VIC model has the ability to simulate local ponding features with inclusion of a lake and wetland algorithm (Bowling et al., 2010). A parameterization was developed to represent the depth-area relationship of inundated land area in a sub-catchment of the Red River basin using remotely sensed observations (Smith et al., 2020). In this study, we extend the parameterization developed in the Buffalo River watershed to the greater Red River basin with as outlet at Drayton, ND using additional MODIS observations. Figure 3.3 shows the spatial distribution of the maximum fractional ILA within the Red River basin. The inundation extent is highest along the main stem of the river and decreases with distance from the stem of the river to the uplands. The isolated inundated areas in the northwest are associated with wetlands and lake. In the northeast is a larger lake with grid cells removed and is not represented within the VIC simulations.

In the Red River basin, ice jams can cause overbank flow along the stem of the main channel. The VIC model does not simulate overbank flow, as a result, grid cells associated with overbank flow were identified and removed from analysis. Simulated grid cells that had overbank flow extending greater than 10% within the grid cell were masked from evaluation of ILA (Figure 3.3). The overbank flow extent was estimated at 1km for each bank of the main channel, for a total width of 2 km. Grid cells were identified and overbank flow extent estimated using a combination of remotely sensed observations, discharge records and local government agency reports of overbank flow observations. MODIS observations with high estimates (>50%) of ILA within a grid cell were identified as areas likely experience overbank flow. Record notes of the discharge data were analyzed with dates corresponding to areas likely to experience overbank flow to confirm high ILA observations were due to overbank flow. The extent of overbank flow was estimated using local agency reports with geotagged images and observation notes, where the distance of observed overbank flow was measured at approximately 1 km away from the main channel near Halstad (USGS 05064500).

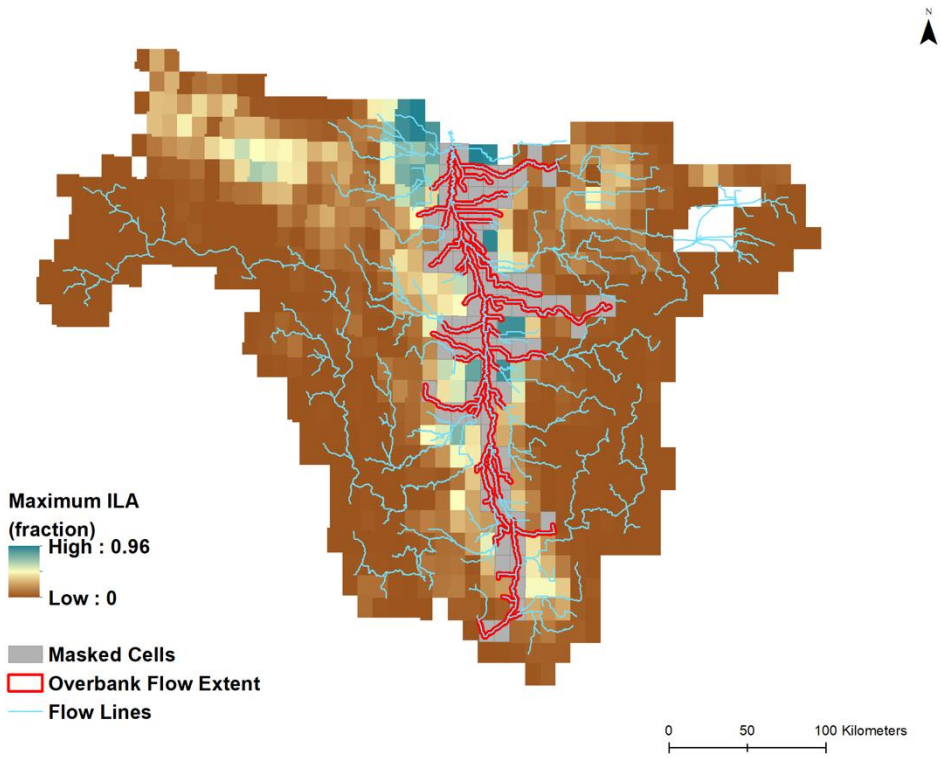

Figure 3.3: Maximum extent of inundated land area determined from the MODIS global flood mapping product and rescaled for the 1/8th degree VIC model grid cells used in this analysis.

The VIC model was calibrated for the Red River at Drayton from water years 2006 to 2009 and evaluated from water years 2010 to 2014. MODIS imagery depicting ILA was available from water years 2006 to 2014. Discharge data was matched with available ILA data in order to analyze and assess model performance of simulated discharge and ILA during low and high flow periods. A GIS based routing model was used to compare simulated and observed discharge (Yang et al., 2011). Model parameters developed by Smith et al. (2020) for the Buffalo River near Dilworth, a subcatchment of the Red River (Figure 3.2), were used to parameterize the Red River basin. Adjustments were made to the soil parameter file to improve representation of spring peak flow events and interim low flow periods.

Table **3.2** lists the calibrated VIC model parameters. Model performance was assessed for discharge using Nash-Sutcliffe efficiency (NSE), the NSE of the natural log data (LNSE) and percent bias (PBIAS). Model performance was assessed for ILA using root mean square error (RMSE).

Table 3.2: Calibrated VIC model parameters. The lake and wetland parameters were not used for the No ILA scenario.

Parameter name	Description	Calibrated value
b_infil	Variable infiltration curve parameter, no units	0.17
Ds	Value at which non-linear baseflow begins, listed as a fraction of Dsmax	0.005
Dsmax	Maximum velocity of baseflow, listed as mm/day	12.0
Ws	Maximum soil moisture where non-linear baseflow begins, listed as a fraction	0.99
wfrac	Width of lake outlet, listed as a fraction of the lake perimeter	0.0002
rpercent	Runoff that enters lake and wetland, listed as a fraction of the grid cell	2.73×fractional ILA

3.2.4 Flood frequency

During peak flow events, the temporary storage of water on the land surface reduces flood magnitude by delaying runoff to nearby channels. Representing the influence of inundated land area on the magnitude and occurrence of peak flow events can improve predictive estimates of peak flow events for different return periods. The effects of ILA on the annual maxima series were analyzed using flood frequency diagrams for the observed and routed streamflow from water years 1984 to 2015. Two simulation scenarios were used to evaluate the effects of ILA on streamflow, one with ILA represented (ILA) and one with no ILA representation (No ILA). In the ILA scenario, the lake and wetland algorithm was activated, whereas in the No ILA scenario, the lake and wetland algorithm was not activated. The flood frequency of both scenarios was compared with the observed data to evaluate how the representation of surface ponding impacts flood magnitude and compares with observed data for a range of flood sizes. Flood magnitudes for return periods of 2, 5, 10, 25, and 50 years were evaluated. The Cunnane plotting position was used with the

extreme value type-I (EVI) distribution to evaluate the flood frequency (Cunnane, 1978; Fisher et al., 1928).

3.3 Results

3.3.1 Model performance

Model performance for the discharge calibration and evaluation period are listed in Table 3.3 and shown in Figure 3.4. For the calibration period (2006-2009), the NSE, LNSE and PBIAS are 0.61, 0.42 and 13%, respectively. As shown in Figure 3.4, the magnitude of spring and summer peak flow events are well represented with the exception of the spring event in 2006. Simulated discharge during spring events also simulates a short delay in the timing of peak flow compared to the observed discharge. The interim low flow periods show that simulated discharge is slightly overestimated. For the evaluation period (2010-2014), the NSE, LNSE and PBIAS are 0.63, 0.57 and -4%, respectively. For the evaluation period, simulated baseflow is improved and peak flow events are well represented. While assessing water years 1984 to 2015 shows that the overall fit of simulated is satisfactory, there is a tendency to underestimate peak flow events.

Table 3.3: Model performance for the calibration and evaluation periods.

Parameterization	Calibration (2006-2009)				Evaluation (2010-2014)			
	NSE	LNSE	PBIAS (%)	RMSE (%)	NSE	LNSE	PBIAS (%)	RMSE (%)
Discharge	0.61	0.42	13		0.63	0.57	-3	
ILA				1				0.8

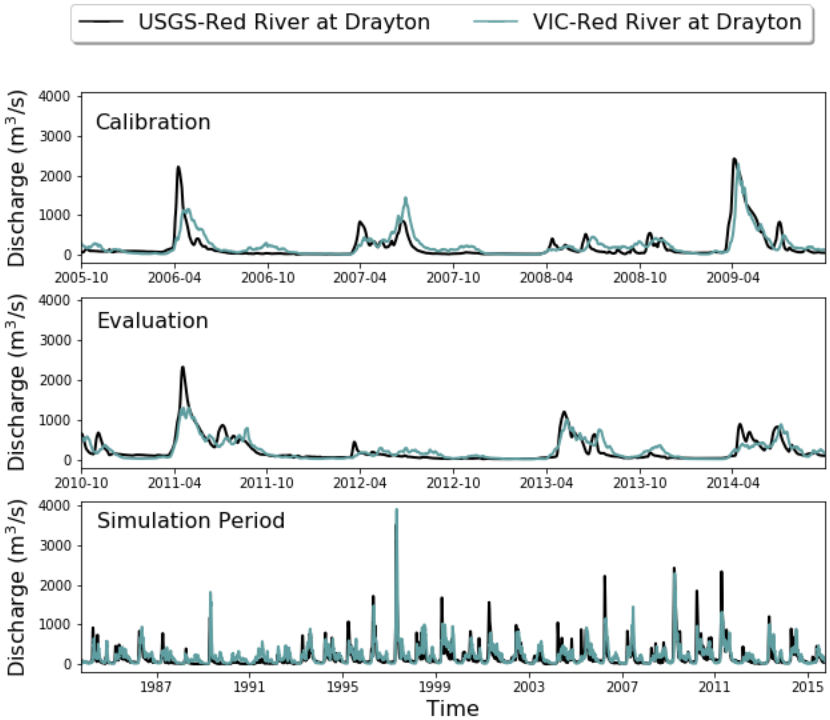

Figure 3.4: Time series of daily simulated and observed discharge (m^3/s) for calibration (water years 2006-2009), evaluation (water years 2010-2014) and the simulation period (water years 1984 to 2015).

Model performance of simulated ILA for the calibration and evaluation periods are listed in Table 3.3 and shown in Figure 3.5. For the calibration and evaluation periods, the RMSE is 1% and 0.8%, respectively. As shown in Figure 3.5, simulated ILA shows a similar seasonal response to the observed ILA, where ILA increases in the spring from snowmelt over frozen soils and is associated with the larger peak flow events represented in Figure 3.4. For spring events, the timing of simulated ILA is well represented, but it underpredicts the magnitude. In the transition from spring to summer, ILA is associated with excess rainfall where ILA and discharge are lower compared to the spring (Figure 3.4 and Figure 3.5). The timing of simulated ILA for summer flood events is again well represented, but generally overpredicts the magnitude in response to the summer rainfall (Figure 3.5).

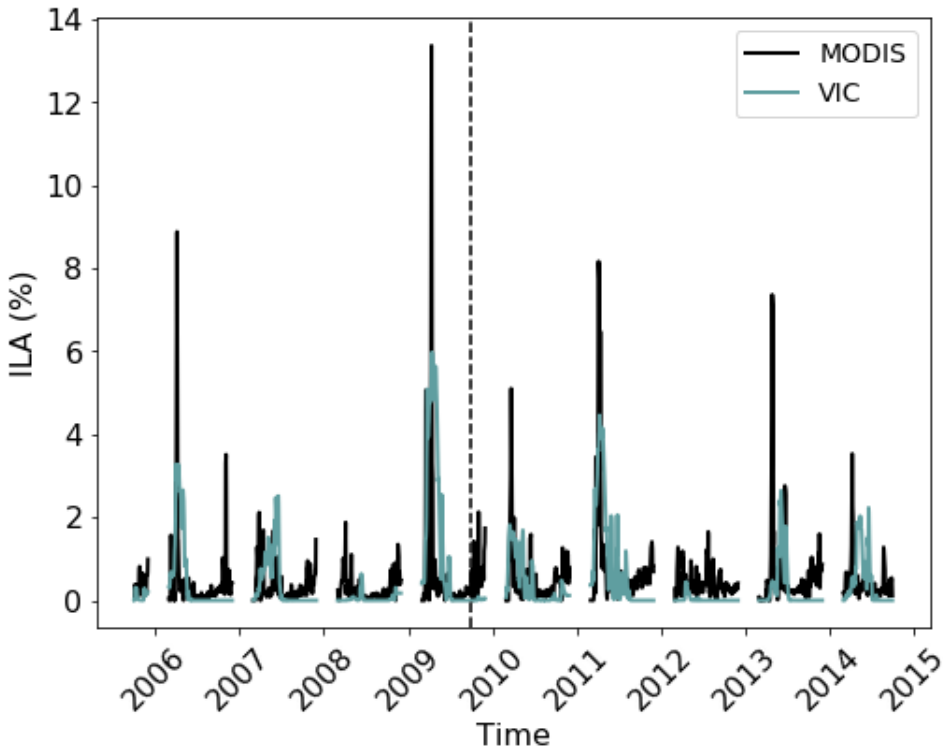

Figure 3.5: Time series of simulated and observed inundated land area (%) over calibration (2006-2009) and evaluation (2010-2014) periods, separated by the dotted line.

3.3.2 Annual trend and magnitude

The tests for significance of trend and magnitude using the Mann-Kendall test (a=0.1) and computed Sen slope estimator ($m^3 s^{-1} yr^{-1}$) for the observed annual maxima series (1969-2018) are listed in Table 3.4. Overall, two of the six gaging stations had statistically significant increasing trends. These stations were Halstad and Fargo, which are located on the mainstem of the Red River, and both experienced a noticeable increase in peak discharge rate with Sen's slope values of 5.6 $m^3 s^{-1} yr^{-1}$ and 2.5 $m^3 s^{-1} yr^{-1}$, respectively. Gaging stations in upstream locations of the Red River did not have statistically significant trends. Sen slope estimates range from 0.03 $m^3 s^{-1} yr^{-1}$ (Hawley) to 5.6 $m^3 s^{-1}$ per yr^{-1} (Fargo).

Table 3.4: Mann-Kendall (a=0.1) and Sen slope estimators for the listed gaging stations calculated using the annual maxima series from water years 1969 to 2018.

Gaging Station	p-value	Sen slope estimator ($m^3 s^{-1} yr^{-1}$)
Drayton, ND	0.53	2.7
Halstad, MN	*0.09	5.6
Fargo, ND	*0.07	2.5
Dilworth, MN	0.63	0.2
Sabin, MN	0.55	0.2
Hawley, MN	0.95	0.0

3.3.3 Seasonal trend and magnitude

Further evaluation of tests for trend and magnitude during spring (March and April) and summer (June and July) seasons are listed in Table 3.5 using the Mann-Kendall (a=0.1) and Sen slope estimate. For period of analysis (1969-2018) trends were evaluated for the largest seasonal flood per year during the spring and summer seasons at all gaging stations. Table 3.5 show the results of the Mann-Kendall test and Sen slope estimator (m^3 s-1 yr^{-1}) for spring and summer periods. For the spring period, there are no statistically significant trends identified for any of the gaging stations. This is evidence that over the period of analysis the size of the largest spring flood did not substantially change within these watersheds.

The analysis of the summer season (June and July) found statistically significant increases in the magnitude of peak flow events (Table 3.5) over the period of analysis. Interestingly, the trend magnitude increases from the smaller subcatchments in the south towards the river basin outlet to the north (Figure 3.6). The gaging station at Drayton has an increase in magnitude of peak flow during summer months of 8.5 $m^3 s^{-1} yr^{-1}$. This degree of change is substantial as it equates to 6% of the annual average discharge at the Drayton gaging station.

Table 3.5: Results of Mann-Kendall Test and Sen slope estimator from annual maximum discharge during the spring (March and April) and summer (June and July) season (a=0.1) from water years 1969 to 2018.

	Spring		Summer	
Gaging Station	p-value	Sen slope estimator ($m^3 s^{-1} yr^{-1}$)	p-value	Sen slope estimator ($m^3 s^{-1} yr^{-1}$)
Drayton, ND	0.85	1.2	*0.0023	8.5
Halstad, MN	0.43	2.1	*0.0010	5.4
Fargo, ND	0.26	1.3	*0.0001	2.6
Dilworth, MN	0.82	0.1	*0.0002	0.6
Sabin, MN	0.75	0.1	*0.0006	0.5
Hawley, MN	0.79	0.0	*0.0037	0.2

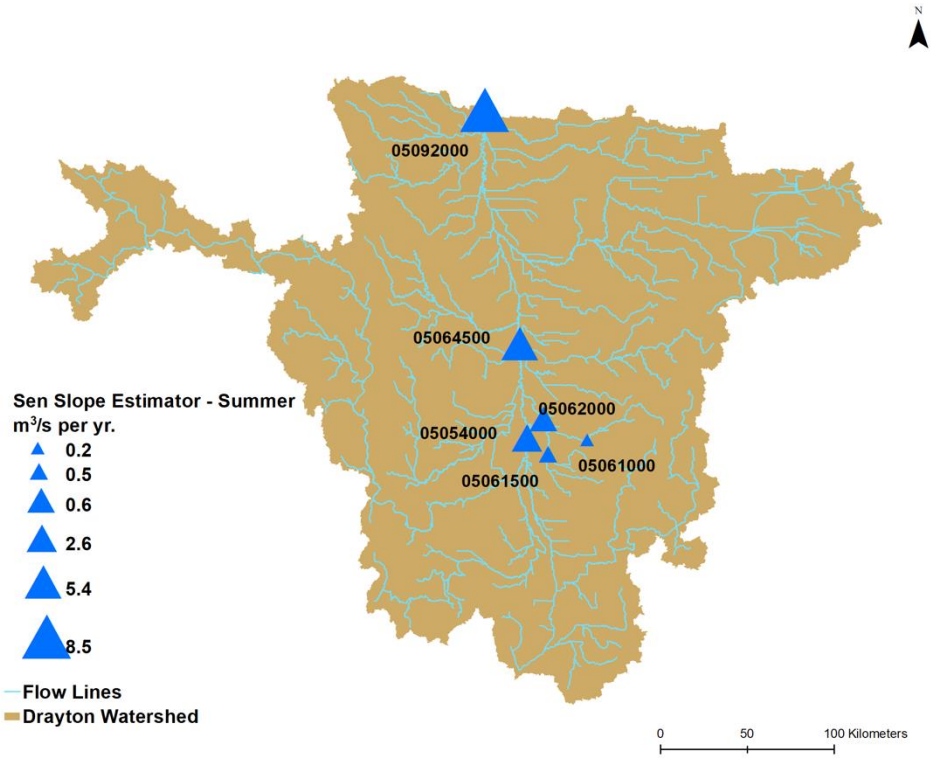

Figure 3.6: Sen slope estimator (m^3/s per yr.) for summer season showing magnitude of floods increasing northward from uplands to main river channel.

3.3.4 Change in the frequency of peak flow events

The change in the frequency of peak flow events both annually and seasonally is assessed using peaks over threshold (POT) analysis. The annual POT series was calculated for observed streamflow on the main stem of the Red River using the USGS gaging station as Drayton, ND (Figure 3.7). The threshold was set at 500 m^3/s to increase the number of peak flow events under analysis beyond the annual maxima series by analyzing moderate and large flood events. This resulted in a total of 53 events that exceeded the threshold between water years 1984 and 2015. The frequency of exceedance gradually increases over the 32-year period, with half of the POT events occurring on or after 2003, so in the final 13 years. The increase in occurrence begins in the mid-1990s, with one or more event occurring in all but two years after 1993.

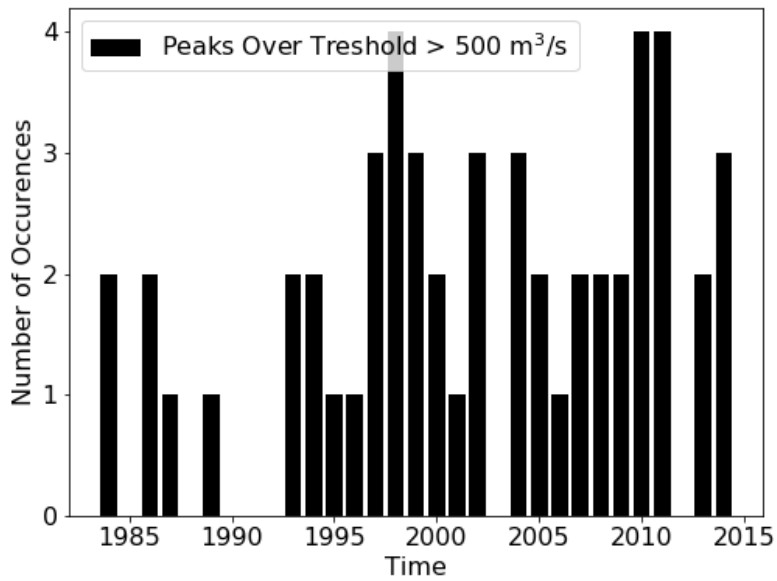

Figure 3.7: Annual peaks-over-threshold at the Red River at Drayton gaging station (05092000). Water years evaluated ranged from 1984 to 2015. Threshold value was set at 500 m^3/s to analyze moderate and large peak flow events. The linear fit model in red shows an increase of peak flow events over the simulation period.

To evaluate seasonal shifts in the occurrence of peak flow events, the number of observed monthly POT for the first 16 years of record is plotted against the number of POT events for the final 16 years of the series for the Red River at Drayton, ND (Figure 3.8a). The monthly POT series was constructed by identifying events where daily flow exceeded the threshold, still set at 500 m^3/s,

for each month. The total number of events is equal to that on the annual plot (53 events), but 22 events occurrences in the first 16 years versus 31 in the second 16 years.

The observed earlier period (1984 to 1999) has a unimodal structure, with flood events occurring predominantly in the spring season. In the later period (2000 to 2015) there is a shift from a unimodal structure to a bimodal structure, where floods are occurring in both the spring and summer seasons. Most notably, five or more peak flow events occur in the months of April in the spring season and June and July in the summer season for the second half of the observational record. Five or more floods occur only in April in the first half of the record. In addition, during the second half of the analysis period, there are five POT occurrences in October and November, compared to none in the first half of the analysis period. The region has consistently experienced flooding events in spring that can hamper planting, but more recently flooding events are occurring more frequently in the summer and fall months. These months are also important for crop production and harvesting, so increased flooding potential can leave crops more susceptible to damage and yield loss.

In order to more clearly ascertain the role of surface inundation and storage on these shifts, we applied the calibrated VIC model with and without the representation of ILA to the whole Red River basin. Using the same threshold value (500 m^3/s) applied to the observed stream discharge, monthly POT series were computed for both the No ILA (Figure 3.8b) and ILA (Figure 3.8c) parameterizations. When ILA is not represented (No ILA) simulated POT events shift from spring dominance to summer dominance between the first and second halves of the period of analysis. Five or more events occurred in April, June and July in the first 16-year period, and for the months of April through July with a peak in June for the second 16-year period. In addition, no distinguishable shift in structure from unimodal to bimodal was identified. As the No ILA simulation simulates no surface storage in lakes, wetlands or on fields, there is no storage reducing the magnitude of peak flow events nor contributing to a seasonal shift in flood occurrence (Figure 3.8b).

When ILA is represented in the model (Figure 3.8c), POT events are overestimated for the month of July, but the seasonal variation is in greater agreement with the USGS data (Figure 3.8a).

Specifically, 5 or more POT events occur in April and July for the early 16-year period, and for April, June, July and August for the later 16-year period. This illustrates the shift in seasonality of peak flow events from a unimodal to bimodal structure that is represented in the observed data. As the climate data is the same between model simulations, the difference in the number and distribution of POT events can be directly attributed to the representation of land surface storage. The temporary storage of water in the landscape, causes a reduction of discharge to nearby streams. The POT results from simulations with ILA, demonstrate the ability of the parameterized model to capture the observed change in POT structure (unimodal to bimodal).

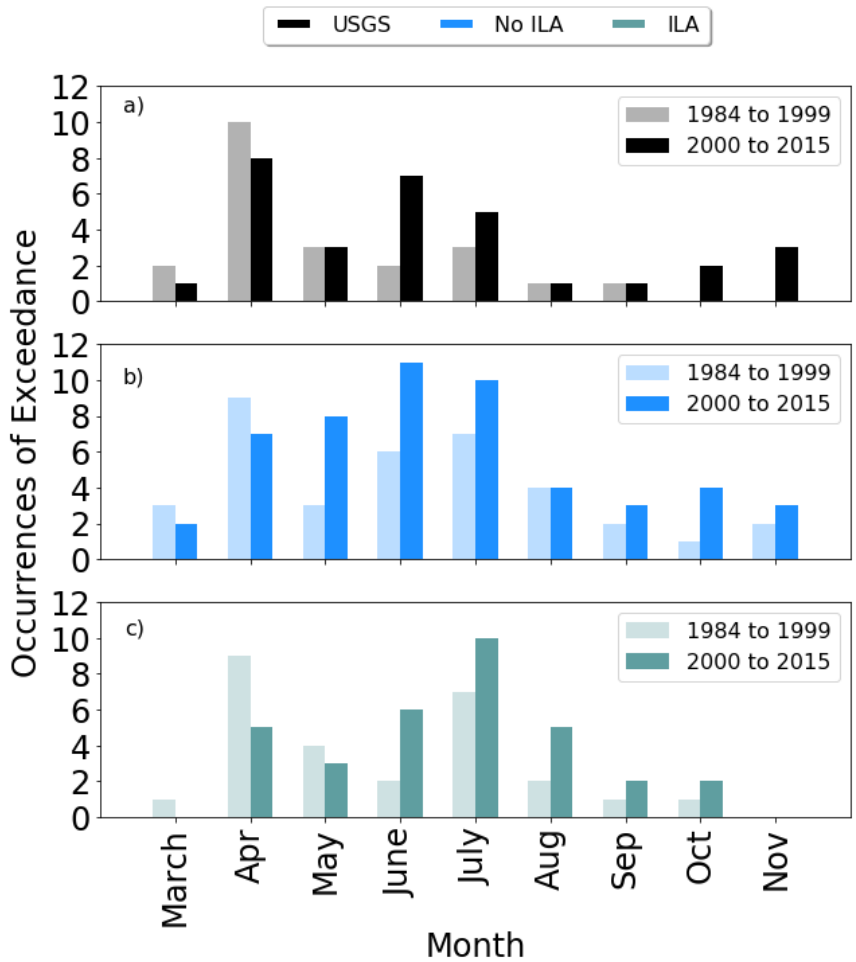

Figure 3.8: Count of peaks-over-threshold (threshold at 500 m^3/s) on a monthly scale at the Red River at Drayton, ND over the water years 1984 to 2015 for a) USGS, b) No ILA and c) ILA. Simulating inundated land area (ILA) shows a similar shift in structure from spring flood events (unimodal) to spring and summer flood events (bimodal) observed in the USGS data. Conversely, to the No ILA scenario, no shift from unimodal to bimodal flood events is simulated.

3.3.5 Flood frequency

To assess the role of ILA on flood magnitude, the estimated return period of annual maximum peak flow events was plotted for observed and simulated discharge for the Red River at Drayton, ND (Figure 3.9). From this flood frequency curve, it can be seen that the No ILA simulation has a steeper slope compared to those fits for the USGS observations and the ILA simulations. For return periods greater than 2 years, the No ILA scenario overestimates flood magnitude, and the overestimation becomes greater as the return period increases. The ILA scenario underpredicts the observed flood frequency curve, but the magnitude of the underprediction is relatively consistent. The influence of ILA on peak flow simulation is most significant at the 50-year return period (Figure 3.9), where the percent difference of the flood magnitude from the No ILA and ILA scenarios with respect to the USGS observations are 23% and -8%, respectively. By representing ILA in model simulations, we are able to reduce bias and improve representation of a greater range of peak flow events.

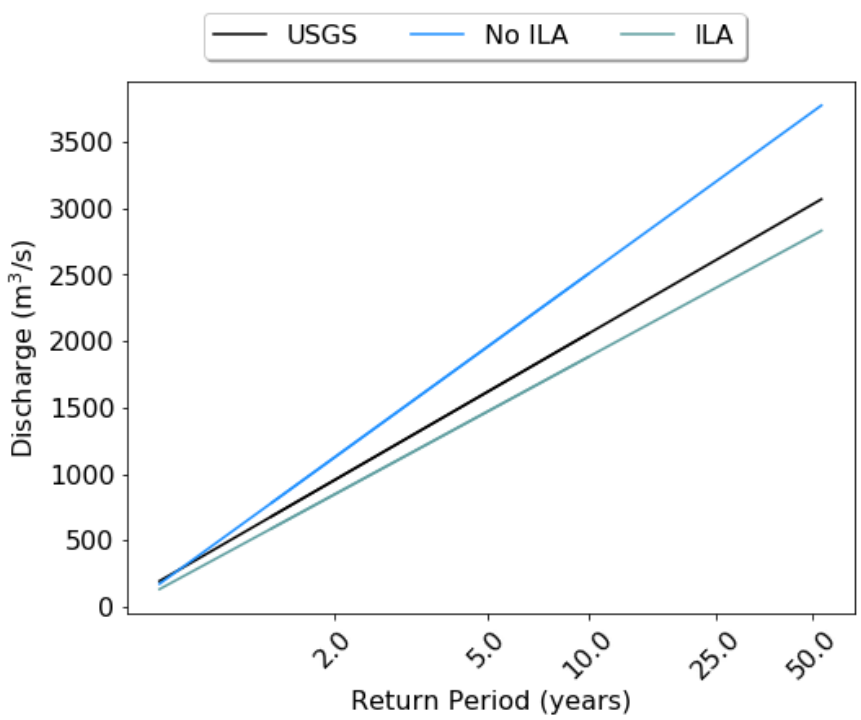

Figure 3.9: Analyzing the influence of local ponding on flood magnitude by comparing flood frequency from parameterizations representing inundated land area versus No ILA flood frequency.

3.4 Discussion

In this study we analyze the seasonal trends, frequency and magnitude of peak flow events in the Red River of the North basin to enhance our understanding of the influences of a changing climate compounded with land use and land cover changes on downstream flow. By explicitly representing ILA in a hydrologic model and comparing results with observed data and a simulation scenario not representing ILA, we are able to better understand the effects temporary water storage on the landscape has on the occurrence and magnitude of peak flow events in the basin.

The model was parameterized using settings developed from a nested catchment within the Red River basin (Smith et al., 2020), and assessed using observed discharge and ILA data. Though parameter adjustments were made to the soil parameter file to improve simulation of spring peak flow events, the parameter settings from Smith et al. (2020) provide a useful baseline to represent simulated streamflow and demonstrate the transferability of the parameters developed for a smaller sub-watershed (USGS 05062000) when applied to a larger watershed (USGS 05092000). Model performance of simulated streamflow is satisfactory with NSE above 0.6 and PBIAS below 15% for separate calibration and validation periods. In general, the model tends to underpredict spring peak flow events, yet capture historical spring peak flow events such as the spring floods in 1997 and 2009. The model results are comparable to previous studies analyzing streamflow in the Red River basin (Liu et al., 2015; Rahman et al., 2014). Liu et al. (2015) also underestimates the spring 2006 event and suggests the underestimation may be due to limitations of the SWAT model that were beyond the scope of the study. In this study, the parameters used to represent the temporary storage were developed by Smith et al. (2020). The model tends to underestimate ILA during spring events, similar to the results found in Smith et al. (2020). The reported RMSE is similar to that of previous studies that estimated ILA over cropland regions (Du et al., 2018; Sun et al., 2011). Simulated ILA is able to represent the seasonal variation of surface inundation observed in the spring and summer seasons resulting from snowmelt over frozen soils and excess rainfall, respectively. The MODIS ILA data used as the reference is also an estimate, where land cover and cloud coverage impacts retrievals (Policelli et al., 2017). Overall, the simulated ILA represents timing and magnitude of ILA satisfactorily and demonstrates the transferability of the ILA parameters.

The comparison of spring and summer peak flow with tests for trend magnitude demonstrate that there is an increase in peak flow events in summer months over the 50-year analysis period. All gaging stations assessed in upstream locations and along the main stem of the Red River have statistically significant increasing summer peak flow events. Peak flow events in the spring remain dominant with no evidence of trend as shown by the results of the peaks over threshold and Mann-Kendall test, respectively. Previous studies have also investigated streamflow metrics seasonally within the Red River basin (Kelly et al., 2017; Villarini et al., 2011). Villarini et al. (2011) evaluated the spatial heterogeneity of peak flow events in the Midwest and demonstrated that peak flow events within the Red River basin occur predominantly in the spring. Kelly et al. (2017) examined the five-year running average (1935-2013) of 22 gaging stations in the Red River basin. They found an increase in daily peak flow for the spring and summer, with daily peak flow changing least in the spring and increasing most in the summer.

Further analysis into the timing and frequency of peak flow events reveal a shift in peak flow from a unimodal structure, where peak flow events occur predominantly in the spring season to a bimodal structure, where floods are occurring in both the spring and summer/fall seasons. The shift is observed at the Red River at Drayton, the largest watershed used in our study. Previous research has analyzed the unimodal and bimodal occurrence of peak flow events in low gradient areas (Cunderlik et al., 2009). Cunderlik et al. (2009) investigated trends in peak flow events in the lowlands of Canada and identified bimodal flood seasonality at gaging stations in Manitoba, a province north of the Red River basin. In their study, the primary season of flood occurrence is the spring (April-May) resulting from snowmelt, followed by peak flow events in the fall (August-October) from high intensity rainfall events (Cunderlik et al., 2009). Kelly et al. (2017) suggest that climate change plays a role in influencing the increase in peak streamflow within the Red River basin, but isolating effects of climate alone on peak flow is difficult due to the contributing influences of land use and land cover changes. The VIC model used in this study represented a constant land use and land cover for the region for the period of analysis. The VIC simulation with represented ILA captures the observed shift in peak flow events from peak flow events occurring predominantly in the spring season to an increase in peak flow events occurring in both the spring and summer seasons. The ILA scenario overestimates the occurrence of peak flow events in July. The overestimation is likely the result of the model's overresponse to summer rainfall events.

Future studies may work to improve simulated discharge in the targeted month. The findings of the timing and frequency of peak flow provide supporting evidence to the studies of Cunderlik et al. (2009) and Kelly et al. (2017) that the shift from a unimodal structure to bimodal structure is likely the result of increases in precipitation intensity in summer months.

The effects of ILA on peak flow are distinguishable in the occurrence of exceedance (Figure 3.8) and flood frequency diagrams (Figure 3.9). The results comparing the occurrence of exceedance on a monthly time scale with the ILA and No ILA scenario demonstrate the role ILA has on reducing flood magnitude. By not representing ILA in simulations the seasonal variation in peak flow events may be overlooked. Conversely, by representing ILA, the seasonal variation in simulated peak flow is well represented along with shifts in occurrence with the USGS data. In addition, the flood frequency for the range of return periods is more accurate when simulating with ILA than simulating without. The parametrization used to represent the ILA in the VIC lake and wetland algorithm is from Smith et al. (2020), where we developed a depth-area relationship to represent the seasonally flooded land surface area in a subcatchment of the Red River basin using remotely sensed and in-situ data. The model performance results along with the scenario comparison using POT shows that the ILA parameterization improves simulation of low and high flow periods and is transferable to larger watersheds within the Red River basin.

3.5 Conclusion

In this study, we investigate the seasonal trends, magnitude and frequency of peak flow events in the Red River basin and use an existing large-scale hydrologic model to represent the seasonal variation in streamflow by representing ILA within the VIC model. Results of the study are the following:

1. Summer peak flow events are increasing within the Red River basin. Results of the Mann-Kendall test show statistical significance of increasing trend in summer peak flow events for all evaluated gaging stations. Spring flood events do not show a statistically significant trend.
2. A detected shift in peak flow occurrence is identified in the observed data within the time period of the study. The shift is from a unimodal structure to a bimodal structure, where

floods are occurring in the spring and summer seasons versus just in the spring season. The shift is also represented in simulated discharge when representing ILA.

3. Simulating ILA improves the estimation of flood frequency. Simulated flood frequency is greatly overestimated when ILA is not represented. For example, the 50-year return period flood is over-predicted by 23% when ILA is not represented, but it underpredicted by only 8% with the ILA parameterization.

3.6 References

Alberto, B., District, S. P., Banitt, A., & Faber, B. (2015). Red River of the North at Fargo, North Dakota, Pilot Study, Impact of Climate Change on Flood Frequency Curve. Retrieved from http://www.corpsclimate.us/docs/Red_River_of_the_North_Adaptation_Pilot.pdf

Bowling, L. ., & Lettenmaier, D. P. (2010). Modeling the Effects of Lakes and Wetlands on the Water Balance of Arctic Environments. *Journal of Hydrometeorology*, *11*(2), 276–295. https://doi.org/10.1175/2009JHM1084.1

Cherkauer, K. A., Bowling, L. C., & Lettenmaier, D. P. (2003). Variable infiltration capacity cold land process model updates. *Global and Planetary Change*, *38*(1–2), 151–159. https://doi.org/10.1016/S0921-8181(03)00025-0

Commission, R. R. B. (2011). *RED RIVER BASIN COMMISSION ' S LONG TERM FLOOD SOLUTIONS For the Red River Basin Final Report to the States of Minnesota Pursuant to Session North Dakota Chapter Counties Interstate Engineering*.

Cunderlik, J. M., & Ouarda, T. B. M. J. (2009). Trends in the timing and magnitude of floods in Canada. *Journal of Hydrology*, *375*(3–4), 471–480. https://doi.org/10.1016/j.jhydrol.2009.06.050

Cunnane, C. (1978). Unbiased plotting positions — A review. *Journal of Hydrology (Amsterdam)*, *37*(3–4), 205–222. article. https://doi.org/10.1016/0022-1694(78)90017-3

Du, J., Kimball, J. S., Galantowicz, J., Kim, S. B., Chan, S. K., Reichle, R., Jones, L. A., & Watts, J. D. (2018). Assessing global surface water inundation dynamics using combined satellite information from SMAP, AMSR2 and Landsat. *Remote Sensing of Environment*, *213*(March), 1–17. https://doi.org/10.1016/j.rse.2018.04.054

Fisher, R. A., & Tippett, L. H. C. (1928). Limiting forms of the frequency distribution of the largest or smallest member of a sample. *Mathematical Proceedings of the Cambridge Philosophical Society*, *24*(2), 180–190. https://doi.org/10.1017/S0305004100015681

Grimm, K., Tahmasebi Nasab, M., & Chu, X. (2018). TWI Computations and Topographic Analysis of Depression-Dominated Surfaces. *Water*, *10*(5), 663. https://doi.org/10.3390/W10050663

Kelly, S. A., Takbiri, Z., Belmont, P., & Foufoula-Georgiou, E. (2017). Human amplified changes in precipitation-runoff patterns in large river basins of the Midwestern United States. *Hydrology and Earth System Sciences*, *21*(10), 5065–5088. https://doi.org/10.5194/hess-21-5065-2017

Kunkel, K., Stevens, L., Stevens, S., Sun, L., Janssen, E., Wuebbles, D., Krunk, M., Thomas, D., Schulski, M., Umphlett, A., Hubbard, K., Robbins, K., Romolo, L., Akyuz, A., Pathak, T., Bergantino, T., & Dobson, J. (2013). *Regional Climate Trends and Scenarios for the U.S. National Climate Assessment Part 4. Climate of the U.S. Great Plains*. Washington D.C.

Liang, X., Lettenmaier, D. P., Wood, E. F., & Burges, S. J. (1994). A simple hydrologically based model of land surface water and energy fluxes for general circulation models. *Journal of Geophysical Research*, *99*(D7), 14,415-14,428. https://doi.org/10.1029/94JD00483

Liu, G., Schwartz, F. W., Tseng, K. H., & Shum, C. K. (2015). Discharge and water-depth estimates for ungauged rivers: Combining hydrologic, hydraulic, and inverse modeling with stage and water-area measurements from satellites. *Water Resources Research*, *51*(8), 6017–6035. https://doi.org/10.1002/2015WR016971

Mishra, V., Cherkauer, K. a., & Bowling, L. C. (2010). Parameterization of Lakes and Wetlands for Energy and Water Balance Studies in the Great Lakes Region*. *Journal of Hydrometeorology*, *11*(5), 1057–1082. https://doi.org/10.1175/2010JHM1207.1

Nigro, J., Slayback, D., Policelli, F., & Brakenridge, G. R. (2014). *NASA/DFO MODIS Near Real-Time (NRT) Global Flood Mapping Product Evaluation of Flood and Permanent Water Detection*. Retrieved from https://floodmap.modaps.eosdis.nasa.gov/documents/NASAGlobalNRTEvaluationSummary_v4.pdf

NWS. (1998). *Service assessment and hydraulic analysis Red River of the North 1997 floods*. book, Silver Spring, MD: U.S. Dept. of Commerce, National Oceanic and Atmospheric Administration, National Weather Service.

Policelli, F., Slayback, D., Brakenridge, B., Nigro, J., Hubbard, A., Zaitchik, B., Carroll, M., & Jung, H. (2017). The NASA Global Flood Mapping System. In V. Lakshmi (Ed.), *In Remote Sensing of Hydrological Extremes* (pp. 47–63). Stanford: Springer, Cham. https://doi.org/10.1007/978-3-319-43744-6_3

Rahman, M. M., Lin, Z., Jia, X., Steele, D. D., & DeSutter, T. M. (2014). Impact of subsurface drainage on streamflows in the Red River of the North basin. *Journal of Hydrology*, *511*, 474–483. https://doi.org/10.1016/j.jhydrol.2014.01.070

Shook, K. R., & Pomeroy, J. W. (2011). Memory effects of depressional storage in Northern Prairie hydrology. *Hydrological Processes*, *25*(25), 3890–3898. https://doi.org/10.1002/hyp.8381

Sun, D., Yu, Y., & Goldberg, M. D. (2011). Deriving Water Fraction and Flood Maps From MODIS Images Using a Decision Tree Approach. *IEEE Journal of Selected Topics in Applied Earth Observations and Remote Sensing*, *4*(4), 814–825. https://doi.org/10.1109/JSTARS.2011.2125778

Tuttle, S. E., Cho, E., Restrepo, P. J., Jia, X., Vuyovich, C. M., Cosh, M. H., & Jacobs, J. M. (2017). Remote Sensing of Drivers of Spring Snowmelt Flooding in the North Central U.S. In V. Lakshmi (Ed.), *Remote Sensing of Hydrological Extremes* (pp. 21–45). Springer, Cham. https://doi.org/10.1007/978-3-319-43744-6_2

U.S. Geological Survey. (2018). USGS's National Water Use Information Program, National Water Information System. Retrieved October 1, 2018, from https://waterdata.usgs.gov/nwis/

USACE. (2017). *Flood Risk Management and Hydrology Appendix A*.

Villarini, G., Smith, J. A., Baeck, M. L., & Krajewski, W. F. (2011). Examining Flood Frequency Distributions in the Midwest U.S. *Journal of the American Water Resources Association*, *47*(3), 447–463. https://doi.org/10.1111/j.1752-1688.2011.00540.x

Yang, G., Bowling, L. C., Cherkauer, K. A., & Pijanowski, B. C. (2011). The impact of urban development on hydrologic regime from catchment to basin scales. *Landscape and Urban Planning*, *103*(2), 237–247. https://doi.org/10.1016/j.landurbplan.2011.08.003

4. QUANTIFYING IMPACTS OF EXCESS WATER STRESS AT EARLY REPRODUCTIVE STAGES OF SOYBEAN FROM UNMANNED AERIAL SYSTEMS

Abstract

Low gradient agricultural areas prone to in-field flooding impact crop development and yield potential resulting in financial losses. Early identification of potential reduction in yield from excess water stress at the plot scale provides stakeholders with high-throughput information needed to assess risk and make responsive economic management decisions as well as future investments. The objective of this study is to analyze and evaluate the application of proximal remote sensing from unmanned aerial systems (UAS) to detect excess water stress in soybean and predict potential reduction in yield. A high-throughput data processing pipeline is developed to analyze multispectral images captured from a low-cost UAS throughout the growing season over two radiation use efficiency experiments in west-central Indiana, USA. Above-ground biomass is estimated remotely to assess the soybean development by considering soybean genotype classes (High Yielding, High Yielding under Drought, Diversity, all classes) and transferring estimated parameters to a replicate experiment. Digital terrain analysis using topographic wetness index (TWI) is used to objectively compare plots more susceptible to inundation with replicate plots less susceptible to inundation. The results of the study find: (1) Proximal remote sensing estimates above-ground biomass at the R4-R5 stage using adaptable and transferable methods with calculated percent bias (PBIAS) and root means square error (RMSE) of 0.8% and 72 g/m^2, respectively for all genetic classes. (2) Estimated biomass is sensitive to excess water stress with distinguishable differences identified between the R4-R6 development stages. (3) Low estimates of mapped percent of expected yield corresponded with observations of in-field flooding and high TWI. This study demonstrates transferable methods to estimate biomass at the plot level and increased potential to provide crop status assessments to stakeholders prior to harvest using low-cost UAS and a high-throughput data processing pipeline.

4.1 Introduction

Low gradient agricultural areas in the Midwest often experience extensive ponding of water in surface depressions thereby damaging crops and increasing financial risk from yield loss. In the Summer of 2015, crops were planted, but excess water from heavy precipitation caused destruction to five percent of the corn and soybean in Indiana resulting in approximately $300 million in crop damage (Pack, 2015). The Midwest was devasted in the Spring of 2019, where excessively wet conditions prevented crops from being planted or there was a complete loss of crops after planting. The saturated conditions caused by snowmelt and heavy rains in Nebraska and Iowa resulted in damages that exceeded $2 billion.

Inundated land area (ILA) is the extent of land surface covered by water following snowmelt, extensive rain events and saturated soil. ILA occurs after water has accumulated within local depressions which are typically less than one meter in depth (Figure 4.1). After accumulation in local depressions, the shallow water will expand through the field as shown in Figure 4.1a, resulting in different levels of impact during different development stages of soybean. In the vegetative stages, ILA can suppress the development of the soybean by preventing the development of nodes and leaves (Figure 4.1b). In the reproductive stages, ILA can reduce yield by restricting root growth, development of pods and filling of seeds, as well as contributing to lodging (Figure 4.1c).

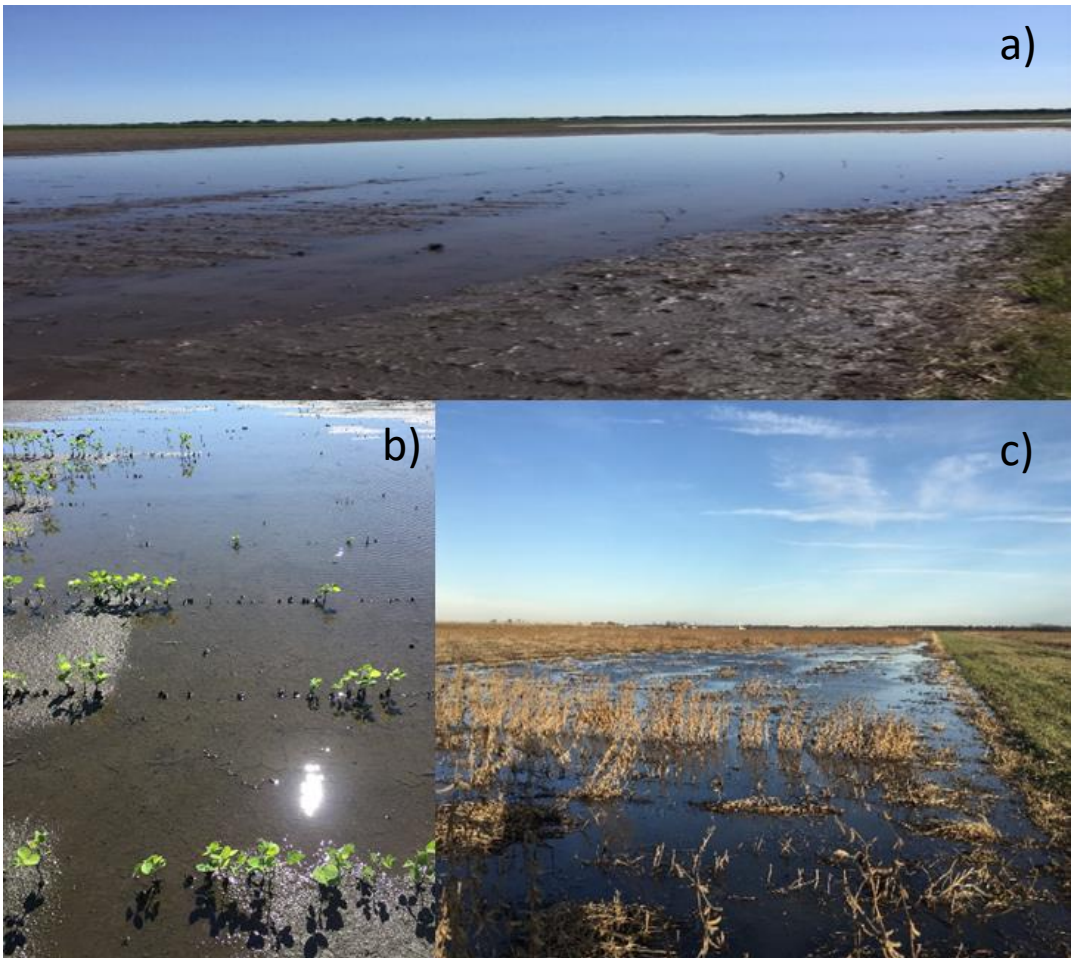

Figure 4.1. Image of inundated land area during different development stages of soybean in an agricultural field in west-central Indiana: a) extent and shallow depth of ILA after planting, b) vegetative stage where the impacts of ILA prevented some plants to develop leaves, and c) reproductive stage where the impacts of ILA have caused lodging in some plants.

Identifying and assessing crops impacted by ILA is important for agricultural stakeholders, because it provides quantitative information that can be used to evaluate effects and future risk needed for more responsive economic, management and insurance decisions. The effects of ILA on agricultural production may be decreases in crop yield or total loss in crop production in a section of a field. Crop status information from early development stages can be used to identify and quantify areas impacted by excess water stress, as well as offer predictive yield information. For instance, soybean can be vulnerable to ILA in the vegetative and reproductive stages of development (D. W. DeBoer and W. F. Ritter, 1970; Evans et al., 1999). Reproductive stages when the soybean is vulnerable are the pod and seed filling stages (R4 to the R6 stages), where the effects

of in-field flooding can have a large impact on soybean yield (Desmond et al., 1985; F. Gao et al., 2018; Ma et al., 2001b; Maimaitijiang et al., 2020). The R4 development stage occurs once the pods are full, approximately Mid-July. At the R5 stage seed filling begins. The R6 stage occurs once the seed has filled the pod, in August (Fehr et al., 1971). By identifying areas impacted by excess water stress early in the reproductive stages, stakeholders can assess risk and make more responsive economic and management decisions. The information gained can also be used to evaluate yield losses at the end of the growing season to support future investments in drainage infrastructure.

Conventional methods to measure the impacts of excess water stress include labor-intensive and site-specific field measurements. The impacts of water stress on crop development and yield have been evaluated using above-ground biomass (g, kg/m^2) and leaf area index (LAI) (m^2/m^2). Biomass and LAI have been used as variables in crop models to estimate yield by representing the variability in crop production (Lobell, 2013; Lobell et al., 2003; Monteith et al., 1977). Though these plot sampling techniques are commonly practiced, notable limitations are (1) the damaging process of collecting samples, (2) the time and expense of sample collection, and (3) the non-representativeness of samples of the total area conditions or crop types.

High spatial and temporal resolution data are needed to analyze crop development at the plot and field scale, because the adverse impacts of inundation also vary in scale and time. For instance, ILA may only impact a small number of rows within a portion of the field. High temporal resolution is needed to monitor and analyze change in environmental conditions that may affect yield (J. Liu et al., 2010; Maimaitijiang et al., 2020; Yu et al., 2016). In addition, the inundation may only last for a few days, and previous studies have shown that excess water stress can be detected in crops within two days (Griffin et al., 1988). As a result, information at high spatial and temporal resolution are needed to detect excess water stress within plots throughout the field. Remote sensing can be used to identify crop stress by measuring the reflected radiation. Band algorithms can be created and used by comparing parts of the spectrum which are related to the crops' attributes or related stress (Jones et al., 2010). Limitations of using remote sensing measurements to analyze crop development have been identified in both the spatial and temporal resolution of spaceborne satellites (Kross et al., 2015). Satellites with moderate spatial resolution

may not be able to differentiate between fields and crop types (Chen et al., 2005; Johnson, 2014). Prior research has also shown that course spatial resolution from satellites such as MODIS, using optical sensors have reduced sensitivity and underestimated measurements of above ground biomass (Chen et al., 2005; Yilmaz et al., 2008). In addition, high temporal resolution is needed to measure changes in the environment. However, freely available products from high spatial resolution platforms are limited by courser temporal resolutions. With the advent of unmanned aerial systems (UAS), field scale observations can be made daily if observation conditions permit. Proximal remote sensing is the indirect measurement of an object in close proximity with a sensor (Chipman et al., 2009). Proximal remote sensing from UAS platforms provides high spatial resolution at the centimeter scale and the ability to produce near real-time updates of the crop status in a non-destructive manner.

The Midwest is experiencing a changing climate with an increase in average annual precipitation and temperature, with the greatest increase in annual precipitation occurring in the critical spring months (Alberto et al., 2015; Widhalm et al., 2018). The United States Department of Agriculture (USDA) uses the term "prevented planted acres" to refer to an insured crop that could not be planted by a predetermined planting date because natural disaster such as flooding prevented the sowing. In 2019, the USDA reported a record number of prevented planted acres at 19.4 million acres where more than 73% of prevented planted acres were in 12 Midwest states. Further research is needed to quantify the impacts of excess water stress in early development stages at varying spatial resolutions. The aim of the study is to quantify the impact of excess water stress in the early reproductive stages of soybean based on proximal remote sensing from a UAS. The results of the study will help answer crop water stress questions such as: (1) Can proximal remote sensing be used to detect excess water stress in soybean? And (2) What is the potential yield impact from ILA? By identifying and assessing soybean yield loss due to excess water stress stakeholders can make more responsive economic and management decisions.

4.2 Methods

The following sections discuss the study site, data acquisition, developed tools and the approach used to measure crop stress.

4.2.1 Site description and data acquisition

The area of interest (AOI) for this study is a research farm field located in west-central Indiana (40.249° N, 86.877° W) which is approximately 7 ha (17 acres). The AOI is in a low gradient area with a soil texture that is predominantly silty clay loam. The dominant soil type being a Drummer soil. The poorly drained soil has subsurface tile drainage with a 20 m spacing at a depth of approximately 1 m. Figure 4.2 shows an aerial view of the site location along with two defined radiation use efficiency (RUE) experiments within the AOI. The RUE experiments were not designed to investigate excess water stress but due to weather events were adequate to support this study. Each RUE experiment contained three soybean classes defined as High Yielding (HD), Diversity (DA) or High Yielding under Drought (HYD) (Song et al., 2017). The number of plots for each class in RUE-1 were 191, 144 and 48 for HY, DA and HYD, respectively for a total of 383 plots for all genetic classes. The number of plots for each class in RUE-2 were 190, 139 and 48 for HY, DA and HYD, respectively with a total of 377 plots for all classes. Each of the three classes contained a unique recombinant inbred line (RIL) with a plot replicate in both experiments (RUE-1 and RUE-2). The plot replicates enabled a comparison analysis for changes in environment. A plot in a location which was more susceptible to inundation could be compared with its genetic replicate in a location that was less susceptible to inundation. Both experiments are approximately 1 ha (2. ac) and are managed using an annual corn and soybean rotation.

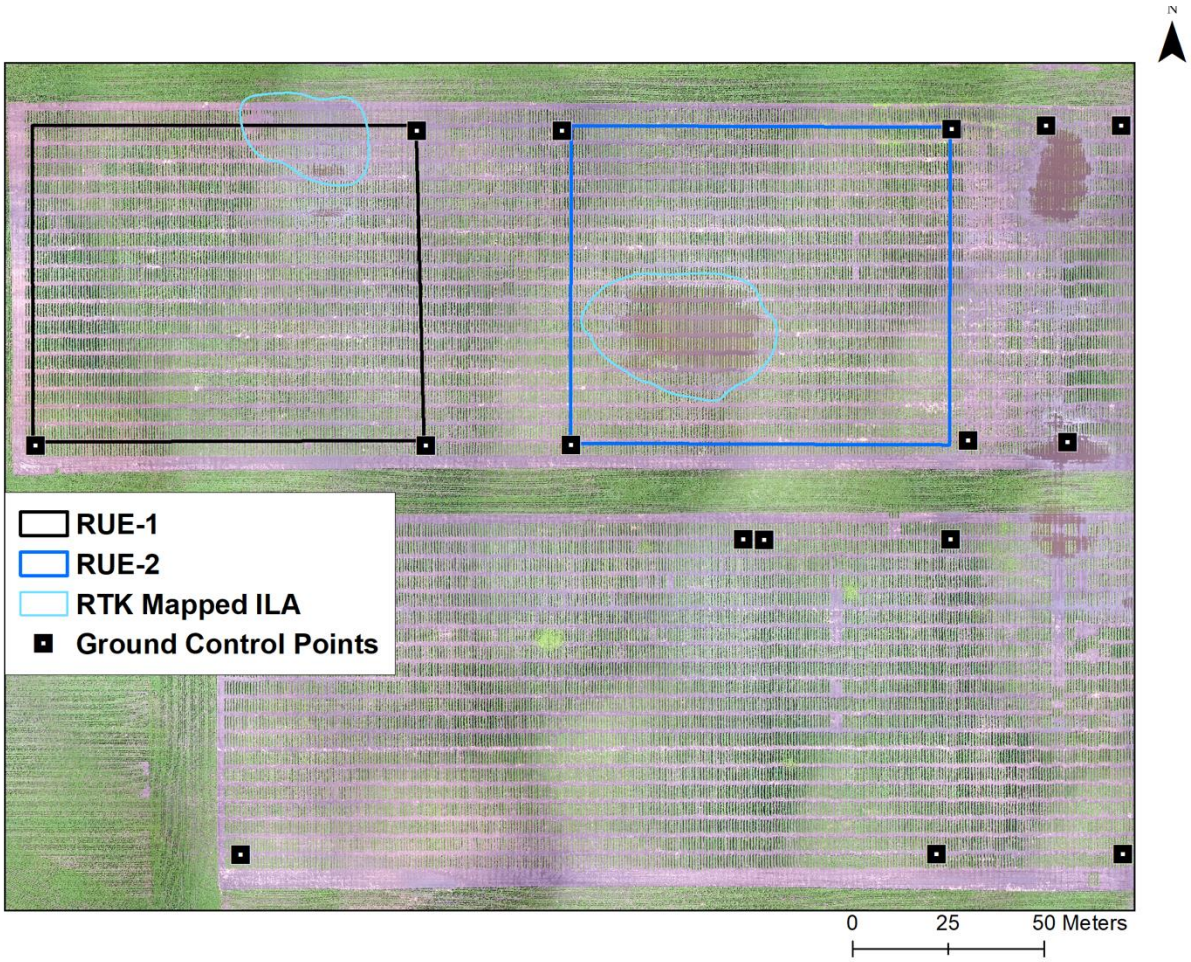

Figure 4.2: Map view of the field experiment, located in west-central IN. Two areas of interests were analyzed, which are outlined in black and blue. The black outline represents the area of experiment 1, RUE-1. The blue outline is the second experiment, RUE-2. The red outlines are mapped locations of inundation using an RTK. Ground control points were used to define extents of experiments.

In 2018, the field was planted with soybean and imaged using an Unmanned Aerial System (UAS) at least once a week from June to August with an RGB and multispectral camera. The UAS platform used in this study was an eBee from senseFly. This autonomous fixed wing system was used to acquire data over the AOI at an altitude of approximately 120 m at spatial resolution of approximately 2.54 cm/pixel and 6.00 cm/pixel for RGB and multispectral, respectively. The RGB camera used was a senseFly S.O.D.A. and the multispectral camera used was a Sequoia from Parrot. Flights were configured and flown with eMotion software. The forward and side overlap for flights were set to at least 85% and 70%, respectively. Ground control points (GCPs) were installed at the

corners of designed experiments and surveyed using the TOPCON Real Time Kinematic (RTK) surveying equipment (Figure 4.2).

Reflectance panels and field spectrometers were used to measure reflectance to aid in image calibration. The panels were laid out on the field during flight operations. The reflectance panels reflect at a specific and consistent percentage of light across the Visible and Near-Infrared spectrum. Five panels were used, with reflectances of 7%, 12%, 22%, 36% and 48%. Handheld field spectrometers were used as well to measure the reflectance of the panels as the multispectral data were being collected via the camera mounted to the UAS. The reflectance values from the panels, along with digital number values of the panels, extracted from the generated orthomosaics, were used to calibrate the remotely sensed data to surface reflectance using an empirical relationship between measured reflectance with respect to the digital number (G. M. Smith et al., 1999). The values generated from the empirical equation can be used as inputs into Vegetation Indices Derivation (VID) to calibrate the images for accurate reflectance and indices output. VID is a tool developed by our workgroup and used in our data processing pipeline that is further described in the following section (Lyu et al., 2019).

In addition, field measurements were collected to evaluate crop development as well as to map the extent of inundation. Soybean biomass samples were collected July 16th (60 days after planting) between the R4 and R5 stage. Above-ground biomass (g/m^2) was sampled throughout each experiment (RUE-1 and RUE-2) collecting 383 and 377 samples, respectively. After collection the soybean was oven dried and weighed. The dry weight was used in the analysis. The field was harvested with a combine, and yield measurements were collected from a yield monitor for each plot. The TOPCON RTK was used to map the extent of inundation following rain events by surveying the perimeter of inundation, as shown in Figure 4.2. Some observed ILA was not mapped in order to reduce the amount of foot traffic within the field.

4.2.2 UAS data processing pipeline

During a flight the UAS captures high resolution imagery from RGB and multispectral sensors over an AOI, and within the AOI may be many experiments and various crop status information that are of interest to plant breeders and stakeholders, where GCPs show the extent of multiple

experiments (Figure 4.2). For our study, in order to analyze and evaluate excess water stress of soybean at the field scale from high resolution imagery, flexible tools were needed to 1) map and extract soybean plots within a defined area, 2) perform atmospheric correction, and 3) apply vegetation indices and output the data to an interpretable format to make inferences. As a result, a high-throughput phenotyping processing pipeline was created with two developed tools, Crop Image Extraction, version 2 (CIE) and Vegetation Indices Derivation (VID). CIE and VID are Python programs which enable users to extract, calibrate and quantify vegetation indices of interest at the plot level (Lyu et al., 2019). The data processing pipeline is highly modular and efficient. Further detail about each tool is described below, and a GitHub repository is available to facilitate collaboration and enhance tool development.

CIE is the first step in the high-throughput phenotyping processing pipeline. CIE has the ability to extract plot images from designed experiments with RGB, multispectral and thermal imagery captured by the UAS. Plot images are extracted from user-configured inputs that describe the AOI and generated outputs from image stitching software such as camera parameter files. For our study Pix4D Mapper software was used (Pix4D SA, 2018). User-defined inputs consisted of experimental metadata such as location, number of crop rows, ranges, and units as well as length and spacing between plots. Figure 4.3 illustrates the components of a mapped experiment using CIE and outputted vegetation index with VID. A crop unit is defined as a single row of a soybean plot, so if the plot was described as a four-row plot it is expected to see four crop units within each plot. Crop rows and ranges are the number plots along the x-direction and y-direction, respectively. The crop unit centerline is used to measure distance between crop units in both x and y direction. After the configuration is completed for the AOI, plots are extracted by segmenting the canopy and gridding the calculated locations of each plot (Figure 4.3). As the crop develops and changes color, CIE uses multiple segmentations and crop localization functions to identify the crop unit centerline to ensure the correct number of crop units are identified within each crop plot (Lyu et al., 2019). The experimental metadata information along with the dimensions of the crop unit (crop length and spacing between crop rows) are then used to calculate the crop plot midpoint and map the remaining crop plots. The result is accurately and precisely identified crop plot midpoints that enable automated and rapid extraction of plot images. Depending on the size of the experiment, the generated CIE outputs can be thousands of plot images.

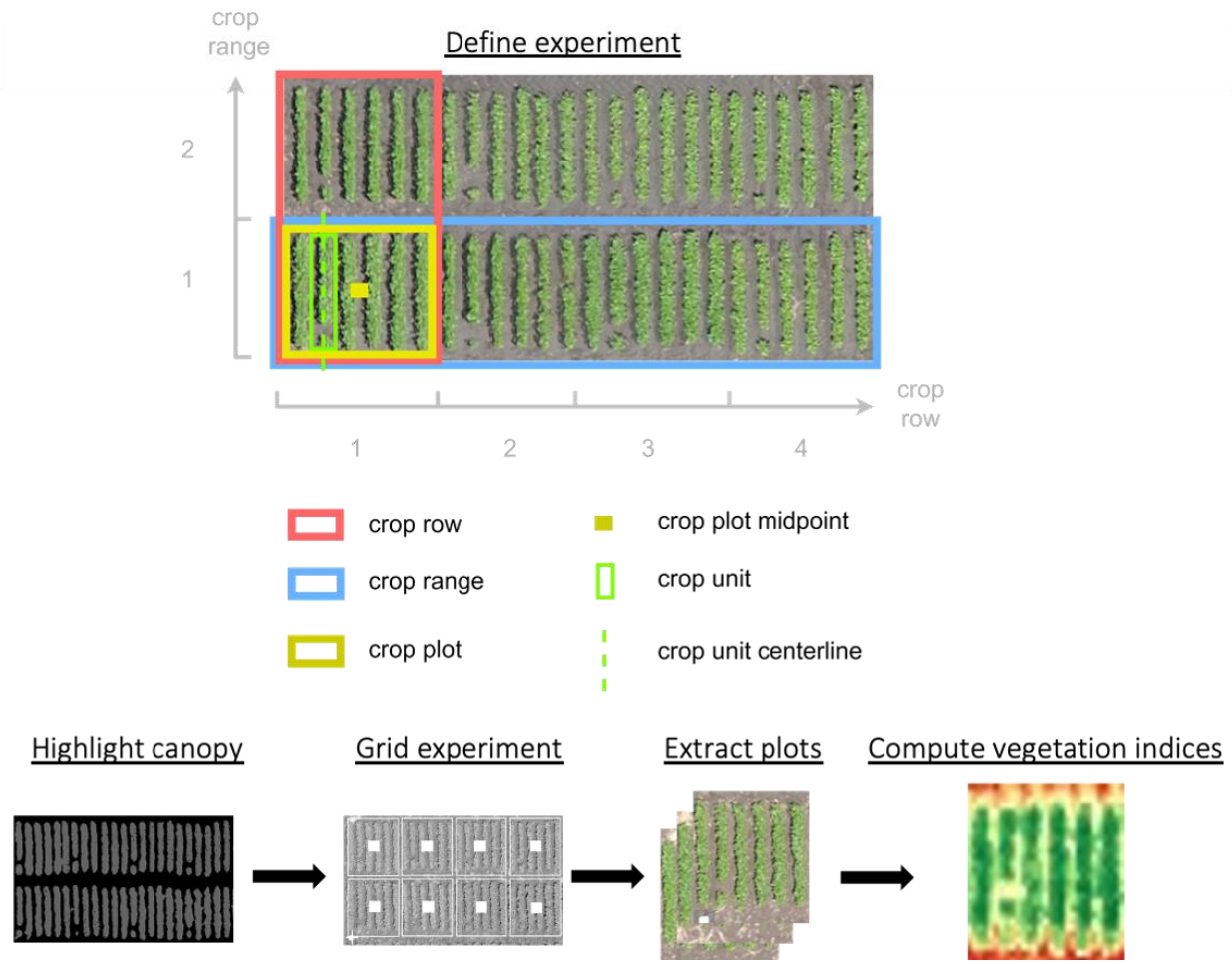

Figure 4.3: Illustration of components of a defined experiment from Crop Image Extraction and Vegetation Indices Derivation. The user has defined an experiment made of four crop rows and two crop ranges, and each crop plot contains six crop units. The experiment is made of four crop rows and two crop ranges. CIE extracts replicate plot images from the UAS during a flight over an area of interest. CIE enables the user to define an experiment, the tool then highlights the canopy, grids the experiment and extracts the replicate plot images from each gridded plot. VID is used to calibrate images and compute vegetation indices of interest.

The plot images from CIE were fed into VID, to calibrate images as well as create and use functions to calculate indices of interests. VID is the second step in the data processing pipeline. VID uses image attributes (i.e. row, range, date, image band, image replicate) with customized functions such as band algorithms to quantify phenotypic traits from the extracted plot images. VID can also calibrate plot images by applying empirical equations generated by extracting reflectance and digital number values from calibration panels positioned within the field during each flight (Smith

et al. 1999). The automated and efficient structure in VID allows for rapid processing and ability to output data into text and image format for analysis as shown in Figure 4.3.

4.2.3 Estimating above-ground biomass remotely

Identifying impacts of excess water stress on soybean remotely requires a predictive measurement that can assess the above-ground crop development. LAI (m^2/m^2) and above-ground biomass (g/m^2), as described previously, are common in-situ measurements that can also be used to assess crop development. Remotely-sensed observations of above-ground biomass often incorporate radiation use efficiency (RUE) models to estimate biomass by converting the absorbed photosynthetically active radiation (APAR) to biomass (J. Liu et al., 2010; Monteith, 1972; Monteith et al., 1977). Vegetation water content (VWC; kg/m^2), is a measurement of the total amount of water in the stems and leaves of vegetation, and VWC is commonly used as a parameter in algorithms to estimate soil moisture content (B. C. Gao et al., 1995; Kim et al., 2012; Yilmaz et al., 2008). VWC can be estimated with both active and passive sensors (Jackson et al., 1999). When measured with passive sensors, vegetation indices are used to obtain water content information. For example, equation 1 uses the normalized difference vegetation index (NDVI) and a stem water content variable to estimate the total above-ground water content (Chan et al., 2013; Jackson et al., 1999).

$$VWC = (1.9134 * NDVI^2 - 0.3215 * NDVI) + stem\ factor * \frac{NDVI_{max} - NDVI_{min}}{1 - NDVI_{min}} \quad (4.1)$$

Equation 1 consists of two terms which combined, estimate the total above-ground water content. The first term describes the foliage water and uses the NDVI values to relate the chlorophyll content within the foliage of the plant. The constants were calculated by optimizing a polynomial function to evaluate the relationship between NDVI and VWC (Jackson et al., 1999). The second term makes use of the stem factor (3.50 for crops) and NDVI annual extremes (maximum and minimum) to estimate the stem water content (Chan et al., 2013). The stem factor is a constant used to estimate the peak amount of water residing in the stems which is dependent on vegetation type. VWC is estimated using NDVI because a higher NDVI indicates a plant with increase in foliage that results in a higher VWC. Previous research used Landsat Thematic Mapper (TM)

images to estimate VWC at a spatial resolution of 30 m (Jackson et al., 1999). VWC has also been used to assess agricultural production for yield estimation and agricultural water management (Zhang et al., 2010).

Equation 1 was developed for regional and global scale retrievals of VWC using NDVI from spaceborne platforms such as MODIS and Landsat (Chan et al., 2013; Jackson et al., 1999). As a result, mission objectives required a spatial resolution at a large scale (30 m – 1 km) to measure NDVI, which would represent the foliage within the pixel. Multispectral imagery from a UAS is at a high spatial resolution (1 cm – 10 cm) where thousands of vegetation index values are generated at the plot scale as compared to satellite imagery which may only generate one vegetation index at the field scale. Understanding these differences in applications are needed to ensure band algorithms are being used and interpreted correctly. The high temporal and spatial resolution of the UAS enabled the use of a varying of NDVI extremes, NDVI maximum and minimum values were calculated for each soybean class and all classes for each experiment.

The estimation of VWC and associated terms in equation 1 were developed for parameterizing emission attenuation of vegetation in order to remotely estimate soil moisture content at a large scale (i.e., 1 km spatial resolution). For instance, the stem factor is a constant value for large scale application. In reality this value is not constant, and changes with the crop's growth and development as well as with environmental conditions. For this study an algorithm was needed for the plot scale which considered the environment that may change daily within the field, such as ILA and its impact on soybean development as well as variation in soybean genetics. In order to integrate these requirements for our application a varying stem water content variable and estimating parameters was developed for each soybean class.

As a result, an algorithm was developed for the plot scale that accounts for changes in the environment by measuring the impact those conditions may have on the soybean's estimated stem water content. In order to quantify the impacts of ILA on crop yield the stem water content would need to be calculated for each plot at different development stages over the growing season. Equation 2 shows the calculation of the adjustable stem factor.

$$adjustable\ stem\ factor = \frac{NIR_{ref}}{Green_{ref}} \tag{4.2}$$

Where NIR_{ref} is the average plot near-infrared band reflectance value and $Green_{ref}$ is the average plot green reflectance value. The stem water content was made variable to suit UAS applications by incorporating an adjustable stem factor and measurement of NDVI extremes that could be measured each flight. The band ratio of the NIR and green band is proposed to represent the stem factor for the following reasons. First the bands have a similar reflectance response when vegetation is healthy. The NIR band has a higher reflectance than the green band, which would correlate to the soybean as having an increase in above ground biomass. Second, the band ratios behave differently under different environmental conditions such as flooding. For instance, in the occurrence of ILA the green band will have an increase in reflectance caused by the turbid water behaving as a diffuse reflector to the smaller wavelength, whereas the NIR band will have a decrease in reflectance from absorption by water of the longer wavelength, which will represent an adverse effect on the crop status and decrease in above ground biomass. Incorporating the variable stem factor can help monitor and analyze change in the development of soybean throughout the growing season which is influenced by environmental conditions.

Providing transferable and representative models to estimate biomass are of necessity for plant breeders where a designed experiment may include multiple classes with thousands of different genetics under analysis at different locations. In this study, parameters were estimated using measured biomass (g/m^2) samples and remotely sensed observations of the average NDVI at the plot scale. Equation 3 shows the non-linear equation used to estimate biomass (g/m^2)

$$\begin{aligned} &Estimated\ Biomass\ (g/m^2) \\ &= (a * NDVI^2 + b * NDVI) + \psi * \frac{NDVI_{max} - NDVI_{min}}{1 - NDVI_{min}} + c \end{aligned} \tag{4.3}$$

where $a, b\ and\ c$ are output parameters from the SciPy optimization tool package used to estimate parameters using non-linear least squares. The adjustable stem factor, ψ, is calculated according to equation 2. Parameters were fit to the adjustable stem factor and with constant stem factor (3.50)

for comparison. The NDVI extremes, $NDVI_{max}$ and $NDVI_{min}$ were calculated for each class and all classes within each experiment.

As stated previously, each field experiment (RUE-1 and RUE-2) contained replicated plots from three classes (HY, HYD and DA) where biomass sampling was conducted in both field experiments in the early reproductive stages (R4-R5). In order to consider the variation in soybean genetics, equations were generated for HY, HYD, DA and all classes from data in RUE-1 using optimized estimated parameters from non-linear least squares. RUE-1 was selected because the measured biomass (g/m^2) had a larger range than RUE-2. The percent bias (PBIAS) and root mean square error (RMSE) were metrics used to evaluate the estimated biomass (g/m^2) with measured biomass (g/m^2) for each class and experiment. The evaluated metrics were also used to determine if parameters were representative for all classes of RUE-1, as well as assess the transferability of experiment parameters from RUE-1 across all genetic lines in RUE-2.

4.2.4 Identifying areas of water accumulation using topographic wetness index

Digital terrain analysis is an effective method used in hydrology applications to explore potential variation in water flow and accumulation based on topographic information. Topographic indices reflect the ratio of contributing area to surface slope and so have been used to predict areas of water accumulation (Grimm et al., 2018; Quinn et al., 1995). The Topographic wetness index (TWI) is a function of the natural log of the contributing drainage area per contour length, α over the surface slope tan β, as listed in equation 4 (Beven et al., 1979).

$$TWI = \ln\left(\frac{\alpha}{\tan\beta}\right) \tag{4.4}$$

The TWI is calculated from a digital elevation model (DEM). The DEM pixels are used to measure α and tan β. The TWI is used to identify hydrologically similar areas, and in our study to identify areas susceptible to ILA, with TWI calculated from a high-resolution DEM (1.5 m). (Figure 4.4). In the AOI, TWI values range from 2 to 23, where regions of lower values are less susceptible to in-field flooding. As TWI values increase, the susceptibility to soil saturation and in-field flooding increases. The observed extent of inundation measured with the RTK as compared to the TWI is

also shown in Figure 4.4 with an average TWI of 13.5 in the surveyed region. TWI was incorporated into the plot scale analysis by using CIE outputs to extract TWI values for each plot within the defined experiments. Plots extracted with CIE in experiments RUE-1 and RUE-2 are shown as black circles in Figure 4.4.

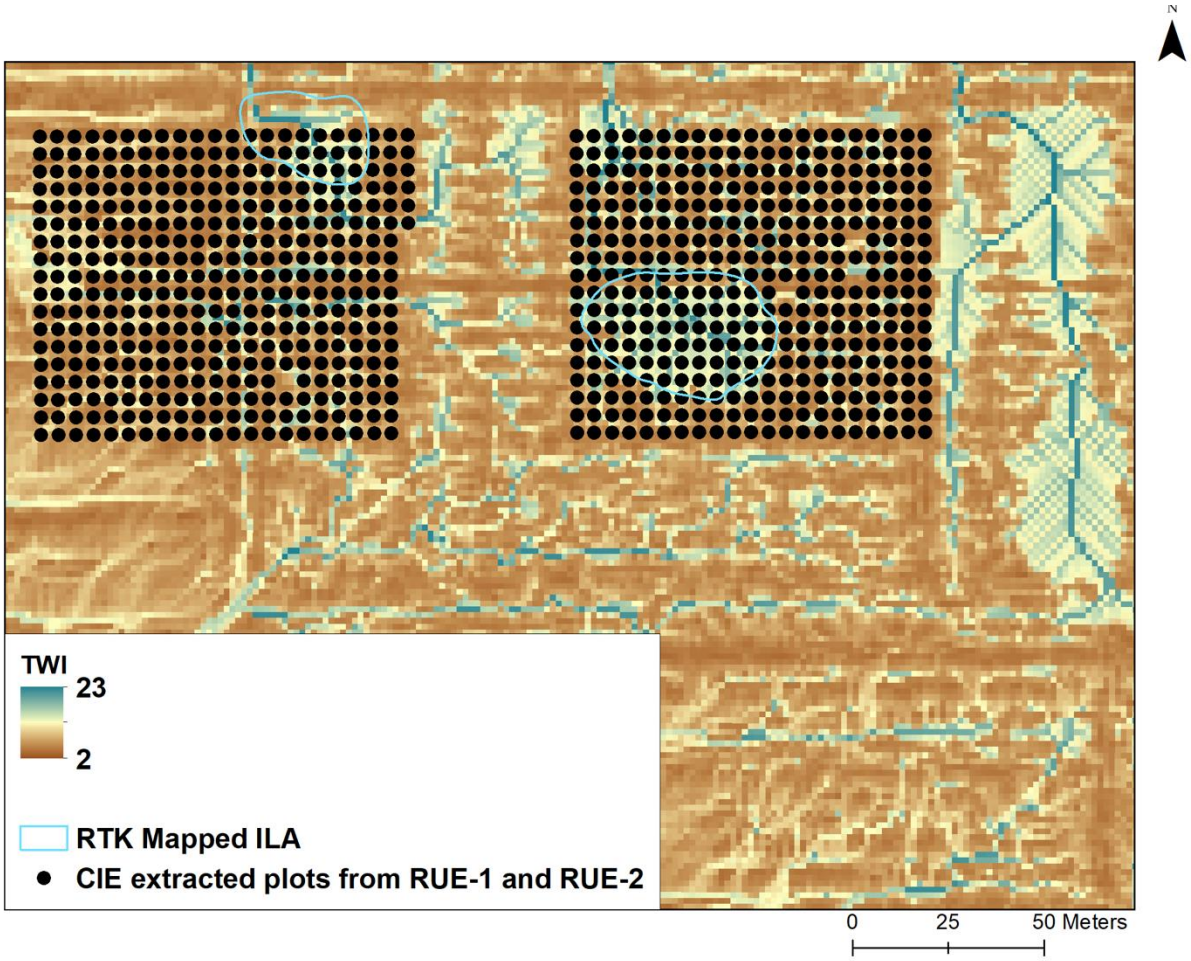

Figure 4.4: Map of topographic wetness index (TWI) calculated from a 1.5 m resolution DEM at the study location. Lower values shown in brown are less suspectable to in-field flooding. The transition from brown to blue shows an increase in susceptibility of in-field flooding. Mapped inundated land area (ILA) shows agreement with the calculated TWI. Crop Image Extraction (CIE) can be used to extract TWI from plots within a defined experiment. The black circles represent the extracted plots from RUE-1 and RUE-2.

In this study TWI was used to analyze the variation in soybean yield between replicates to explore the potential impact of excess water stress. To analyze the differences, TWI thresholds were applied to identify plots less likely to experience ILA and those that were more likely to experience ILA. Thresholds were determined using spatial analyst in ArcMap 10.5 to calculate average TWI

in regions observed to experience inundation, and those observed to be consistently dry. The low TWI threshold (drier conditions) was set to values less than 7.4 and the high TWI threshold (wetter conditions) was set to values greater than 13.5. Figure 4.5 shows a scatter plot comparing soybean yield for all plots under analysis, labeled by class and the plot's associated TWI value. The red vertical lines indicate the location of the applied thresholds for low and high TWI values at 7.4 and 13.5, respectively. The figure shows that plots with a low TWI value have large range in yield from approximately 2,000 kg/ha to 5,700 kg/ha with a median value of 3,970 kg/ha. Whereas plots with a high TWI value have less variation in yield ranging from approximately 2,500 kg/ha to 4,800 kg ha and a lower median yield of 3,770 kg/ha. Plots located in areas of high TWI were predominantly of the HY and DA classes, while only three plots of the HYD were located in an area of high TWI.

In order to isolate the potential impact of differing wetness conditions, 28 replicate pairs were extracted from the RUE-1 and RUE-2 experiments, in which one plot experienced low TWI (< 7.4) and the other experienced high TWI (>13.5). This filtering process allows analysis to focus on replicates that have the potential for different wetness conditions. The replicate plots create opportunities to analyze and compare the soybean development and impact of excess water stress between replicate plots with similar traits. In addition, planting of plots did not take into account TWI, which means all plots were equally likely to be planted in areas that may or may not experience excess water stress.

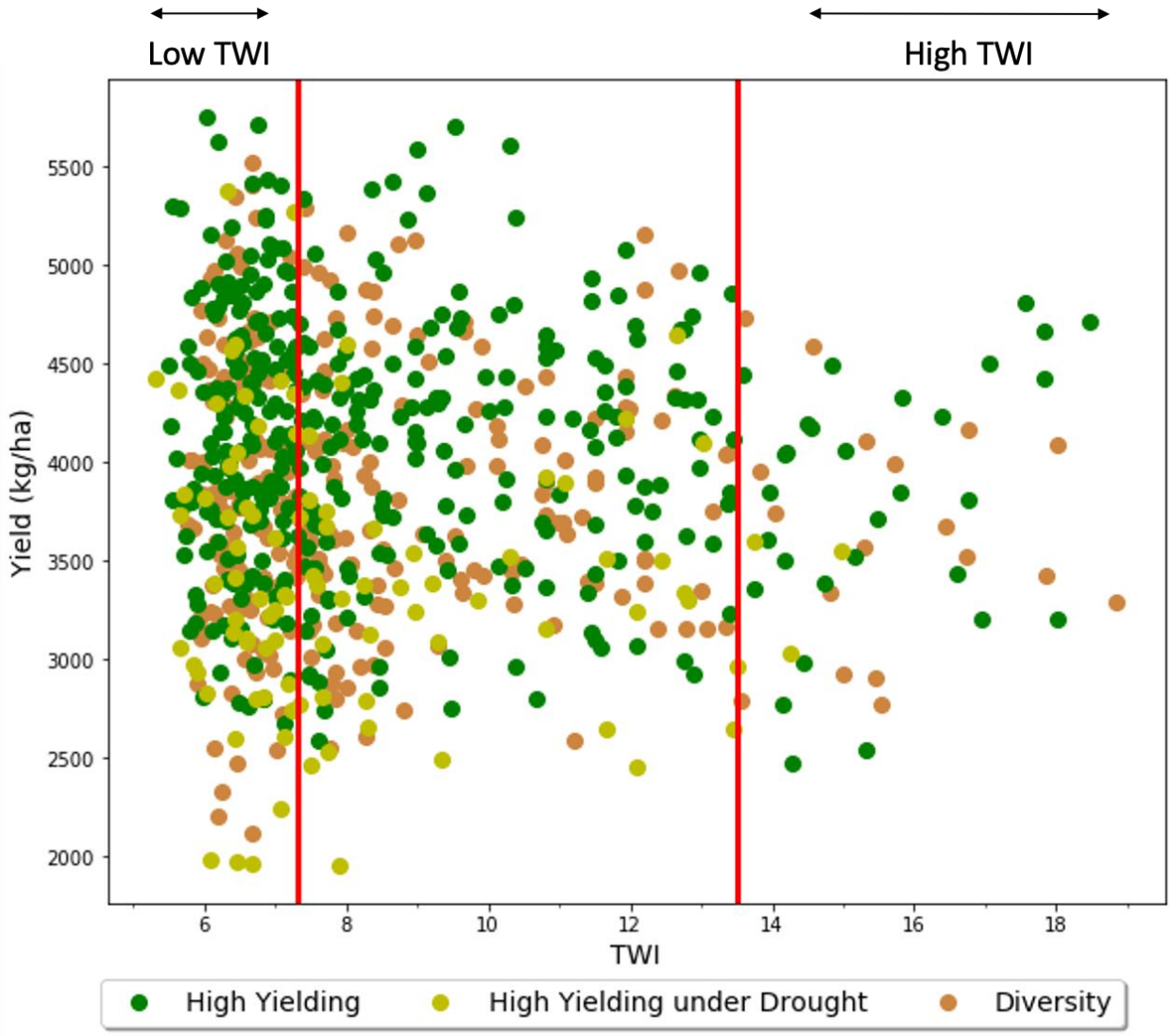

Figure 4.5. Scatter plot of the relationship between topographic wetness index (TWI) and soybean yield (kg/ha) labeled by class. TWI thresholds at 7.4 and 13.5 were set to compare RUE-1 and RUE-2 replicates less likely to experience ILA to those that were more likely to experience ILA. The low and high TWI ranges used in analysis are represented by arrows.

4.3 Results

4.3.1 Above-ground biomass prediction

Results of the optimization process for each class and expanding all genetic lines are listed in Table 1 which includes the parameter estimates (a, b and c), percent bias (PBIAS) and root mean square error (RMSE). The estimated parameters used to estimate biomass for each class and all classes were similar, with the HYD having the most contrast from accompanying classes listed in Table 4.1, highlighting the subtle differences in estimated parameters for different genetics. HYD has the lowest PBIAS and RMSE amongst all classes at < 0.1% and 64 g/m^2, respectively. The constant stem factor (3.50) was also evaluated versus the adjustable stem factor. Overall the constant stem factor results are very similar to the adjustable stem factor with a PBIAS and RMSE ranging from -0.5% to -0.6% and 63 g/m^2 to 75 g/m^2, respectively. Figure 4.6 compares estimated biomass (g/m^2) with respect to measured biomass (g/m^2) for classes HY, HYD, DA and all classes from RUE-1. The red line is a 1:1 reference for each comparison to show overestimation or underestimation of estimated biomass with measured biomass. For each class and all classes in RUE-1, RMSE and PBIAS ranged from 64 g/m^2 to 73 g/m^2 and <0.1% to 0.8%, respectively. The low PBIAS and RMSE for all classes in RUE-1 confirmed that the parameters were representative for all classes under analysis, and it is not necessary to develop equations for each class separately. Figure 4.6a and 6d compare the estimated biomass and measured biomass for the HY class and all classes. The equation for all classes was able to accurately represent the range of estimated biomass similar to the dominant class that had 191 plots.

Table 4.1: Estimated parameters for High Yielding (HY), High Yielding under Drought (HYD), Diversity (DA) and all classes for RUE-1 and RUE-2 with calculated percent bias (PIBAS) and root mean square error (RMSE). Parameters from RUE-1 were transferred to RUE-2. The constant stem factor was also analyzed to compare with the adjustable stem factor.

Type and number of plots	Parameter *a*	Parameter *b*	Parameter *c*	PBIAS (%)	RMSE (g/m^2)
		RUE-1			
HY 191 plots	1817.06	-1022.2	226.9	0.8	73
HYD 48 plots	2382.77	-1863.25	497.97	< 0.1	64
DA 144 plots	1993.46	-1267.85	308.15	<0.1	70
All classes 383 plots	1955.75	-1217.37	290.23	0.8	72
HY – constant stem factor 191 plots	464.06	761.75	-372.22	-0.6	75
HYD – constant stem factor 48 plots	2379.15	-1856.73	493	-0.5	63
DA – constant stem factor 144 plots	1993.16	-1264.52	305	-0.5	70
All classes – constant stem factor 383 plots	1955.75	-1217.37	286.73	-0.5	71
		RUE-2			
HY 190 plots	1817.06	-1022.2	226.9	16.6	82
HYD 48 plots	2382.77	-1863.25	497.97	10.2	65
DA 139 plots	1993.46	-1267.85	308.15	11.5	72
All classes 377 plots	1955.75	-1217.37	290.23	14.4	77

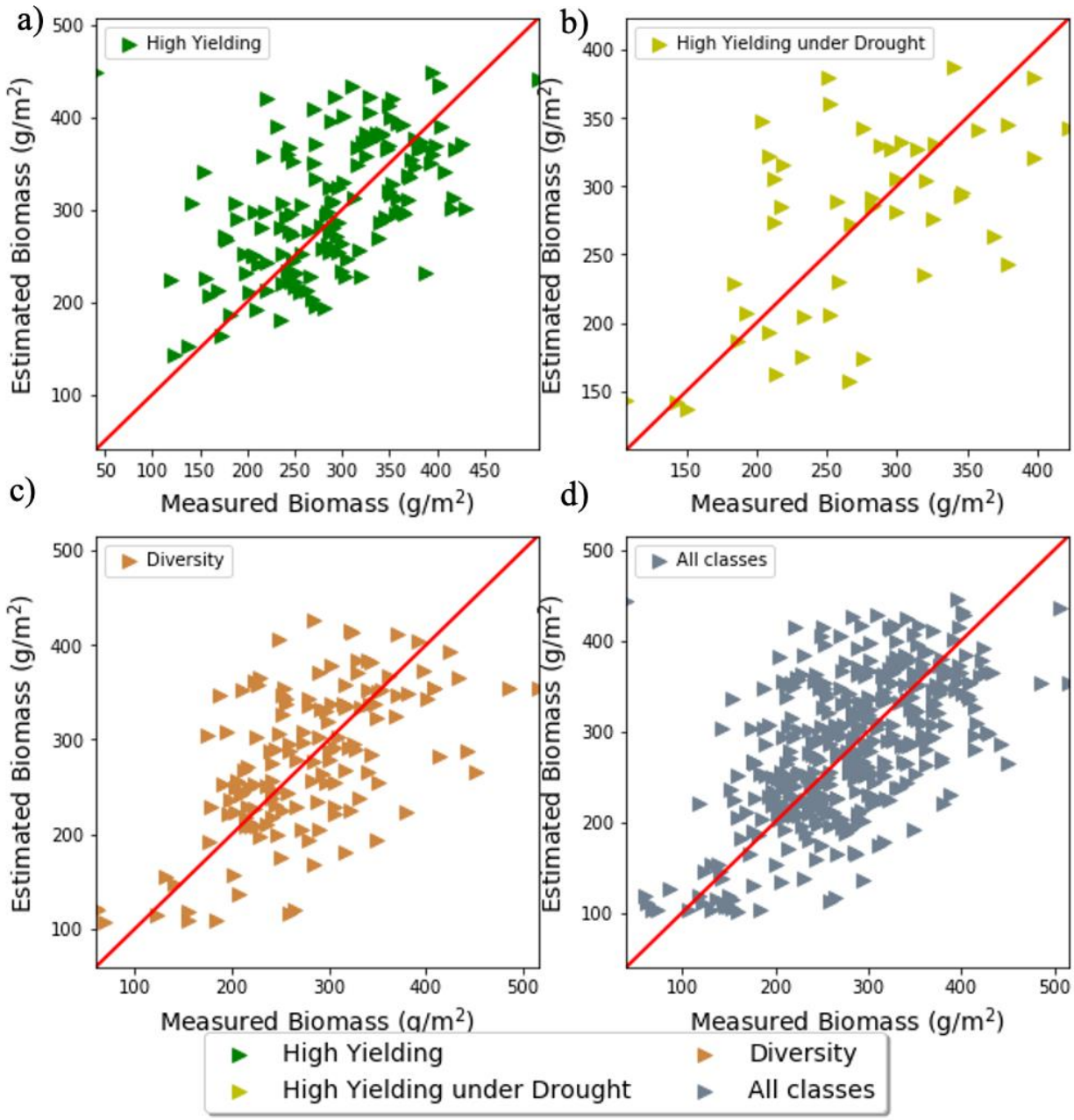

Figure 4.6: Scatter plots comparing estimated biomass with measured biomass for each class and all classes in RUE-1 shown as triangles. a) High Yielding, b) High Yielding under Drought, c) Diversity and d) all classes. Parameters were estimated for each class to consider varying soybean genetics and for all classes to determine if one set of parameters could be representative for all classes.

The parameters for each class and for all classes developed from RUE-1 were transferred to RUE-2. Table 1also lists the PBIAS and RMSE for RUE-2, which ranges from 10.2% to 16.6% and 65 g/m^2 to 82 g/m^2, respectively. Figure 4.7 shows subplots comparing estimated biomass (g/m^2) with respect to measured biomass (g/m^2) for classes HY, HYD, DA and all classes from RUE-2. Overall, the transferred parameters were sufficient at representing the range of estimated biomass for varying genetic classes as well as all classes as shown in Figure 4.7. The transferred equation shows slight overestimation of estimated biomass for HY, DA and all classes for RUE-2 displayed in Figure 4.7a, Figure 4.7c and Figure 4.7d, respectively. The calculated PBIAS is satisfactory with all types under analysis below 20% and RMSE comparable to values calculated in RUE-1. The transferred equation shows the ability to accurately estimate biomass for varying number of plots, such as in the HYD (contains 48 plots) and all classes (contains 377 plots in RUE-2) where the PBIAS is 10.2% and 14.4%, respectively.

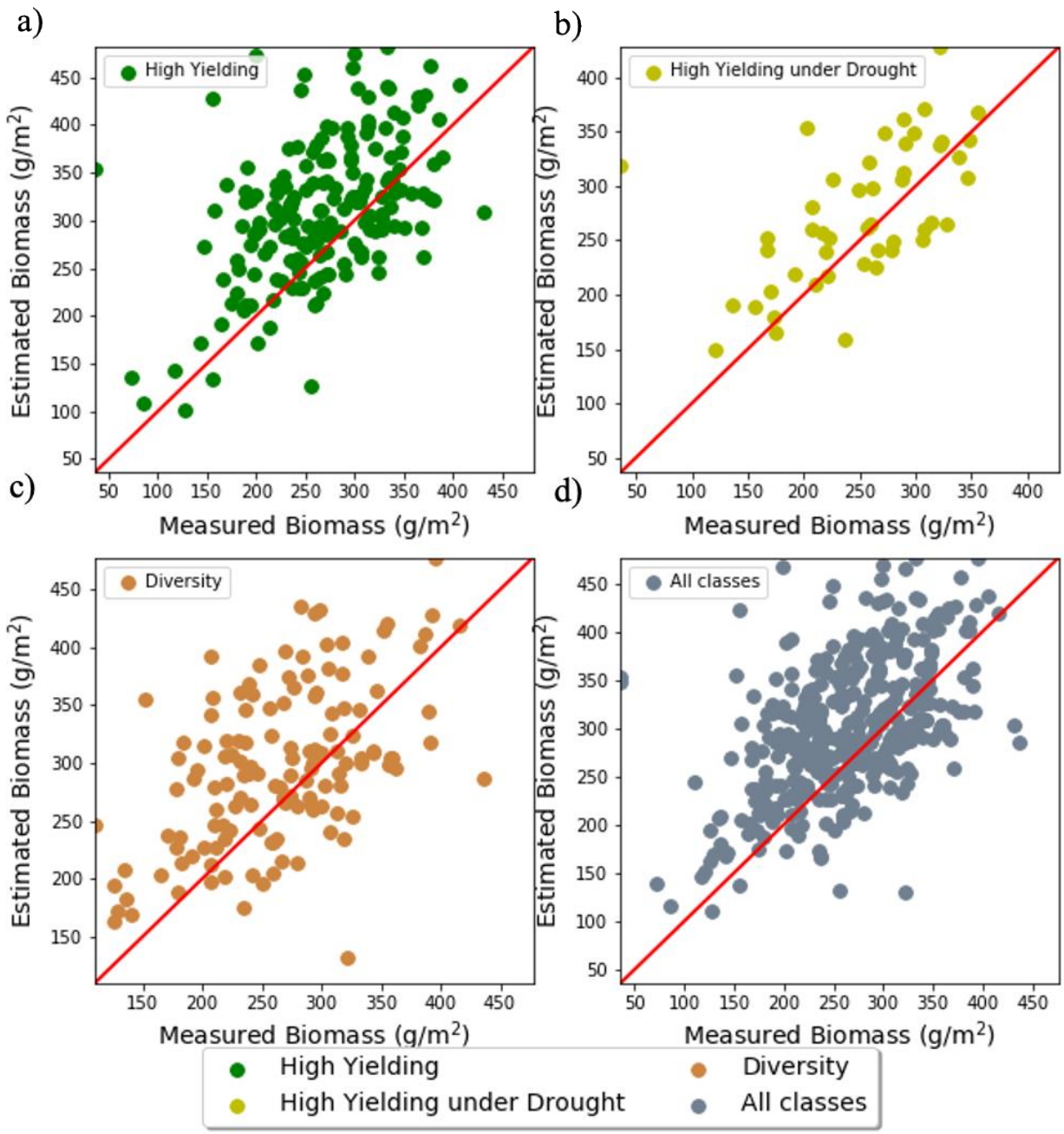

Figure 4.7: Scatter plots comparing estimated biomass with measured biomass for each class and classes in RUE-2 shown as circles. a) High Yielding, b) High Yielding under Drought, c) Diversity and d) all classes. Parameters were transferred from RUE-1 to RUE-2.

Using the representative equation for all classes, above-ground biomass was estimated to analyze the soybean development and impacts of excess water stress. Figure 4.8 is a spatial map displaying the estimated biomass from a flight date on July 17th, 2018. In Figure 4.8, the estimated biomass

ranges from 102.15 g/m² to 476.45 g/m². In RUE-2, the cluster of low biomass values indicated by the red circles correspond with the high TWI values and mapped ILA using the RTK. Also, the northeast corner of RUE-1 has low estimated biomass. This section of the field experienced ILA between the R1-R2 stage of the growing season and corresponds to high TWI values and observed ILA.

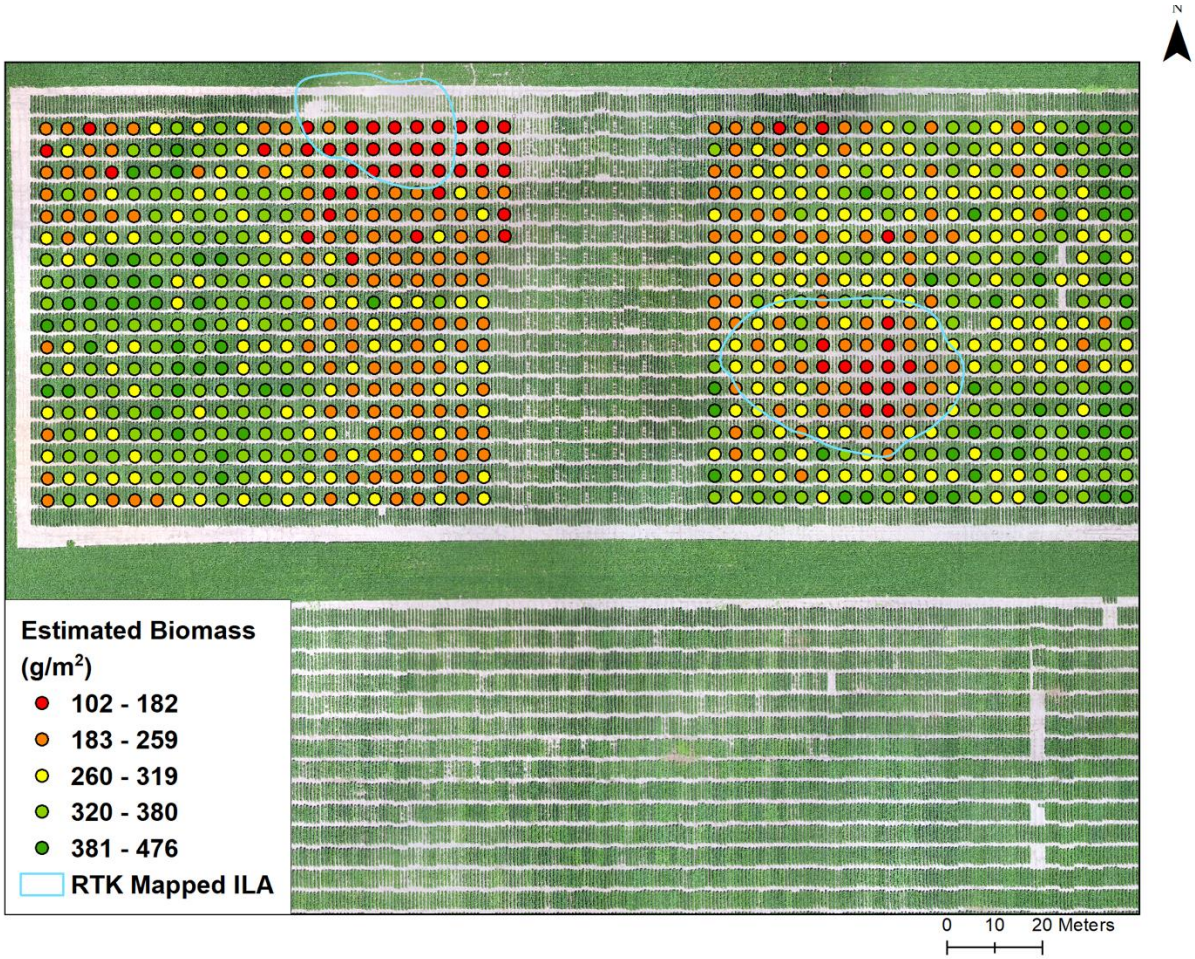

Figure 4.8: Estimated biomass (g/m²) spatially from early reproductive stages (R4-R5) of soybean for experiments in RUE-1 and RUE-2. Outputs generated using CIE and VID. Plots of low estimated biomass values are shown in red and the transition to green represent an increase in estimated biomass. Plots with low estimated biomass correspond with mapped inundated land area.

4.3.2 Sensitivity of above-ground biomass to water stress

To explore if the estimated above-ground biomass is sensitive to water stress, plots with observed occurrences of ILA in RUE-2 were compared with their replicate in RUE-1. In 2018, ILA was

observed on June 25th, July 6th and July 12th. The ILA observed on June 25th was from a large rainfall event (32 mm) on June 23rd demonstrating that ILA can persist for at least two days even with subsurface tile drains. Excessive saturated conditions were observed on July 2nd from heavy rainfall five days prior. In addition, heavy cumulative precipitation of 29 mm occurred during critical periods of the reproductive stages (R4-R6). The R1-R6 stages occurred approximately between June and August. The R1-R3 stages occurred between June 25th to July 12th. The R3-R4 stage was from July 12th to July 17th. The R4-R6 stages occurred between July 17th to August 2nd. The R7-R8 stages occurred between August 9th and August 14th.

Figure 4.9 shows four examples comparing plots in RUE-1 with replicate plots in RUE-2 and analyzing the impacts of excess water stress on estimated biomass over the growing season for the two most dominant class types, DA and HY. Figure 4.9a and 9b display the DA class while Figure 4.9c and 9d assess the impacts of excess water stress on estimated biomass for the HY class. Figure 4.9a and 9b, display similar behaviors from the impacts of excess water stress on biomass in RUE-2 resulting in a 4% and 18% decrease in yield, respectively. Plots in RUE-2 experienced ILA early in the growing season, whereas replicate plots in RUE-1 did not experience ILA. Comparing plots impacted by ILA in RUE-2 with the replicates not impacted by ILA in RUE-1, noticeably lower estimated biomass is detected at the R4-R5 stage on July 17th. Biomass increased at a lower rate for plots in RUE-2 between R4-R6 coinciding with heavy precipitation resulting in a lower estimated biomass at the end of the growing season.

Figure 4.9c highlights an interesting example where both replicate plots experienced inundation at the R1-R2 stage. ILA was observed at the northeast corner of RUE-1 and central section of RUE-2. Between the R1-R4 stages there is little difference between estimated biomass values for the plots in RUE-1 and RUE-2. As the growing season continued the plot in RUE-1 had less occurrences of inundation and an increase in biomass as compared to the plot in RUE-2 which had more occurrences of inundation and a decrease in biomass. The difference in biomass at the end of the growing season was 106 g/m^2 and there is a 16% decrease in yield for the plot in RUE-2. Figure 4.9d illustrates pronounced differences in estimated biomass between plots early in the growing season at the R3-R4 stage with an end of season difference of 119 g/m^2. The plot

impacted by excess water stress in RUE-2 has a 16% decrease in yield as compared to the replicate plot not impacted by excess water stress in RUE-1.

This analysis was completed using plots where ILA had been mapped. The comparison of replicate plots revealed noticeable differences from the impacts of excess water stress on estimated biomass at the early reproductive stages (R4-R6) of soybean and may provide useful indicators of impacts to final yield. An objective approach is needed to distinguish between plots that are more susceptible to ILA with plots that are less susceptible to ILA and recognizing that soybeans can be impacted by excess soil moisture conditions even before surface ponding is visible. The TWI can be used to distinguish plots using TWI thresholds with the estimated biomass.

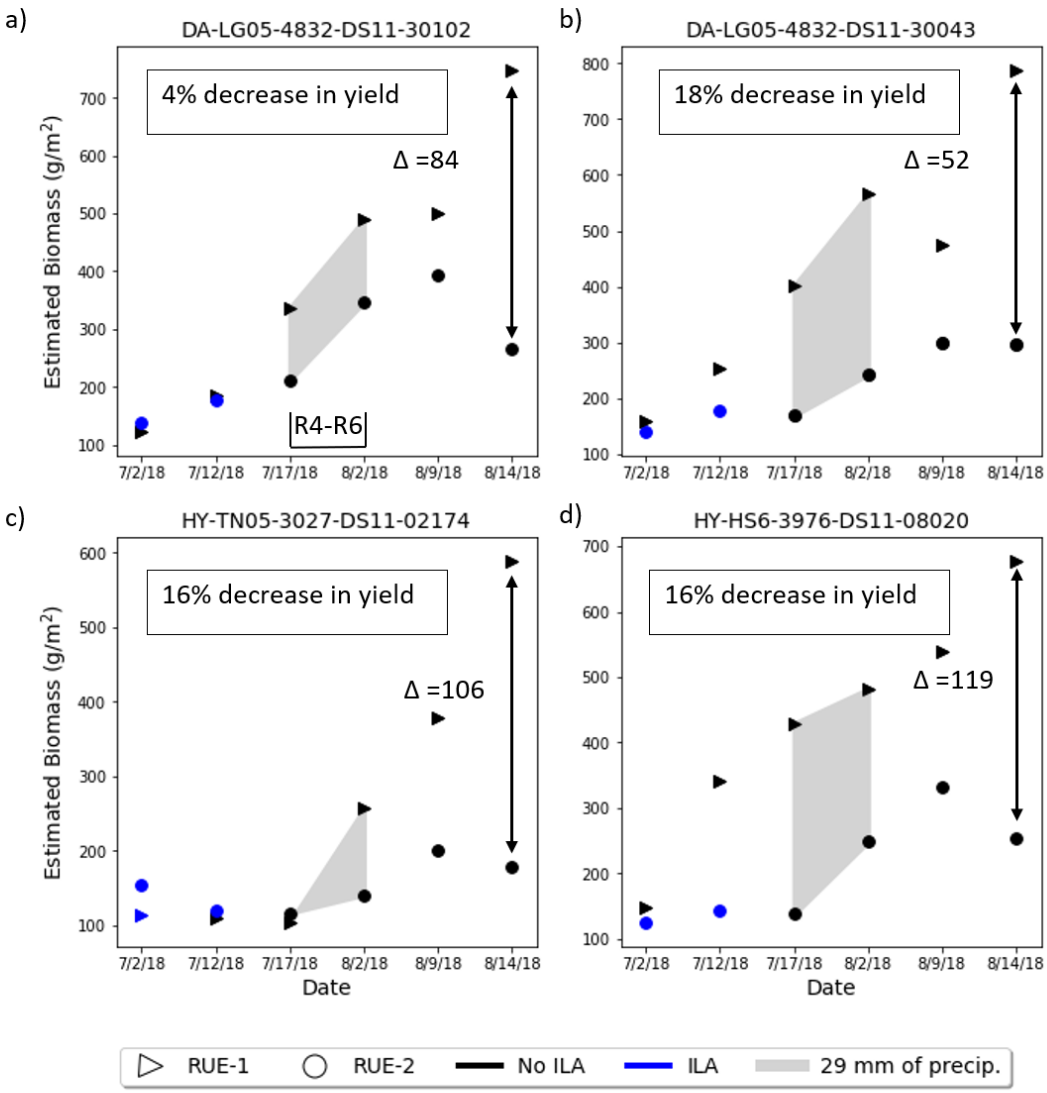

Figure 4.9: Four examples analyzing the impacts of excess water stress on estimated biomass (g/m^2) over the growing season. Plots experienced inundated land area (shown in blue) and heavy cumulative precipitation (shaded in grey). Analysis was done by comparing plots where ILA was observed in RUE-2 (circles) with the plot replicate in RUE-2 (triangles). a) Plots in the Diversity (DA) class recombinant inbred line DS11-30102. b) Plots in the Diversity (DA) class RIL DS11-30043. c) Plots in the HY class RIL DS11-02174. d) Plots in the HY class RIL DS11-08020.

4.3.3 Quantifying the impacts of excess water stress on yield

To quantify the impact of excess water stress on yield, replicate plots in areas of high TWI were analyzed and compared with plots in low TWI (Δ TWI) using estimated biomass from the equation representing all classes in RUE-1 and RUE-2. TWI thresholds of 7.4 and 13.5 were used for low and high areas of TWI, respectively. A total of 28 replicate plots were identified that were located in areas of high susceptibly to excess water stress with a reference replicate in an area less susceptible to excess water stress.

The relationship between Δ TWI, yield loss (Δyield) and difference in estimated biomass (Δ estimated biomass) at early reproductive stages (R4-R5) was analyzed (Figure 4.10). Change was measured by taking the difference between replicate plots in areas of high TWI minus low TWI. Difference in yield range from approximately -2400 kg/ha to 1300 kg/ha, with a negative yield difference indicting a decrease in yield associated with the plot more susceptible to excess water stress. Figure 4.10 shows that as the change in estimated biomass increases (becomes more negative), the yield loss also increases (difference in yield becomes more negative), with biomass differences that exceed 100 g/m^2. Figure 4.10 highlights the relatively high variability of Δ TWI as an independent metric to estimate change in yield.

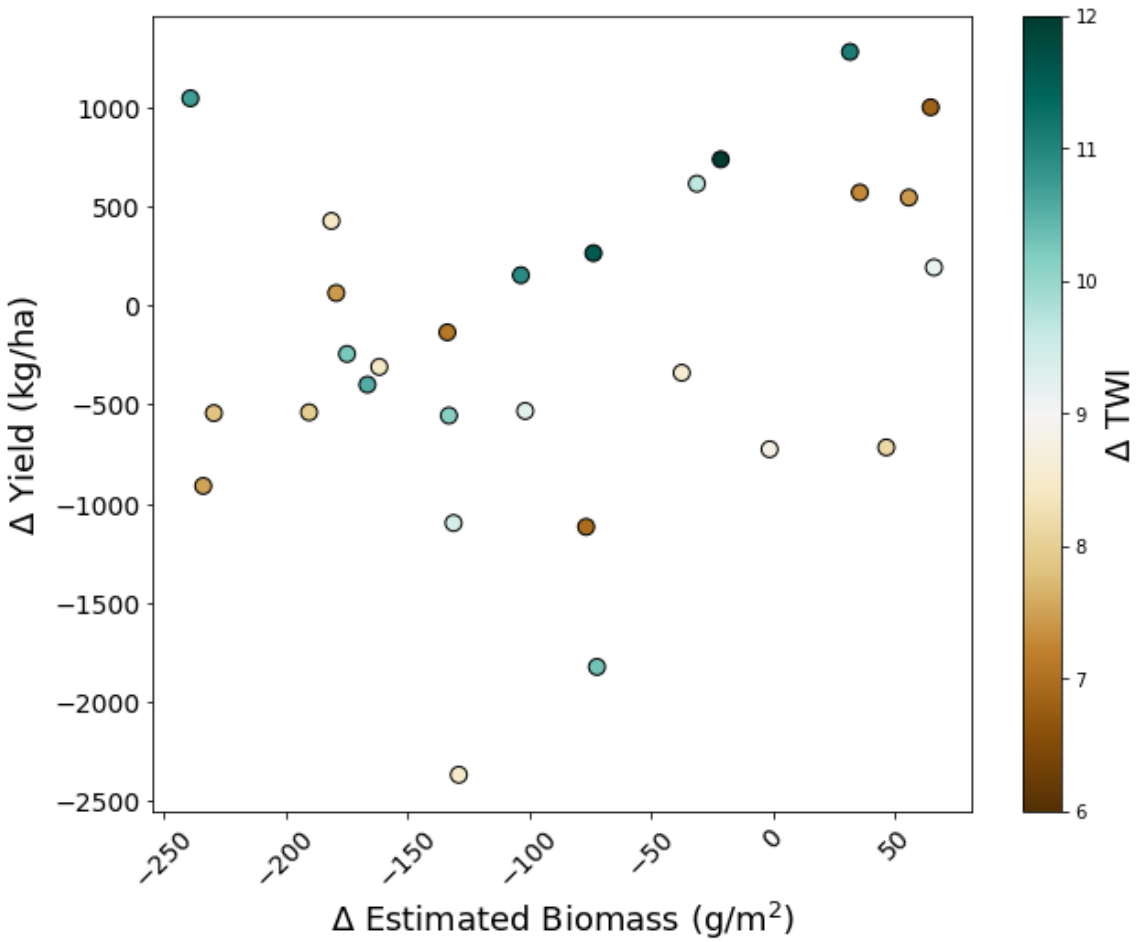

Figure 4.10: Analyzing the interactions between Δ yield, Δ estimated biomass and Δ TWI at the early reproductive stage (R4-R5). Values are colored with the difference in TWI between replicate plots, which range from 7 to 12.

The percent of expected yield (%) with respect to the relative biomass (fraction) was also analyzed to create a predictive equation for stakeholders to determine percent of expected yield based on observations from the early reproductive stages (R4-R5). The percent of expected yield is the calculated ratio of the change in yield between plots of high and low TWI with respect to the yield in low TWI. The relative biomass is the calculated ratio of the biomass in plots of high TWI (g/m^2) with respect to the biomass (g/m^2) in plots of low TWI. Figure 4.11 demonstrates the relationship between the percent of expected yield and fractional biomass at R4-R5 for plots in areas of high TWI. The range of percent difference is from 52% to 151%, while the range of estimated biomass is 0.41 to 1.25. Figure 4.11 demonstrates the linear model which shows a positive linear correlation. The correlation across all plots is not significant with a correlation coefficient (r) of 0.32. The F-

statistic of the regression is not significant at 0.05 but is significant at 0.1. In general, as estimated biomass increased Δ estimated biomass also increased, which transitioned to a positive increase in percent difference in yield.

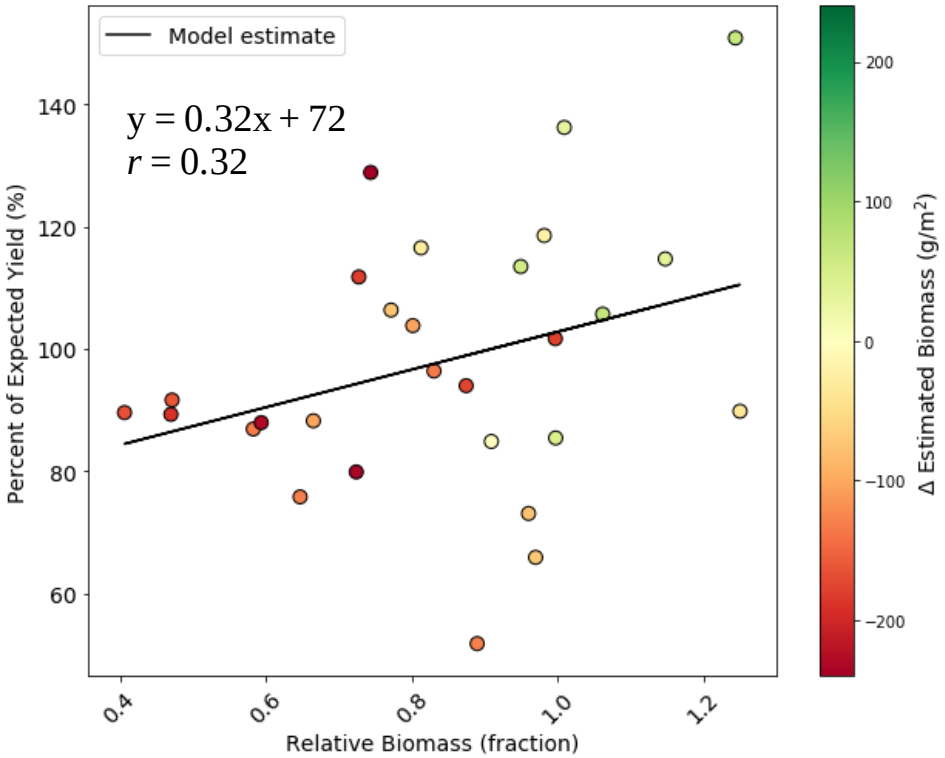

Figure 4.11. Comparing interactions between percent of expected yield (%) with respect to relative biomass (fraction) and the Δ estimated biomass (g/m^2) at the early reproductive stage (R4-R5). The model estimate is shown in black.

Figure 4.12 is a spatial map of the percent of expected yield (%) across RUE-1 and RUE-2 from a flight on July 17th, 2018 at the R4-R5 stage. The range of percent of expected yield is from 83 to 125%. The average percent of expected yield is 103%. The lowest range of percent of expected yield between 83% and 90% occur predominately in corresponding areas susceptible to inundation. For RUE-1 plots with the lowest percent of expected yield occur in the northeast corner which correspond to the high TWI and mapped ILA. In RUE-2 plots with the lowest percent of expected yield occur towards the center of the field and also correspond with high TWI and mapped ILA. In RUE-1 the percent of expected yield generally increases in the direction from east to west. In RUE-2 the percent of expected yield generally increases from west to east.

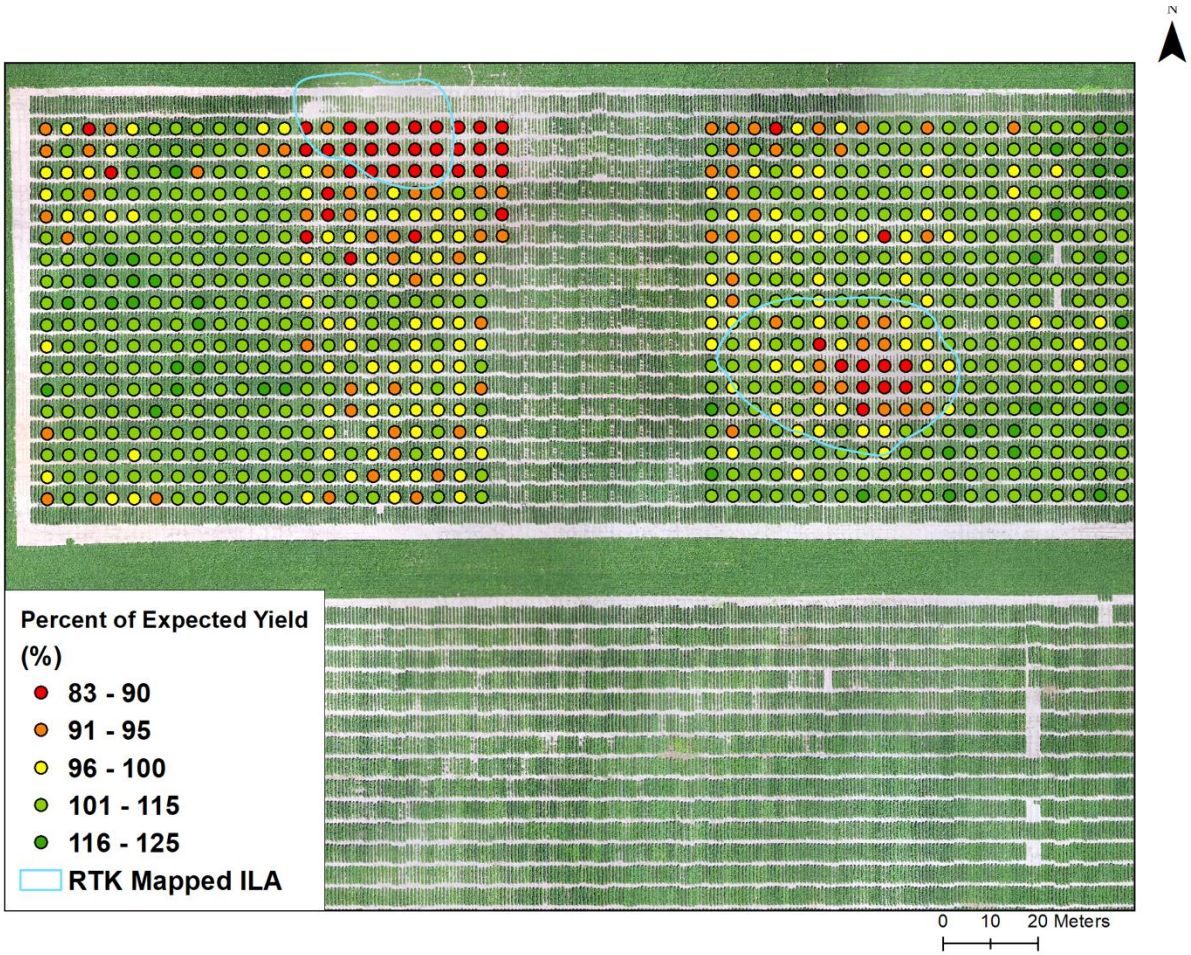

Figure 4.12. Percent of expected yield (%) from excess water stress at the R4-R5 stage. Values between 83-95% (red to orange) indicate areas predicted more likely to have a lower yield, whereas values greater than 95% (yellow to green) predict a higher estimate of yield.

4.4 Discussion

The discussion is divided into three sections evaluating the approach to quantify the impacts of excess water stress on soybean yield and underscoring notable developments and future work needed. The sections discussed are the data processing pipeline, estimation of biomass and quantifying impacts of excess water stress on yield.

4.4.1 UAS data processing pipeline

A data processing pipeline was developed for high-throughput phenotyping at the plot level with CIE and VID (Lyu et al., 2019). The developed tools enabled calibration and plant phenotyping at

the plot scale for multiple flight dates to estimate potential yield loss by excess water stress. This form of data processing can be time and data intensive as indicated by Shi et al. (2016). In their study 38,000 plots were manually extracted from orthomosaics (Shi et al., 2016). Creating automated tools to extract plot images, calibrate images and apply band algorithms can be additional challenges that limit time needed to answer primary objective science questions. CIE and VID are Python tools that were developed to reduce the aforementioned burden and place more time and focus on the science questions. Yu et al. (2016) and Maimaitijiang et al. (2020) have used orthomosaics for plant phenotyping of soybean generated from stitched images with RGB, multispectral and thermal sensors on UAS platforms. In this study orthomosaics were also used for estimating biomass from multispectral stitched images. CIE now has the capability to extract plots from the original images from RGB, multispectral and thermal imagery, which can generate multiple replicate plot images within an experiment. Future research should analyze the original images and test data fusion and/or deep learning to predict yield.

4.4.2 Predicting above-ground biomass

By expanding the methodology developed from Jackson et al. (1999) and Chan et al. (2013) for estimation of VWC to estimate above-ground biomass for different soybean classes (HY, HYD and DA) and across all classes proved to be representative and transferable. The incorporated adjustable stem water content variable provided only minor improvements when compared to the constant stem factor. This finding provides insight that the estimated biomass was not significantly influenced by the adjustable stem factor. Parameters used to estimate biomass representing all genetic classes within RUE-1 had low PBIAS and satisfactory RMSE. The equation used for all classes in RUE-1 was transferred to RUE-2 to estimate biomass for all plots. Estimated biomass in RUE-2 had satisfactory PBIAS and RMSE but was generally overestimated when compared with in-situ data. The overestimation in RUE-2 is attributed to biomass values (and associated parameters) from RUE-1 to be generally higher than biomass in RUE-2, which caused estimated values in RUE-2 to have a positive bias. The soybean plots in RUE-1 had less occurrences of inundation with an average biomass and yield of 278 g/m^2 and 4,150 kg/ha, respectively. Comparatively, RUE-2 had more occurrences of ILA and lower average biomass and yield of approximately 263 g/m^2 and 3,680 kg/ha, respectively. Representative variability in estimated biomass was observed in RUE-1 and RUE-2, where low values corresponded with mapped ILA.

The transferability demonstrates the potential use in future research to develop models within a defined experiment and scale-up the model across multiple fields for plant phenotyping.

In our study, models were generated to estimate above-ground biomass at the R4-R5 stage using a flight one-day after sampling. The close interval between in-situ sampling and remotely sensed observation was an important factor for estimating adequate parameters to estimate biomass. In our study, the developed model to estimate biomass for all classes was applied to multiple flights during different development stages. Using the developed models for different development stages does introduce uncertainty. To build representative models to predict biomass, dense in-situ sampling to capture variability at important development stages with corresponding flight dates should be considered. Previous studies have shown the blooming to seed filling stages (R2-R5) to be critical for soybean yield prediction (F. Gao et al., 2018; Ma et al., 2001a; Maimaitijiang et al., 2020; X. Zhang et al., 2019).

4.4.3 Quantifying impacts of excess water stress on yield

Proximal remote sensing with digital terrain analysis was used to detect and estimate potential gross yield loss from excess water stress at the plot scale. The calculated and mapped TWI agreed with in-situ observations of ILA. TWI independently was not strongly correlated with percent difference in yield. TWI was measured at 1.5 m resolution, which highlighted the in-field variability of TWI. The TWI thresholds were used to provide an objective approach to distinguish inundation susceptibility between replicate plots. However, some plots that did experience flooding did not meet the threshold criteria and as a result were not used in comparison analysis. This study also showed plots located in areas of high TWI (>13.5) can have higher yields than plots located in areas of low TWI (<7.4) if the occurrence of ILA is limited and providing optimal soil moisture conditions for the soybean to thrive. For instance, plots in RUE-1 had less observed occurrences of ILA than plots in RUE-2, and as a result some plots developed in areas of high TWI had a higher yield than plots in RUE-2 located in areas of low TWI. For future studies, refining the TWI threshold criteria and including the number of occurrences of inundation may increase the sample size used for analysis or distinguish plots more susceptible to inundation better.

Incorporating estimated biomass with TWI improved the detection and estimation of yield loss caused by excess water stress. By comparing and evaluating plots impacted by ILA with replicate plots not impacted by ILA over the growing season, distinguishable differences in estimated biomass were identified in the early reproductive stages (R4-R6) which corresponds to the results of previous studies. In-situ experiments from Desmond et al. (1985) and Scott et al. (1989) calculated crop susceptibility factors for flood duration effects on indeterminate and determinate soybean, respectively. Results of their studies found agreement that the indeterminate and determinate soybean were most susceptible to flooding during early reproductive stages (Desmond et al., 1985; Scott et al., 1989).

Mapping the percent of expected yield with CIE provided the ability to evaluate the soybeans spatially at the R4-R5 stage. By integrating mapped ILA observations with digital terrain analysis from TWI, inferences relating to potential yield reduction due to excess water stress could be made with supportive data. Similar data fusion frameworks would be useful for stakeholders and provide the information needed to make management decisions.

4.5 Conclusion

Low gradient agricultural areas often experience ILA in the Midwest resulting in damaged crops and increased financial risk from yield loss. By identifying areas impacted by excess water stress early in the reproductive stages, stakeholders can assess risk and make investment plans for responsive management decisions. The potential of low-cost UASs to measure impacts of excess water stress on soybean development were analyzed and evaluated along with new tools, CIE and VID, designed to help with the extraction of plots within breeding experiments. Aims of this study were to (1) determine if proximal remote sensing can be used to predict biomass for different growth stages and (2) determine if that biomass estimate is sensitive to excess water stress. The main conclusions of the investigation are:

1. Proximal remote sensing from UASs is a representative predictor of biomass at the R4-R5 stage at the plot scale. Expanding the methodology developed from Jackson et al. (1999) and Chan et al. (2013) for estimation of VWC to estimate biomass proved to be representative and transferable. Soybean of varying classes (HY, HYD and DA) were

analyzed and a representative estimate of biomass for all genetic lines was generated. To improve model predictions, consideration should be made to ensure close temporal frequency between remotely sensed and in-situ observations in order to capture similar crop development stages.

2. Estimated biomass at early reproductive stages proved to be sensitive to excess water stress. The sensitivity of estimated biomass to excess water stress was analyzed and evaluated at the plot and field scale throughout the growing season. The sensitivity of estimated biomass sensitivity to excess water stress was most distinguishable in the early reproductive stages (R4-R6). Concentrated areas of low estimates of biomass showed agreement with mapped ILA and areas of high TWI.
3. Low estimates of percent of expected yield corresponded with observations of in-field flooding and areas with high TWI. Whereas high estimates of percent of expected yield corresponded with areas less susceptible to inundation. Estimates of potential yield reduction mapped with developed tools provide a useful crop status assessment at the R4-R5 stage.

The results of this study demonstrate transferable methods to estimate biomass at the plot level and potential to provide crop status assessments to stakeholders prior to harvest. Future work aims to (1) leverage satellite data to fill data gaps and analyze sensitivity of estimated biomass to water stress at larger scales and (2) incorporate model simulations to estimate a water stress index at varying scales.

Acknowledgements

This research was supported by the United States Department of Agriculture (2016-07982).

4.6 References

Alberto, B., District, S. P., Banitt, A., & Faber, B. (2015). Red River of the North at Fargo, North Dakota, Pilot Study, Impact of Climate Change on Flood Frequency Curve. Retrieved from http://www.corpsclimate.us/docs/Red_River_of_the_North_Adaptation_Pilot.pdf

Beven, K. J., & Kirkby, M. J. (1979). A physically based, variable contributing area model of basin hydrology. Hydrological Sciences Bulletin, 24(1), 43–69. https://doi.org/10.1080/02626667909491834

Chan, S., Bindlish, R., Hunt, R., Jackson, T., & Kimball, J. (2013). Ancillary Data Report: Vegetation Water Content, (SMAP Science Document 047), 1–15. Retrieved from smap.jpl.nasa.gov

Chen, D., Huang, J., & Jackson, T. J. (2005). Vegetation water content estimation for corn and soybeans using spectral indices derived from MODIS near- and short-wave infrared bands. Remote Sensing of Environment, 98(2–3), 225–236. https://doi.org/10.1016/j.rse.2005.07.008

Chipman, J. ., Olmanson, L. G., & Gitelson, A. . (2009). Remote sensing methods for lake management. Environmental Protection.

D. W. DeBoer and W. F. Ritter. (1970). Flood Damage to Crops in Depression Areas of North-Central Iowa. Transactions of the ASAE, 13(5), 0547–0549. https://doi.org/10.13031/2013.38659

Desmond, E., Barkle, G. F., & Shwab, G. O. (1985). Soybean Yield Response to Excess Water. In 1985 Winter Meeting American Society of Agricultural Engineers (pp. 1–12).

Evans, R. O., & Fausey, N. R. (1999). Effects of Inadequate Drainage on Crop Growth and Yield. In Agricultural Drainage, Agronomy Monograph 38 (pp. 13–54).

Fehr, W. R., Caviness, C. E., Burmood, D. T., & Pennington, J. S. (1971). Stage of Development Descriptions for Soybeans, Glycine Max (L.) Merrill 1 . Crop Science, 11(6), 929–931. https://doi.org/10.2135/cropsci1971.0011183x001100060051x

Gao, B. C., & Goetzt, A. F. H. (1995). Retrieval of equivalent water thickness and information related to biochemical components of vegetation canopies from AVIRIS data. Remote Sensing of Environment, 52(3), 155–162. https://doi.org/10.1016/0034-4257(95)00039-4

Gao, F., Anderson, M., Daughtry, C., & Johnson, D. (2018). Assessing the variability of corn and soybean yields in central Iowa using high spatiotemporal resolution multi-satellite imagery. Remote Sensing, 10(9). https://doi.org/10.3390/rs10091489

Griffin, J. L., & Saxton, A. M. (1988). Response of Solid-Seeded Soybean to Flood Irrigation. II. Flood Duration. Agronomy Journal, 80(6), 885. https://doi.org/10.2134/agronj1988.00021962008000060009x

Grimm, K., Tahmasebi Nasab, M., & Chu, X. (2018). TWI Computations and Topographic Analysis of Depression-Dominated Surfaces. Water, 10(5), 663. https://doi.org/10.3390/W10050663

Jackson, T. J., Le Vine, D. M., Hsu, a Y., Oldak, a, Starks, P. J., Swift, C. T., Isham, J. D., & Haken, M. (1999). Soil moisture mapping at regional scales using microwave radiometry: the Southern Great Plains Hydrology Experiment. Geoscience and Remote Sensing, IEEE Transactions On, 37(5), 2136–2151. https://doi.org/10.1109/36.789610

Johnson, D. M. (2014). An assessment of pre- and within-season remotely sensed variables for forecasting corn and soybean yields in the United States. Remote Sensing of Environment, 141, 116–128. https://doi.org/10.1016/j.rse.2013.10.027

Jones, H. G., & Vaughan, R. A. (2010). Remote sensing of vegetation: principles, techniques, and applications. Oxford University Press.

Kim, Y., Jackson, T., Bindlish, R., Lee, H., & Hong, S. (2012). Radar Vegetation Indices for Estimating the Vegetation Water Content of Rice and Soybean. Geoscience and Remote Sensing Letters, 9(4), 564–568. https://doi.org/10.1109/LGRS.2011.2174772

Kross, A., McNairn, H., Lapen, D., Sunohara, M., & Champagne, C. (2015). Assessment of RapidEye vegetation indices for estimation of leaf area index and biomass in corn and soybean crops. International Journal of Applied Earth Observation and Geoinformation, 34(1), 235–248. https://doi.org/10.1016/j.jag.2014.08.002

Liu, J., Pattey, E., Miller, J. R., McNairn, H., Smith, A., & Hu, B. (2010). Estimating crop stresses, aboveground dry biomass and yield of corn using multi-temporal optical data combined with a radiation use efficiency model. Remote Sensing of Environment, 114(6), 1167–1177. https://doi.org/10.1016/j.rse.2010.01.004

Lobell, D. B. (2013). The use of satellite data for crop yield gap analysis. Field Crops Research, 143, 56–64. https://doi.org/10.1016/j.fcr.2012.08.008

Lobell, D. B., Asner, G. P., Ortiz-Monasterio, J. I., & Benning, T. L. (2003). Remote sensing of regional crop production in the Yaqui Valley, Mexico: Estimates and uncertainties. Agriculture, Ecosystems and Environment, 94(2), 205–220. https://doi.org/10.1016/S0167-8809(02)00021-X

Lyu, B., Smith, S. D., Xue, Y., & Cherkauer, K. A. (2019). Deriving Vegetation Indices from High-throughput Images by Using Unmanned Aerial Systems in Soybean Breeding. ASABE 2019 Annual International Meeting, 1–15. https://doi.org/10.13031/aim.201900279

Ma, B. L., Dwyer, L. M., Costa, C., Cober, E. R., & Morrison, M. J. (2001a). Early prediction of soybean yield from canopy reflectance measurements. Agronomy Journal, 93(6), 1227–1234. https://doi.org/10.2134/agronj2001.1227

Ma, B. L., Dwyer, L. M., Costa, C., Cober, E. R., & Morrison, M. J. (2001b). Early Prediction of Soybean Yield from Canopy Reflectance Measurements. Agron. J, (93), 1227–1233. https://doi.org/10.2134/agronj2001.1227

Maimaitijiang, M., Sagan, V., Sidike, P., Hartling, S., Esposito, F., & Fritschi, F. B. (2020). Soybean yield prediction from UAV using multimodal data fusion and deep learning. Remote Sensing of Environment, 237(December 2019), 111599. https://doi.org/10.1016/j.rse.2019.111599

Monteith. (1972). Solar Radiation and Productivity in Tropical Ecosystems Author (s): J . L . Monteith Source : Journal of Applied Ecology , Vol . 9 , No . 3 (Dec ., 1972), pp . 747 -766 Published by : British Ecological Society Stable URL : http://www.jstor.org/stable/. Society, 9(3), 747–766.

Monteith, J. L., & Moss, C. J. (1977). Climate and the Efficiency of Crop Production in Britain [and Discussion]. Philosophical Transactions of the Royal Society B: Biological Sciences, 281(980), 277–294. https://doi.org/10.1098/rstb.1977.0140

Pack, D. J. (2015). About $300 million in Indiana crops' value lost to flooding so far - Parke County - Purdue Extension. Retrieved May 16, 2018, from https://extension.purdue.edu/Parke/pages/article.aspx?intItemID=10734

Quinn, P. F., Beven, K. J., & Lamb, R. (1995). The ln(a/tan Beta) index: How to use it within the TOPMODEL framework. Hydrological Processes, 9(April 1994), 161–182.

Scott, H. D., DeAngulo, J., Daniels, M. B., & Wood, L. S. (1989). Flood Duration Effects on Soybean Growth and Yield. Agronomy Journal, 81(4), 631. https://doi.org/10.2134/agronj1989.00021962008100040016x

Shi, Y., Thomasson, J. A., Murray, S. C., Pugh, N. A., Rooney, W. L., Shafian, S., Rajan, N., Rouze, G., Morgan, C. L. S., Neely, H. L., Rana, A., Bagavathiannan, M. V, Henrickson, J., Putman, E. B., Popescu, S., Burks, T., Cope, D., & Ibrahim, A. (2016). Unmanned Aerial Vehicles for High- Throughput Phenotyping and Agronomic. Plos One, c(July 2016), 1–26. https://doi.org/10.5061/dryad.65m87

Smith, G. M., & Milton, E. J. (1999). The use of the empirical line method to calibrate remotely sensed data to reflectance. International Journal of Remote Sensing, 20(13), 2653–2662. https://doi.org/10.1080/014311699211994

Song, Q., Yan, L., Quigley, C., Jordan, B. D., Fickus, E., Schroeder, S., Song, B., Charles An, Y., Hyten, D., Nelson, R., Rainey, K., Beavis, W. D., Specht, J., Diers, B., & Cregan, P. (2017). Genetic Characterization of the Soybean Nested Association Mapping Population. The Plant Genome, 10(2), plantgenome2016.10.0109. https://doi.org/10.3835/plantgenome2016.10.0109

Widhalm, M., Hamlet, A., Byun, K., Robeson, S., Baldwin, M., Staten, P., Chiu, C., Coleman, J., Hall, B., Hoogewind, K., Huber, M., Kieu, C., Yoo, J., & Dukes, J. (2018). Indiana's Past & Future Climate: A Report from the Indiana Climate Change Impacts Assessment. Climate Change Reports. https://doi.org/10.5703/1288284316634

Yilmaz, M. T., Hunt, E. R., & Jackson, T. J. (2008). Remote sensing of vegetation water content from equivalent water thickness using satellite imagery. Remote Sensing of Environment, 112(5), 2514–2522. https://doi.org/10.1016/j.rse.2007.11.014

Yu, N., Li, L., Schmitz, N., Tian, L. F., Greenberg, J. A., & Diers, B. W. (2016). Development of methods to improve soybean yield estimation and predict plant maturity with an unmanned aerial vehicle based platform. Remote Sensing of Environment, 187, 91–101. https://doi.org/10.1016/j.rse.2016.10.005

Zhang, J., Xu, Y., Yao, F., Wang, P., Guo, W., Li, L., & Yang, L. (2010). Advances in estimation methods of vegetation water content based on optical remote sensing techniques. Science China Technological Sciences, 53(5), 1159–1167. https://doi.org/10.1007/s11431-010-013-3

Zhang, X., Zhao, J., Yang, G., Liu, J., Cao, J., Li, C., Zhao, X., & Gai, J. (2019). Establishment of plot-yield prediction models in soybean breeding programs using UAV-based hyperspectral remote sensing. Remote Sensing, 11(23). https://doi.org/10.3390/rs11232752

5. QUANTIFYING YIELD IMPACTS ON SOYBEAN FROM EXCESS WATER USING RAPIDEYE

Abstract

Distinguishing the impacts of inundated land area (ILA) on crop yield from other yield-impacting factors provide stakeholders and government agencies with information to support immediate and future decisions related to agricultural management and risk assessment. The utility of unmanned aerial systems (UASs) and spaceborne platforms can be leveraged to develop models at the field scale for application over larger areas to quantify the impacts of ILA on crop development. However, developing transferable models often requires a range of in-situ data and access to UAS and satellite imagery which can be labor and cost intensive. In this study, the impacts of ILA on soybean development at early reproductive stages are evaluated over multiple fields and crop years in west-central Indiana. The objectives of the study are to (1) estimate biomass remotely with satellite imagery using model developed for UAS data, (2) estimate percent of expected yield with satellite imagery using a model developed from UAS data and (3) analyze the impacts of excess water to soybean across multiple fields and years. The results of the study show that model estimates, designed at the field scale and applied over larger areas using satellite imagery, are sensitive to excess water and agree with in-situ observations. The study demonstrates the usage and potential of complimentary measurements from UASs and spaceborne platforms to identify soybean impacted by ILA between the R4-R6 development stages and support stakeholders with information at varying spatiotemporal scales.

5.1 Introduction

Delivering early assessments of crop conditions to agricultural stakeholders can provide information for immediate and future management decisions. For a farmer, early estimates of yield impacts provide a baseline within a field and can help make marketing decisions for their crop. For policy makers and governments, the early estimates provide forecasts of the supply and demand of crop resources. The United States Department of Agriculture (USDA) National Agricultural Statistics Service (NASS) and Risk Management Agency (RMA) work to report forecasted yield of commodity crops and prevented planted acreage from in-field flooding. Large

surveys are conducted by NASS throughout the growing season. The vital surveys require trained enumerators and in-situ sampling, which are time, labor and cost intensive (Di et al., 2017; Johnson, 2014). For future management decisions, quantification of the impact of excess water stress on yield can help farmers plan future planting schemes, application of fertilizer and irrigation as well as investments in drainage practices to decrease the yield gap. In a changing climate, excess water stress can negatively impact crop yield (Smith et al., 2020). Assessing risk prior to harvest can help farmers and insurance companies file and process insurance claims and remain transparent in the sharing of information.

Inundated land area (ILA) is the extent of land surface covered by water following snowmelt, extensive rain events and saturated soil, and occurs after water has accumulated within local depressions which are typically less than one meter in depth. ILA can impact agricultural production and decrease crop yield in wet years, although in dry years concentration of available water may enhance yield in local depressions. Water availability can impact soybean development during different development stages. Reproductive stages when the soybean is vulnerable to in-field flooding are when the pod begins to fill (R2) up until the seed is filled (R6) (Desmond et al., 1985; Gao et al., 2018; Licht et al., 2011; Ma et al., 2001; Maimaitijiang et al., 2020; Smith et al. 2020). The R4 development stage occurs once the pods are full, approximately mid-July. At the R5 stage seed filling begins. The R6 stage occurs once the seed has filled the pod, in early August (Fehr et al., 1971).

Potential yield impacts of ILA over agricultural fields can be quantified using remote sensing from satellites and unmanned aircraft systems (UASs) (Di et al., 2017; Shrestha et al., 2013). Spaceborne platforms have the ability to observe larger areas than UAS platforms and are often equipped with greater spectral range. However, in order to distinguish fields from one crop to another such as soybean and corn as well as capture in-field flooding, higher spatial and temporal resolution are necessary (Liu et al., 2010; Mulla, 2013). MODIS for example, has a daily temporal resolution and a moderate spatial resolution of 250 m. Although the temporal resolution is acceptable, the spatial resolution may not be able to distinguish between fields. On the other hand, Landsat 8 has a 16-day temporal resolution with a higher spatial resolution of 30 m. Landsat has the ability to distinguish fields but may not have the temporal resolution needed to capture the

effects of in-field flooding during critical development stages that can provide inferences of crop yield, such as the R4 to R6 stage for soybean. Satellite constellations that consist of multiple systems with similar characteristics can provide higher spatial and temporal resolutions. For instance, the RapidEye and PlanetScope constellations provide multi-spectral imagery with spatial resolution of 5 m and 3 m, respectively with multiple observations per week.

Models driven with remotely sensed data are increasingly being used to provide an alternative method to assess crop development and predict yield. Remotely sensed measurements of above-ground biomass (g/m^2) or leaf area index (LAI) (m^2/m^2) typically apply multispectral imagery within a model to estimate the desired crop parameter (Kross et al., 2015; Smith et al., 2020). Unlike more traditional physical sampling methods, this approach does not damage the crop, is less time and cost intensive and allows larger areas to be assessed. The estimated crop parameters can also be incorporated into models to predict yield (Lobell, 2013). Yield forecasts are typically made using surveys, statistical or crop models. Surveys use field collected samples to develop statistical regressions with historical yield data to predict yield. Statistical and crop models can use remotely sensed data to improve yield forecast. For instance, remotely sensed observations can improve model skill by updating model variables, driving model simulations or improving model parameterization (Basso et al., 2019). Previous research has also investigated coupling statistical and crop models with remotely sensed imagery to provide field scale yield estimates (Dado et al., 2020; Lobell et al., 2015). As remote sensing becomes increasingly integrated into agricultural applications, developed models need to be routinely tested and enhanced as well as be increasingly adaptable for application to larger areas. Flood assessment models incorporating crop damage may need to include the variation in impact from early recovery to longer-term impacts appearing only in the weeks following an event (Di et al., 2017). Such models could help determine crop loss and accelerate financial recovery through insurance claims.

Few studies have investigated the potential of leveraging the measurements from UASs to design models at the field scale for application over larger areas with satellite imagery. The use of small, low-cost UASs with multi-spectral cameras provides an opportunity to design models at the field scale that can be made transferable for high resolution satellite imagery and applied over larger areas. Research constraints are due to limited availability or access to the in-situ data needed to

develop and validate models as well as limited access to both UAS and satellite imagery. This study is unique in that in-situ biomass data were acquired at significant soybean development stages and yield data were obtained over multiple fields and years. In addition, cloud-free UAS and satellite imagery were collected at a similar temporal resolution over the areas of interest. These combined factors allow for models to be developed and tested under similar conditions. This in turn provides an opportunity to investigate the potential of leveraging low-cost UASs to support field scale analysis over large areas with satellite imagery, which have the potential to support early recovery assessments related to ILA and support USDA NASS goals by reducing the labor and costs to conduct large surveys. The objectives of this study are to (1) Estimate biomass remotely with satellite imagery using a model developed for UAS data, (2) Estimate the percent of expected yield that was realized following excess water (relative yield) with satellite imagery using a model developed from UAS data and (3) Analyze the impacts of excess water on yield across multiple fields and years.

5.2 Methods

5.2.1 Study area

The focus of this study are soybean fields at the Agronomy Center for Research and Education (ACRE) located in north-central Indiana (40.47°N, 86.99°W). ACRE is an active research farm, where fields represent typical planting conditions for Indiana. Fields at ACRE have minimal topographic gradient with a soil texture that is predominantly silty clay loam. The dominant soil series are a Chalmers silty clay loam and Raub-Brenton silt loam. The poorly drained soil has subsurface drainage with a 20 m spacing at a depth of approximately 1 m in all fields. The ten fields of interest (Figure 5.1) are managed using an annual corn and soybean rotation. Each field is approximately 4 ha in area. In this study, each field was included in the analysis only when used to grow bulk soybeans (> 0.81 ha). During the analysis period, from 2015 to 2019, the number of fields available for this projected ranged from three to four.

Figure 5.1 shows the topographic wetness index (TWI) values for the fields of interest at ACRE. The TWI is a function of the contributing drainage area per contour length over the surface slope and is used to identify hydrologically similar areas (Beven et al., 1979). In this study, the TWI is

used to identify areas susceptible to ILA. The fields of interest have isolated areas of increased TWI where local depressions are located, and ILA can occur from excess water. In 2019 areas of observed ILA were mapped using Real Time Kinematic surveying. Figure 5.1 shows the mapped ILA within the soybean field is located in an area with a TWI of approximately 8.

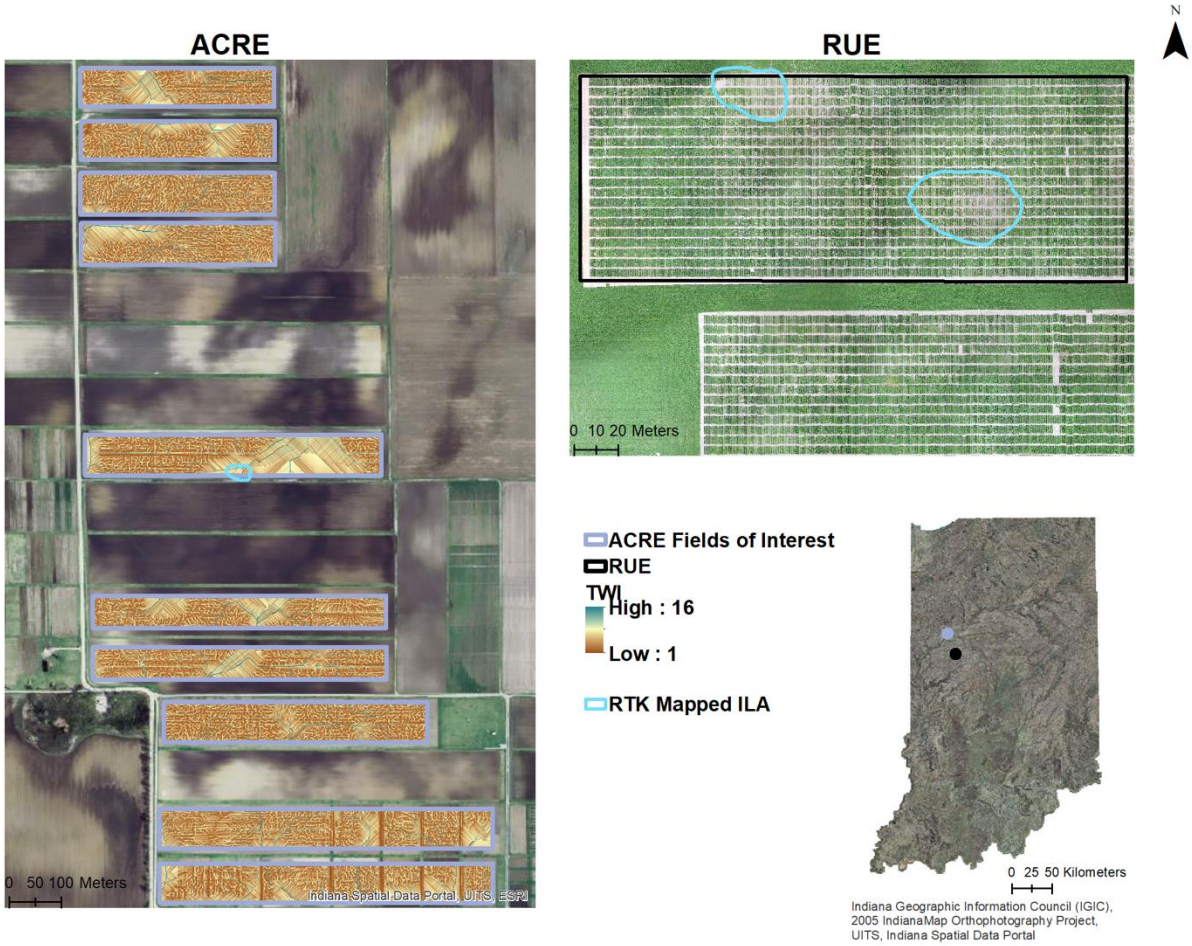

Figure 5.1: Left panel shows the southern portion of the Agronomy Center for Research and Education (ACRE), with the fields used in the study highlighted. Right top panel shows the research farm where radiation a use efficiency (RUE) experiment (highlighted in black) is used to develop models with soybean. ACRE and RUE fields are managed with an annual corn and soybean rotation, and both sites have experienced inundation that was mapped with an RTK in 2018. Bottom panel shows relative locations of both experiments in west-central Indiana.

5.2.2 Data acquisition

Satellite, precipitation and yield data were used to evaluate the impact of excess water on bulk fields at ACRE from 2015 to 2019. Observed soybean yield was used to calculate the relative yield attained each year for comparison with remotely sensed estimates. Quantification of the relative yield is discussed in Section 2.4. ACRE fields were planted approximately mid-May and harvested early October with a combine, and yield measurements were collected from a yield monitor. Fields planted in bulk soybean (i.e., not planted for research purposes) varied each year, however the total area in bulk soybeans was similar for each year. Daily precipitation (mm) data were used to analyze estimated model outputs and evaluate the impacts of excess water on soybean development during seed filling (stages R4 to R6) that in Indiana occurs between mid-July and early August. Cumulative precipitation was calculated from April 1st to July 15th for each growing season to capture total precipitation prior to remotely sensed observations. Precipitation data were collected from a National Weather Service Cooperative Observe Program (NWS COOP 129430) weather station located at ACRE (Midwestern Regional Climate Center, 2019). Table 5.1 lists the cumulative early growing season precipitation from 2015 to 2019, where 2015 and 2017 have the highest cumulative precipitation of 573 mm and 561 mm, respectively.

Satellite imagery from RapidEye was used to estimate biomass and relative yield of soybean over bulk fields at ACRE. RapidEye is a constellation of five satellites with a spatial resolution of 5 m and five multispectral bands: blue, green, red, red edge and near-infrared (NIR). RapidEye was retired in 2020 and PlanetScope has since filled its position with a similar spatial resolution (3 m) and imaging bands (blue, green, red and NIR). The RapidEye products downloaded from Planet were orthorectified with radiometric corrections applied (Level 3A). The aim was to collect one image per year between the R4 and R6 stages of soybean with no cloud coverage over the fields of interest. This time window was selected because of the importance of the early reproductive stages to yield (Desmond et al., 1985; Gao et al., 2018; Ma et al., 2001; Maimaitijiang et al., 2020; Smith et al., 2020). As a result, one scene per year was collected between July 17th and July 27th from 2015 to 2019 (Table 5.1).

Table 5.1: Observed and remotely sensed data collected from the Agronomy Center for Research and Education from 2015 to 2019.

Crop Year	Median Yield (kg/ha)	Cumulative Precipitation (mm) between April 1st – July 15th	RapidEye imagery
2015	3302	573	July 21st
2016	3649	310	July 27th
2017	4357	561	July 25h
2018	3852	324	July 17th
2019	3633	364	July 25th

5.2.3 Estimating biomass

Soybean biomass (g/m^2) was estimated remotely with a model that was developed in prior work using in-situ biomass data and multi-spectral UAS imagery at the field scale (Smith et al., 2020). This product is hereafter referred to as the UAS biomass model. The in-situ biomass data consisted of a total of 868 biomass samples that were collected from a soybean breeding experiment conducted at a nearby research farm also located in west-central Indiana (RUE experiment; Figure 5.1). Samples used for this analysis were collected on July 16th, 2018 (60 days after planting) between the R4-R5 stage. The experiment was designed to evaluate differences in radiation use efficiency (RUE) from recombinant inbred lines (RILs) with varying genes, that were replicated between two neighboring experiment plots. In this work, the UAS biomass model was applied to RapidEye imagery to estimate the soybean biomass and will hereafter be referred to as RapidEye biomass.

The UAS biomass represents the above-ground biomass using a combination of band algorithms and estimated parameters, which are sensitive to the water content in the crop canopy (Chan et al., 2013) and excess water stress (Smith et al., 2020). Equation 5.1 lists the calculation to estimate biomass from Smith et al. (2020) using two terms.

$$Biomass\ (g/m^2) = (a * NDVI^2 + b * NDVI) + \psi * \frac{NDVI_{max} - NDVI_{min}}{1 - NDVI_{min}} + c \qquad (5.1)$$

The first term represents the foliage of the soybean canopy using the normalized difference vegetation index (NDVI). The second term represents the stem water content using a stem factor,

ψ, and NDVI extremes (maximum and minimum). The stem factor is the band ratio of NIR_{ref} and $Green_{ref}$. The output parameters, $a, b\ and\ c$ are from the SciPy optimization tool package used to estimate parameters using non-linear least squares. The parameters were estimated using the relationship between measured biomass from the RUE plots and NDVI (n=868) from the multi-spectral imagery.

The RapidEye biomass model was developed by fitting the UAS biomass model to parameters estimated with RapidEye imagery collected over the RUE experiment on July 17th, 2018. The estimated parameters are 4564, -5042 and 1450 for $a, b\ and\ c$, respectively. The RapidEye biomass model is sensitive to excess water stress and was applied over ACRE fields of interest from crop years 2015 to 2019.

5.2.4 Quantifying percent of expected yield

The RapidEye biomass and harvester yield data were used to estimate the percent of expected yield, a measure of relative yield, at ACRE. The percent of expected yield, rather than yield, is used in order to provide an assessment of yield impact of excess water relative to the yield potential for a given soil, climate and hybrid and identify areas that may be at risk due to excess water stress. The percent of expected yield (%) is the predicted yield outcome relative to the expected yield. At ACRE, the observed expected yield was defined as the median yield in 2018, which was the crop year for which the UAS biomass and UAS expected yield models were developed from the RUE experiment. The percent of expected yield or relative yield was then calculated as 100% times the ratio of reported yield each year to the 2018 median yield.

Smith et al. (2020) developed a model to estimate the impact of ILA on the percent of expected yield (hereafter referred to as UAS relative yield) by comparing differences in estimated biomass between the wetter and drier replicate plots, identified using topographic wetness index (TWI). Equation 5.2 was used to calculate the UAS relative yield in percent, where x, is the relative biomass obtained from RapidEye.

$$UAS\ Relative\ Yield = 0.32x + 72 \tag{5.2}$$

Relative biomass is the calculated ratio of the estimated biomass (g/m^2) to the field average biomass (g/m^2). By not using the estimated biomass directly, the relative biomass indicator avoids biases introduced by changing sensors thus increasing the transferability of the biomass models to different remote sensing platforms such as UASs and satellites that may have different spectral ranges or sensitivities and differing spatial resolutions. The UAS relative yield model was applied over larger areas and multiple growing seasons (2015-2019) using RapidEye biomass inputs to estimate percent of expected yield (hereafter referred to as RapidEye relative yield). The RapidEye relative yield was analyzed to predict yield change due to early season inundation based on RapidEye biomass estimates from late July.

5.2.5 Estimating yield decline and gain

Saturated soils in local depressions from ILA can cause declines in soybean yield as the duration and occurrence of inundation increases (DeBoer and Ritter, 1970; Desmond et al., 1985; Evans et al., 1999). On the other hand, if the occurrence and duration of inundation are limited these local depressions can provide ideal soil water conditions for soybean to develop without stress later in the season. Smith et al. (2020) predominantly observed negative impacts to soybean that were exposed to excess water, where soybean plots located in areas susceptible to ILA had lower yield compared to plot replicates located in areas less susceptible to ILA. Conversely, the study also observed instances where soybean plots located in areas more susceptible to ILA had higher yield than plot replicates located in areas less susceptible to ILA. These instances of higher yield are likely the result of ILA that did not cause significant damage to the plant due to limited duration, but the greater soil water storage in these locations provided improved water availability for the soybean late in the season, which allowed it to thrive compared to the plot replicate.

In this study we estimate average yield decline and gain in relation to the average yield to determine the impacts of water availability on soybean yield from crop years 2015 to 2019. As shown in equations 5.3 and 5.4, respectively, yield decline and gain were estimated for each field by multiplying the annual median yield across all fields with the zone of the field associated with a yield decline or yield gain and the average relative yield (as a fraction) within the zone. The zone of the field associated with yield decline was determined for each field by calculating the area of the field where relative yield was below 100% and dividing by the total area of the field. The zone

of field associated with yield gain was computed similarly using areas with relative yield at or above 100%. ArcGIS was used to calculate the fractional area of yield impact and zonal statistics were used to estimate the average relative yield within the fraction.

$$Yield\ Decline\ \left(\frac{kg}{ha}\right) = annual\ median\ yield \cdot (1.0 - relative\ yield\ (fraction)) \cdot fraction\ of\ field\ with\ yield\ decline \tag{5.3}$$

$$Yield\ Gain\ \left(\frac{kg}{ha}\right) = annual\ median\ yield \cdot (relative\ yield\ \ (fraction) - 1.0) \cdot fraction\ of\ field\ with\ yield\ gain \tag{5.4}$$

5.3 Results

5.3.1 Estimating biomass

Figure 5.2 illustrates the relationship between RapidEye and observed biomass of soybean (g/m^2). The RapidEye biomass was estimated from a RapidEye image from July 17th, 2018 using equation 5.1 whereas in-field biomass samples were collected on the previous day from the RUE experiment. The estimated biomass follows the 1:1 line with a calculated percent bias less than 0.1% and root mean square error of 69 g/m^2.

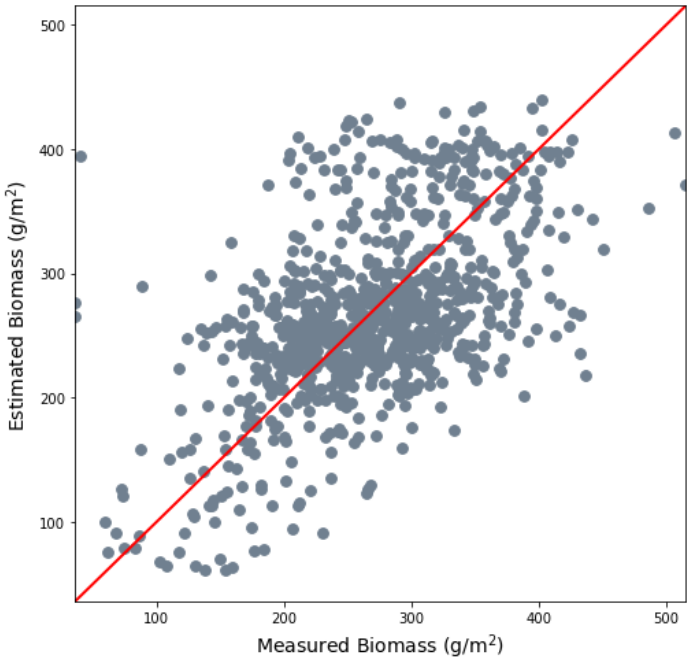

Figure 5.2: Comparison of estimated biomass (g/m^2) and measured biomass (g/m^2). (n=868). Percent bias and root mean square error of <0.1% and 69 g/m^2

RapidEye biomass estimates of soybean are mapped to individual plots for the RUE experiment in Figure 5.3. These estimates are based on an image from July 17th, which is in the R4-R5 stage for all soybean varieties pictured. From the map it can be seen that the range of estimated biomass is from 61 g/m^2 to 440 g/m^2. The higher biomass values are found in the western section of the field, which also had an average yield of 4145 kg/ha at the end of season. Lower biomass estimates are found in the eastern section of the field, where the average yield was 11% lower than the western section at the end of the season. Low estimates of biomass are also associated with observed inundated land area which were mapped with an RTK system in the beginning of July when the soybeans were between the R1-R2 stage (Figure 5.3). This ILA was observed following heavy precipitation that accumulated in local depressions within the field. Despite the presence of subsurface drainage installed in the fields (as with most Indiana agricultural fields), ILA has been observed to persist for at least two days at this experimental farm. The RapidEye biomass was found to be in agreement with the in-situ data (Figure 5.2) where low biomass estimates correspond spatially with observed instances of in-field flooding (Figure 5.3). To investigate the impacts of excess water on yield of soybean at ACRE, we applied the RapidEye biomass developed from the RUE experiment to the soybean fields of interest at ACRE.

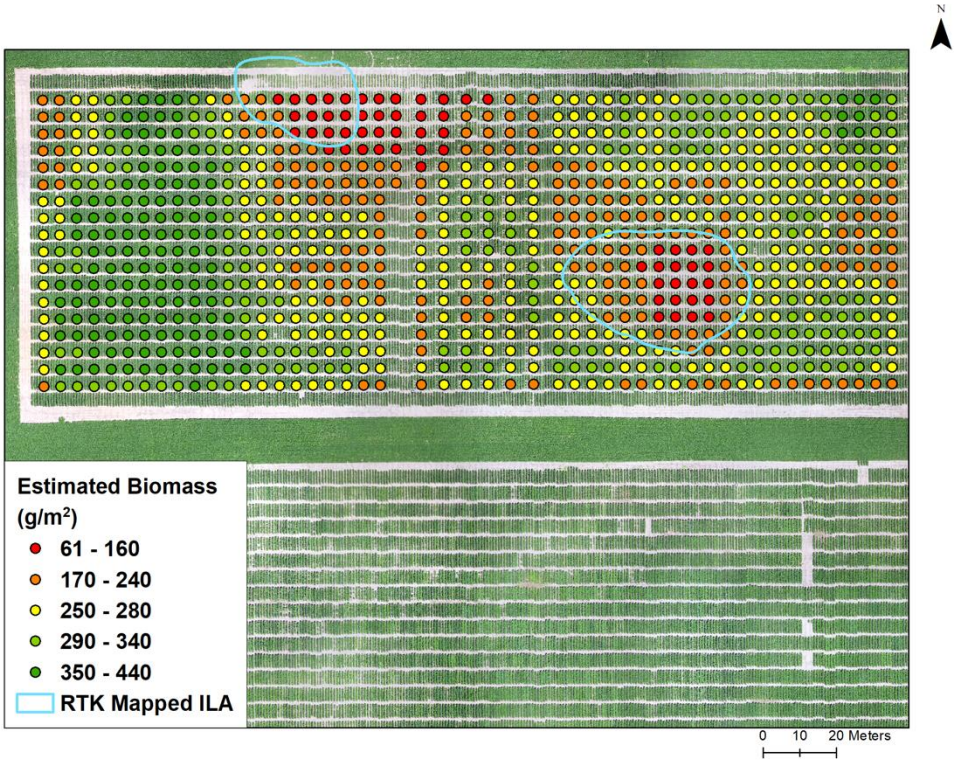

Figure 5.3: Estimated biomass from research field in north-central Indiana. Field was used to develop model using collected biomass (n=869) at the early reproductive stages (R4-R5).

Field average RapidEye biomass (g/m^2) estimated at ACRE between the R4 to R6 stages is shown in relation with harvested yield (kg/ha) between crop years 2015 and 2019 in Figure 5.4. The figure shows that as biomass increases, yield also increases, where the positive linear correlation between yield and biomass is significant with a coefficient (r) of 0.80. The RapidEye biomass at the early reproductive stages correlates with the measured yield across multiple growing seasons (2015-2019).

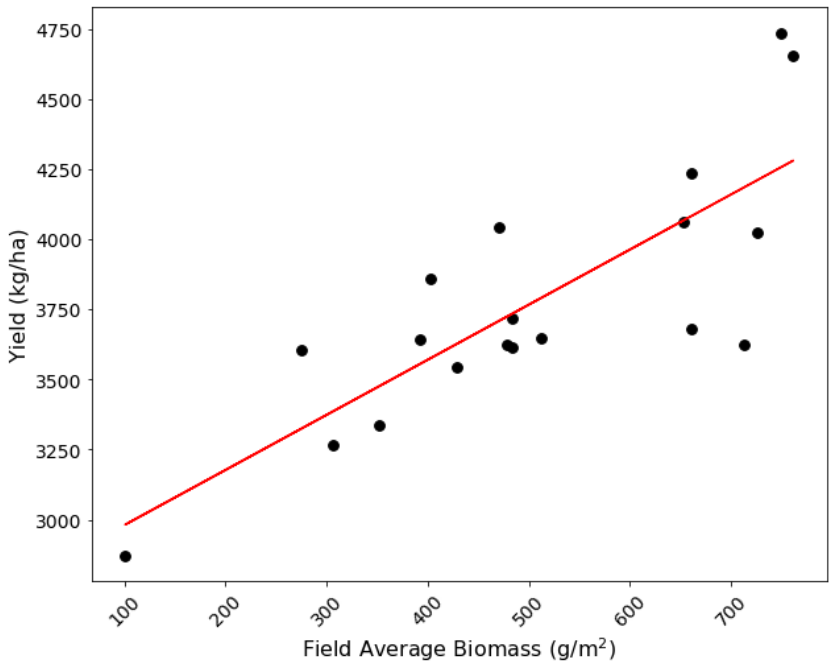

Figure 5.4: Soybean yield with respect to average estimated biomass at early reproductive stages (R4-R6) for each field of interest from 2015 to 2019.

To analyze the impact of excess water stress on RapidEye biomass fields are compared between years. In crop years 2015 and 2019, similar fields were planted with soybean and cumulative precipitation between April 1st and July 15th was 573 mm and 364 mm, respectively. Figure 5.5 shows a panel comparison of estimated biomass between R4-R6 at fields of interest for crop years 2015 and 2019. In general, the fields in 2015 have a lower biomass compared with the fields in 2019, with an average biomass of 259 g/m^2 and 456 g/m^2 and yields of 3300 kg/ha and 3700 kg/ha, respectively. The areas with the lowest biomass are also associated with areas susceptible to ILA. In 2015, the ILA was more extensive and expanded radially from the local depressions impacting not only the biomass within the local depressions but also the biomass adjacent to the local depressions (Figure 5.5). The fields in 2015 also have a lower yield compared with the fields in 2019, with an average yield of 3300 kg/ha and 3700 kg/ha, respectively. In 2019, the impacts of ILA on biomass are less extensive than 2015, resulting in greater biomass and yield. ILA was observed and remotely sensed within isolated sections of the field where lower estimates (<140 g/m^2) of biomass are identified (Figure 5.5).

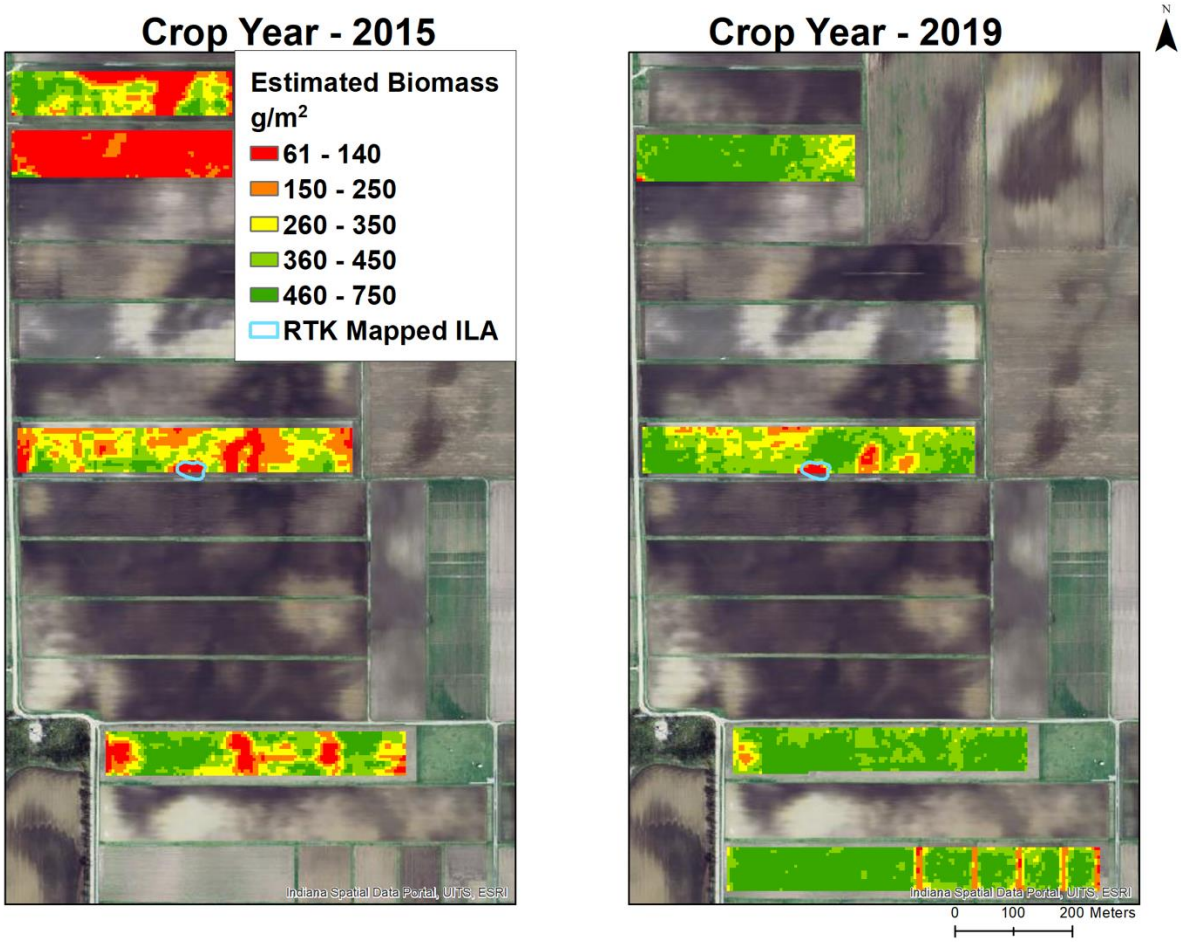

Figure 5.5: Comparison of RapidEye biomass (g/m^2) between crop years 2015 and 2019. Low estimates of biomass (61-140 g/m^2) are associated with observed ILA, mapped using an RTK. The 2015 crop year shows more extensive damage to soybean at early reproductive stages from excess water.

5.3.2 Percent of expected yield

The percent of expected yield from RapidEye is calculated for each field and compared with the observed relative yield calculated from the yield monitor data between crop years 2015 and 2019. The comparison between RapidEye and observed relative yield for all years is shown in Figure 5.6. Overall, the RapidEye relative yield was found to be in agreement with the observed with a calculated percent bias and mean absolute error of -4% and 6%, respectively. The RapidEye and observed relative yield values follow the 1:1 line closer for values less than 100% with a PBIAS and MAE of -2% and 2%, respectively (Figure 5.6). For predicted and observed relative yields greater than 100%, the scatter increases with an increase in PBIAS and MAE of -8% and 9%,

respectively. Predicted values capture the range of observed over multiple growing seasons, however there is an underprediction for higher estimates of relative yield (Figure 5.6).

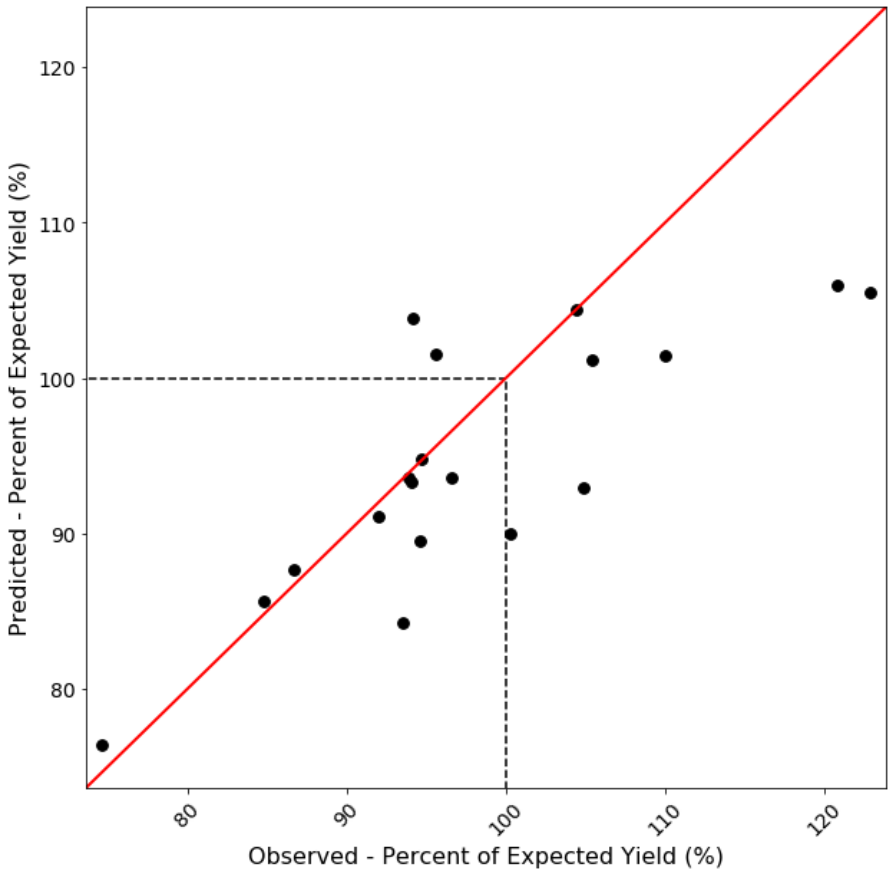

Figure 5.6: Comparison between observed and predicted percent of expected yield (%) from RapidEye (RapidEye expected yield) for all fields of interest between 2015 and 2019. The percent bias and mean absolute error are -4% and 6%, respectively.

The RapidEye relative yield is compared between all bulk soybean fields in crop years 2015 and 2019 (Figure 5.7), where 2015 was wetter than 2019. The RapidEye relative yield is lower in fields for the 2015 crop year compared to the 2019 crop year where the average percent relative yield is 83% versus 92%. The low estimates (< 80%) from RapidEye coincide with areas where ILA has been mapped with an RTK, which can be seen in similar fields for both years, though the inundation in 2015 is more prevalent. The areas susceptible to ILA and mapped with the RTK are found to have a reduction in yield by as much as 25% (Figure 5.7). The RapidEye expected yield indicates that fields in 2015 are severely impacted by ILA, with a total of 5 ha (12 ac) projected to

reach less than 80% of their potential. On the other hand, the impacts of ILA are less severe in 2019, with only 0.4 ha (1 ac) projected to fall below 80%. The areas with low relative yield occur primarily in areas within the field where ILA was mapped in 2018 and which were also observed to experience inundation in 2015 and 2019 (Figure 5.7). Overall, this analysis indicates that the RapidEye relative yield provides an accurate assessment of the projected yield over multiple growing seasons.

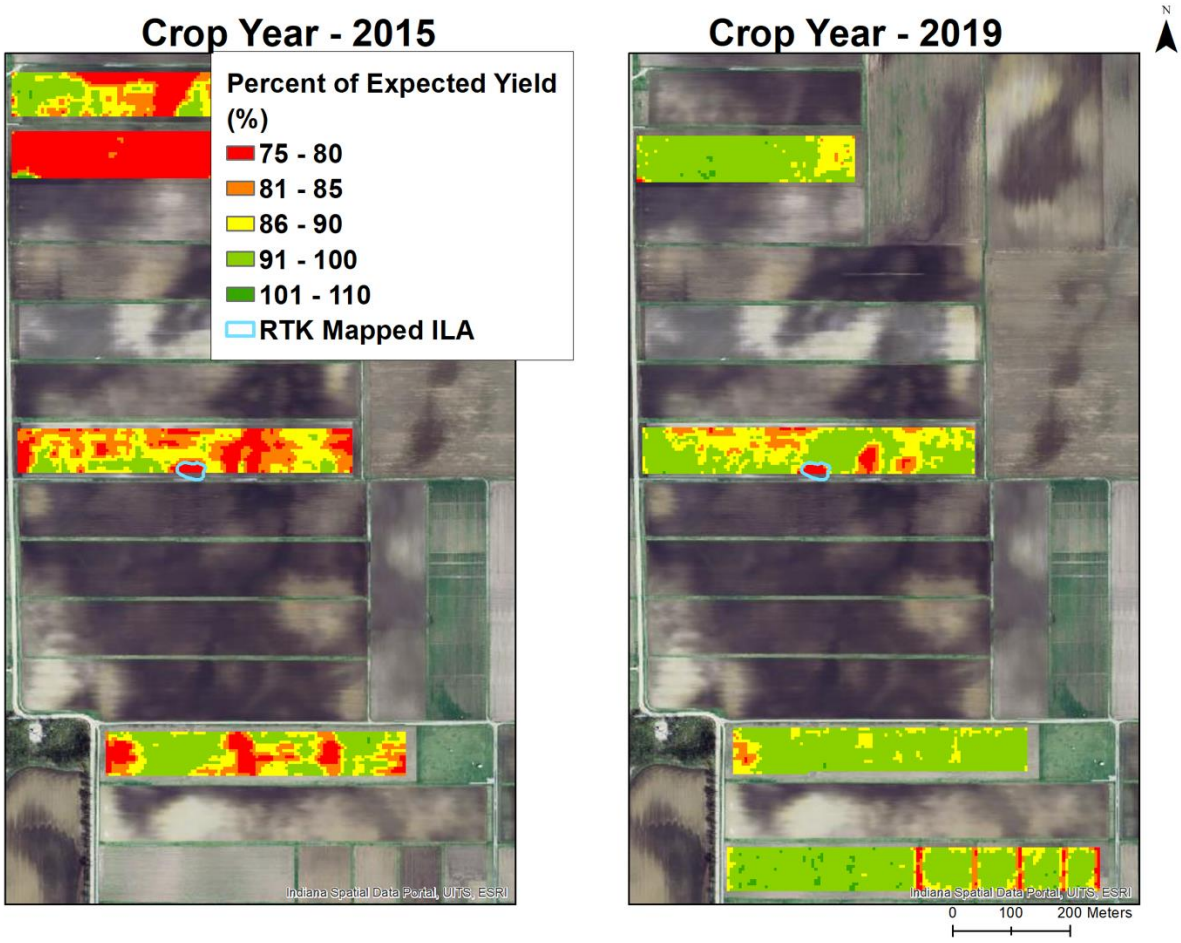

Figure 5.7: Field comparison of RapidEye expected yield between crop years 2015 and 2019. Soybean yield susceptible to ILA has the potential to have a 25% lower expected yield compared to areas that are not at risk of in-field flooding. ILA was mapped with an RTK, outlined in blue.

The influences of water availability on yield are shown by year in Figure 5.8, where the average yield is plotted with the contributing yield decline and yield gain. The range in average yield decline is from 0 kg/ha to 550 kg/ha, whereas the range in average yield gain is from 0 kg/ha to

150 kg/ha. As shown in Figure 5.8, water availability can cause yield decline and gain which impacts the average yield. For instance, the largest contributing yield decline occurs in 2015 with a value of approximately 550 kg/ha in the areas of negative yield impact, followed by crop years 2016 and 2019 with values of 250 kg/ha and 280 kg/ha, respectively. The yield decline in 2015 coincides with the lowest average yield in the period of analysis with a value of 3300 kg/ha and is the wettest year in the period of analysis. Whereas crop year 2016 is the driest in the period of analysis and has the second lowest average yield at 3600 kg/ha. The largest contributing yield gain occurs in 2017 with a value of approximately 150 kg/ha, followed by 140 kg/ha in 2018. The yield gains in 2015, 2016 and 2019 are negligible. The yield gains in crop years 2017 and 2018 are associated with the highest yields with values 4300 kg/ha and 3900 kg/ha, respectively.

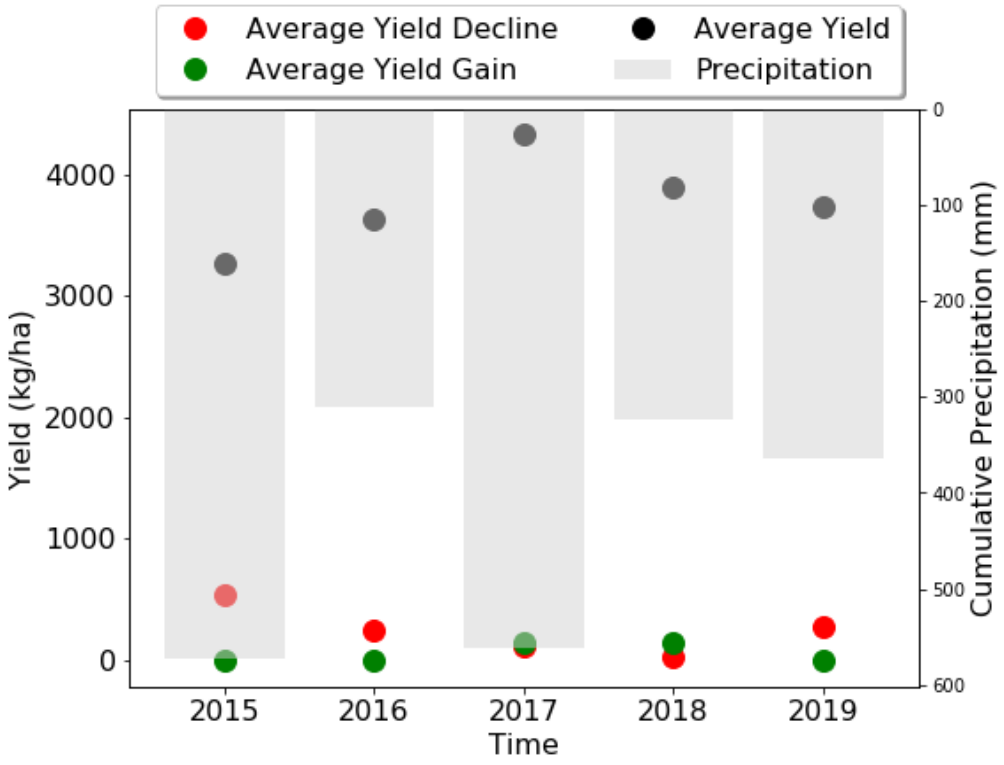

Figure 5.8: The average decline (red) and gain (green) in yield (kg/ha) relative to the average yield (black) with cumulative precipitation (mm) between April 1st and July 15th from crop years 2015 to 2019. Water availability (too much or too little water) causes increases in yield decline, such as in 2015, 2016 and 2019 and influences the average yield. Water availability can also provide optimal growing conditions to increase yield such as crop years 2017 and 2018.

5.4 Discussion

In this study we demonstrate the capabilities of leveraging low-cost UASs to design models at the field scale and apply the model over multiple years (2015-2019) and larger areas using satellite imagery from RapidEye. Previous research emphasizes the importance of matching spectral characteristics and temporal resolution to compliment the use of UAS and satellite imagery (Dash et al., 2018). RapidEye is selected in our study, because of its spectral characteristics as well as high temporal and spatial resolution. The image bands in the RapidEye data are similar to the bands on the Parrot Sequoia, the multispectral camera used to collect our UAS data. The high spatial and temporal resolution of RapidEye increases the opportunity to obtain observations at critical stages of soybean development and in-situ sampling. The high temporal resolution allows for cloud free retrievals between the R4-R6 stages from 2015 to 2019. The RapidEye imagery also provides the high spatial resolution (5 m) imagery needed in order to estimate parameters and develop the model for RapidEye biomass over the RUE experiment. The RapidEye biomass is developed from the UAS biomass model (Smith et al., 2020), where both models are tested at the RUE experiment. Results show that the UAS biomass model is also applicable to high resolution satellite imagery, such as RapidEye, where RapidEye biomass shows low bias and error with in-situ data from the calculated statistics. RapidEye biomass is also estimated at ACRE fields during early reproductive stages. Gao et al. (2018) used satellite imagery to compare calculated vegetation metrics with yield, and the results from their study also suggest vegetation metrics at early reproductive stages have stronger correlations with yield. In this study, the RapidEye biomass also has signification correlation with yield (Figure 5.4). Results of the RapidEye biomass demonstrate the ability to develop and transfer crop models across sites which are sensitive to the impacts of ILA.

We also use the UAS relative yield developed by Smith et al. (2020) and apply the model to RapidEye imagery to estimate RapidEye relative yield. Our research shows that the estimation and comparison of the RapidEye relative yield with the observed relative yield is a viable approach to quantitatively assess soybean development from excess water at early reproductive stages. Previous studies have used vegetation indices such as NDVI or the disaster vegetation damage index (DVDI) to assess crop damage from inundation (Di et al., 2018; Rahman et al., 2020; Shrestha et al., 2013). Rahman et al. (2020) note a limitation with providing crop loss assessments

as indices in that they do not incorporate yield information which may be of importance when reporting crop damage. In this study, yield data are available to provide a quantitative assessment of relative yield impacts based on biomass estiamtions from early reproductive stages. The UAS and RapidEye relative yield models have been tested for use with UAS and high-resolution satellite imagery that have similar bands. By incorporating the fractional biomass into the model, remote sensing platforms that have different spectral ranges and spatial resolutions can be used. The comparison of the observed and RapidEye relative yield shows strong correlation with low bias. However, prediction of relative yield greater than 100% shows an increase in bias. The increase in bias is due to limitations in the model estimate where the maximum yield potential is 110%. Further research is needed to determine if more data is needed to increase the range and improve the model estimate.

Few studies have evaluated the transferability of developed models from high resolution UAS data for application with satellite data. Dash et al. (2018) describes the sensitivity differences between the RapidEye and a UAS camera, the MicaSense Red Edge 3 camera, which has similar bands as the RapidEye and Parrot Sequoia. The results of the study show that the RapidEye is less sensitive than the UAS camera. Further research is also needed to test the model using other UAS and satellite platforms. Previous studies have used MODIS to analyze impacts of inundation on crop development (Di et al., 2017; Shrestha et al., 2013). MODIS may be of future use or PlanetScope, which have similar bands needed to test the models over larger areas with a high temporal resolution. The developed models from this study have low bias compared to observed data and demonstrate the potential to assess excess water impacts on soybean at early development stages at varying scales.

In our study, we provide models to estimate biomass and percent of expected yield assessments at the early reproductive stages with RapidEye, from R4 to R6. The results from 2015 to 2019 show that low estimates of biomass and relative yield correspond to mapped observations of ILA which can reduce the relative yield by as much as 25%. The higher degree of damage from excess water stress estimated in 2015 also corresponds with reports that as much as 5% of the corn and soybean crops in Indiana were damaged by excess rainfall that caused approximately $300 million in crop damage (Pack, 2015). Di et al. (2017) discuss the need for early recovery assessments of crops

impacted by inundation. In the period of analysis, the 2015 and 2017 crop years have the highest cumulative precipitation between April 1st and July 15th at 573 mm and 561 mm, respectively. Though the cumulative differences are small, the timing of the precipitation is critical and can affect crop development. In June of 2015, the cumulative precipitation was 255 mm, while in June of 2017 the cumulative precipitation was 140 mm. The average yield for all fields of interest in the 2015 and 2017 crop years were 3270 kg/ha and 4327 kg/ha, respectively, while the average biomass in 2015 and 2017 are 259 g/m^2 and 642 g/m^2, respectively. Though other contributing factors can impact yield, the difference in cumulative precipitation of 115 mm within the short time window from June 1st to June 30th results in differences in average yield and inverse impacts from excess water as shown in Figure 5.8, where excess water causes noticeable yield decline in 2015 but contributes to slightly more yield gain in 2017. Rahman et al. (2020) discuss the resilience of crops from inundation. Our results show that excess water typically results in yield loss and in instances where there is an increase in yield, the gain is not substantial. The instance of yield gain may be due to soil moisture conditions which allow the soybean to thrive. Similar results are reported at the plot scale by Smith et al. (2020). The impacts of excess water on yield decline also shed light on the importance of subsurface drainage and the potential for remote sensing derived products such as estimated biomass or percent of expected yield to monitor drainage efficiency by analyzing the crop status over multiple growing seasons. A previous study used vegetation indices to analyze crop development under different control drainage practices (Cicek et al., 2010). In this study, the observed ILA is typically in isolated locations and is associated with low RapidEye biomass and relative yield. The remote sensing products presented in this study can be used to identify fields with persistent ILA as shown in Figure 5.9, where the percent of expected yield is mapped for a soybean field at early reproductive stages between 2015 and 2019. Figure 5.9 shows that ILA occurs predominantly in the center of the field, where visual and mapped observations of ILA correspond to the low values of percent of expected yield. By identifying fields or locations within fields with a persistent decrease in expected yield from ILA over multiple growing seasons, agricultural producers can improve management decisions and determine whether to install additional subsurface drainage throughout the field or in specific locations.

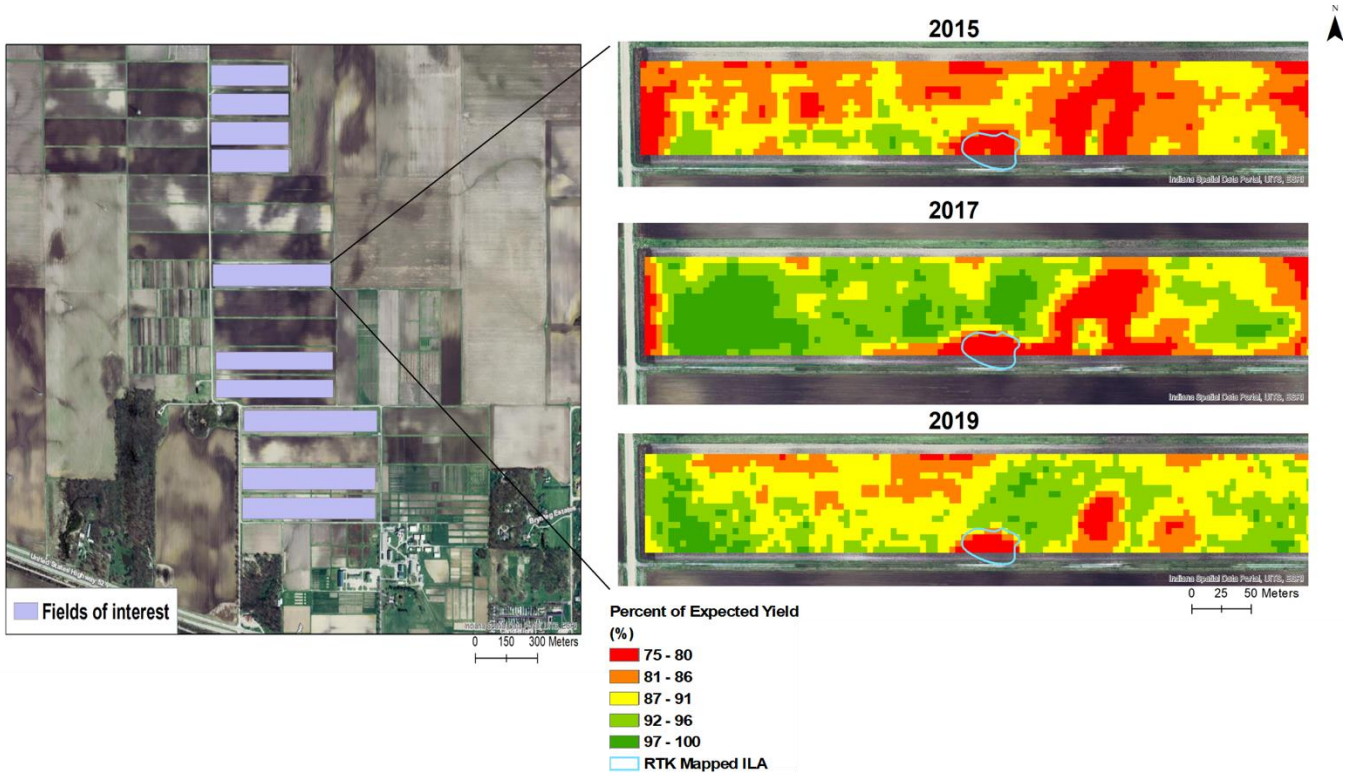

Figure 5.9: Example of identified field with persistent inundated land area over multiple crop years associated with a decrease in percent of expected yield. Observed ILA was mapped with an RTK and is associated with expected yield ranging from 75% to 80%. This information can help agricultural producers improve management decisions.

Johnson (2014) and Di et al. (2017) discuss the importance of providing crop damage assessments and yield information to inform stakeholders and support their decisions related to agricultural economics and farm management. In this study, we provide maps of estimated biomass and percent of expected yield that identify areas impacted by ILA. This information can help stakeholders identify risks and increase transparency between insurance companies and policy holders. The biomass and relative yield maps may also support work needed in the annual Objective Yield Survey for soybean. For soybean, the Objective Yield Survey uses trained enumerators to manually collect hundreds of samples from randomly selected fields from the Agricultural Yield Survey in late July and continue monthly inspections until harvest. Di et al. (2017) notes the limitations of the field survey such as costs and time required to complete sampling. Incorporating the use of remotely sensed measurements to estimate biomass and relative yield may help reduce costs and time intensive processes as well as provide supporting data needed for yield forecasts. Future

research should investigate incorporating estimates of soybean yield potential from remotely sensed observations to improve forecasts.

5.5 Conclusion

In this study, we investigate the utility and applications of low-cost UASs to design models at the field scale and applied over larger areas using complimentary measurements from RapidEye to estimate biomass and percent of expected yield. Results of the study suggest the following:

1. A biomass model developed from UAS imagery is applicable for high resolution satellite imagery such as RapidEye. The developed RapidEye biomass model at early reproductive stages, between R4-R6 show agreement with in-situ observations (n=868) with low percent bias and root mean square error of <0.1% and 69 g/m^2, respectively.
2. RapidEye relative yield when compared with observed relative yield shows a strong relationship with a calculated percent bias and mean absolute error of -4% and 6%, respectively. Though the model underpredicts relative yield greater than 100%, overall, the model captures the range of relative yield.
3. RapidEye biomass and relative yield correspond with observations of inundated land area. Local depressions susceptible to ILA can impact relative yield by as much as 25%. However, some areas within the fields may have water availability conditions that can cause yield gains. Mapping and providing assessments of predicted relative yield at early reproductive stages is useful for stakeholders.

Readily available products are needed to inform stakeholders of impacts to crop development from inundated land area. Remotely sensed observations can be used to provide early indications of soybean development and quantify potential impacts on yield. In this study, we leverage the utility of low-cost UASs and available in-situ data to develop models at the field scale for application over larger areas with satellite imagery. The results demonstrate the transferability of models across sites and between sensors with the accuracy needed to quantify the spatiotemporal impacts of excess water at early reproductive stages.

5.6 References

Basso, B., & Liu, L. (2019). Seasonal crop yield forecast: Methods, applications, and accuracies. In *Advances in Agronomy* (1st ed., Vol. 154, pp. 201–255). Elsevier Inc. https://doi.org/10.1016/bs.agron.2018.11.002

Chan, S., Bindlish, R., Hunt, R., Jackson, T., & Kimball, J. (2013). Ancillary Data Report: Vegetation Water Content, (SMAP Science Document 047), 1–15. Retrieved from smap.jpl.nasa.gov

Cicek, H., Sunohara, M., Wilkes, G., McNairn, H., Pick, F., Topp, E., & Lapen, D. R. (2010). Using vegetation indices from satellite remote sensing to assess corn and soybean response to controlled tile drainage. *Agricultural Water Management*, *98*(2), 261–270. https://doi.org/10.1016/j.agwat.2010.08.019

Dado, W. T., Deines, J. M., Patel, R., Liang, S. Z., & Lobell, D. B. (2020). High-resolution soybean yield mapping across the us midwest using subfield harvester data. *Remote Sensing*, *12*(21), 1–22. https://doi.org/10.3390/rs12213471

Dash, J. P., Pearse, G. D., & Watt, M. S. (2018). UAV multispectral imagery can complement satellite data for monitoring forest health. *Remote Sensing*, *10*(8), 1–22. https://doi.org/10.3390/rs10081216

Desmond, E., Barkle, G. F., & Shwab, G. O. (1985). Soybean Yield Response to Excess Water. In *1985 Winter Meeting American Society of Agricultural Engineers* (pp. 1–12).

Di, L., Yu, E. G., Kang, L., Shrestha, R., & BAI, Y. qi. (2017). RF-CLASS: A remote-sensing-based flood crop loss assessment cyber-service system for supporting crop statistics and insurance decision-making. *Journal of Integrative Agriculture*, *16*(2), 408–423. https://doi.org/10.1016/S2095-3119(16)61499-5

Di, L., Yu, E., Shrestha, R., & Lin, L. (2018). DVDI: A new remotely sensed index for measuring vegetation damage caused by natural disasters. *International Geoscience and Remote Sensing Symposium (IGARSS)*, *2018–July*(3), 9067–9069. https://doi.org/10.1109/IGARSS.2018.8518022

Fehr, W. R., Caviness, C. E., Burmood, D. T., & Pennington, J. S. (1971). Stage of Development Descriptions for Soybeans, Glycine Max (L.) Merrill 1. *Crop Science*, *11*(6), 929–931. https://doi.org/10.2135/cropsci1971.0011183x001100060051x

Gao, F., Anderson, M., Daughtry, C., & Johnson, D. (2018). Assessing the variability of corn and soybean yields in central Iowa using high spatiotemporal resolution multi-satellite imagery. *Remote Sensing*, *10*(9). https://doi.org/10.3390/rs10091489

Johnson, D. M. (2014). An assessment of pre- and within-season remotely sensed variables for forecasting corn and soybean yields in the United States. *Remote Sensing of Environment*, *141*, 116–128. https://doi.org/10.1016/j.rse.2013.10.027

Kross, A., McNairn, H., Lapen, D., Sunohara, M., & Champagne, C. (2015). Assessment of RapidEye vegetation indices for estimation of leaf area index and biomass in corn and soybean crops. *International Journal of Applied Earth Observation and Geoinformation*, *34*(1), 235–248. https://doi.org/10.1016/j.jag.2014.08.002

Licht, M., Abendroth, L. J., Elmore, R. W., Boyer, M. J., & Marlay, S. K. (2011). *Corn Growth and Development*. Retrieved from https://store.extension.iastate.edu/product/Corn-Growth-and-Development

Liu, J., Pattey, E., Miller, J. R., McNairn, H., Smith, A., & Hu, B. (2010). Estimating crop stresses, aboveground dry biomass and yield of corn using multi-temporal optical data combined with a radiation use efficiency model. *Remote Sensing of Environment*, *114*(6), 1167–1177. https://doi.org/10.1016/j.rse.2010.01.004

Lobell, D. B. (2013). The use of satellite data for crop yield gap analysis. *Field Crops Research*, *143*, 56–64. https://doi.org/10.1016/j.fcr.2012.08.008

Lobell, D. B., Thau, D., Seifert, C., Engle, E., & Little, B. (2015). A scalable satellite-based crop yield mapper. *Remote Sensing of Environment*, *164*, 324–333. https://doi.org/10.1016/j.rse.2015.04.021

Ma, B. L., Dwyer, L. M., Costa, C., Cober, E. R., & Morrison, M. J. (2001). Early Prediction of Soybean Yield from Canopy Reflectance Measurements. *Agron. J*, (93), 1227–1233. https://doi.org/10.2134/agronj2001.1227

Maimaitijiang, M., Sagan, V., Sidike, P., Hartling, S., Esposito, F., & Fritschi, F. B. (2020). Soybean yield prediction from UAV using multimodal data fusion and deep learning. *Remote Sensing of Environment*, *237*(December 2019), 111599. https://doi.org/10.1016/j.rse.2019.111599

Mulla, D. J. (2013). Twenty five years of remote sensing in precision agriculture: Key advances and remaining knowledge gaps. *Biosystems Engineering*, *114*(4), 358–371. https://doi.org/10.1016/j.biosystemseng.2012.08.009

Rahman, M. S., & Di, L. (2020). A systematic review on case studies of remote-sensing-based flood crop loss assessment. *Agriculture (Switzerland)*, *10*(4). https://doi.org/10.3390/agriculture10040131

Shrestha, R., Shao, Y., Di, L., Kang, L., Yu, G., & Zhang, B. (2013). Detection of flood and its impact on crops using NDVI - Corn Case. In *2013 2nd International Conference on Agro-Geoinformatics: Information for Sustainable Agriculture, Agro-Geoinformatics 2013* (pp. 200–204). IEEE. https://doi.org/10.1109/Argo-Geoinformatics.2013.6621907

Smith, S. D., Bowling, L. C., Rainey, K. M., & Cherkauer, K. A. (2020). Quantifying Impacts of Excess Water Stress at Early Reproductive Stages of Soybean from Unmanned Aerial Systems. *Agricultural and Forest Meteorology*, in review.

6. CONCLUSIONS AND FUTURE WORK

6.1 Summary

The overall goal of this work was to increase understanding of the impacts of inundated land area on streamflow and crop development in the Upper Midwestern United States. To increase this understanding, the following research objectives were established, to: (1) Parameterize the representation of surface ponding in the VIC model using remote sensing estimates of ILA, (2) Evaluate seasonal trends in flood magnitude and frequency in the Red River of the North, (3) Quantify the impacts of excess water stress on soybean development based on proximal remote sensing from unmanned aircraft systems (UASs) and (4) Quantify the impacts of excess water stress on soybean development over larger areas using satellite imagery with models developed at the field scale from UAS data.

To evaluate the impacts of ILA on streamflow, an inundated depth-area parameterization (IDA) was introduced in Chapter 2 to simulate the temporary storage of water on the land surface using a hydrologic model. The IDA parameterization can be routinely updated in hydrologic models using available discharge and remotely sensed data. The IDA parameterization was developed and tested using the VIC model in a subcatchment of the Red River basin which is dominated by agricultural land use and prone to ILA. The simulated ILA is satisfactory when compared to the observed ILA from the MODIS NRT Global Flood Mapping product with a percent bias -16% over the evaluation period. Simulated ILA and streamflow provide supporting evidence of the dominant runoff generation mechanisms during the winter-spring and summer-fall seasons. During the winter-spring the VSA concept and fill and spill are the dominant runoff generation mechanisms. For the VSA concept, ILA increases over the land surface due to low permeability from the soil-ice content restricting infiltration. For the fill and spill mechanism, simulated and observed ILA show a rise and fall of ILA after peak flow, where local depressions in low gradient areas contribute to runoff generation once depressions reach capacity following the peak flow event and continue to fill and spill. During the summer-fall, infiltration-excess overland is the dominant runoff generation mechanism, where ILA increases from runoff of excess precipitation

causing an increase in storage on the land surface, and ILA decreases rapidly as infiltration is no longer limited.

The ILA parameterization methodology was then extended to the larger Red River Basin using VIC model simulations to quantify the influence of ILA on flood occurrence and magnitude (Chapter 3). This is a region that has a known history of large flood events which have caused billions of dollars in damage and there is evidence that climate change is increasing the frequency of such events as well as increasing the likelihood of flood events occurring in the summer season. The results of the study show statistically significant increasing trends in summer flood magnitudes for all gaging stations evaluated in the Red River basin from the Mann-Kendall test. The occurrence of flood events is shifting from a unimodal structure to a bimodal structure with more floods occurring in the spring and summer seasons, specifically the months of April and June, respectively. There is no observed increase in flood occurrence during the month of May, while model simulations without ILA show increases in May flood frequency, which implies an increase in-field flooding may be mitigating flood potential. A reduced flood occurrence is simulated when representing ILA and is overpredicted when not representing ILA. Representing this in-field flooding is important to agricultural producers and their management decisions, where farmers in the Upper Midwest plant crops during the month of May which could be at risk of excess water stress. In addition, the study demonstrates the importance of representing ILA in hydrologic models, where the simulation of flood magnitude and occurrence are improved. When simulating ILA, flood frequency for the 50-year return period is 8% less than the observed compared to not representing ILA which is 23% more than the observed. The observed shift in peak flow occurrence is also captured in simulated streamflow when representing ILA. This study also highlights the increased occurrence of flooding (both observed and simulated) during the summer season, which leads directly to a need for better understanding of how inundation affects crop yields, which in turn leads directly to the research in the next chapter.

In Chapter 4, we evaluate the impacts of ILA on crop development, where models were developed to quantify the impacts of excess water stress on soybean biomass accumulation and yield at early reproductive stages using proximal remote sensing from UASs. The developed models used in-situ and remotely sensed data at the plot scale (23 m^2) to estimate biomass and percent of expected

yield between the development stages when pods are full (R4) to the development stage when the seed filling has begun (R5) at the field scale (2 ha). Topographic wetness index is used to compare plots more susceptible to ILA with replicate plots less susceptible to ILA, and mapped observations of ILA are used to validate model estimates. Estimated biomass was accurate when compared to observed biomass with a percent bias and root mean square error of 0.8% and 72 g/m^2, respectively. The estimated biomass is sensitive to excess water stress with distinguishable differences identified between the R4-R6 development stages. The percent of expected yield less than 90% corresponds with mapped observations of in-field flooding and high TWI. These results demonstrate the increased potential to provide stakeholders with early estimates of the potential yield impacts of excess water stress on soybean using low-cost UASs and a high-throughput data processing pipeline.

The applicability of models developed using field scale ground reference and remote sensing data for the estimation of biomass and prediction of final yield at larger scales using satellite remote sensing imagery was evaluated in Chapter 5. The UAS models (UAS biomass and percent of expected yield) described in Chapter 4 were developed using in-situ biomass and yield data along with UAS multi-spectral imagery from a radiation use efficiency (RUE) experiment at a nearby research farm in west-central Indiana. The UAS models were applied to satellite imagery from RapidEye to estimate biomass (RapidEye biomass) and percent of expected yield attained (RapidEye expected yield) over larger areas at the Agronomy Center for Research and Education (ACRE) from crop years 2015 to 2019. Parameters to estimate RapidEye biomass were fitted using RapidEye imagery and in-situ biomass collected from the RUE experiment. At RUE, RapidEye biomass has a percent bias of 0.1% and root mean square error of 69 g/m^2. At ACRE the field average RapidEye biomass has significant correlation with the field average yield (kg/ha). At ACRE, the UAS expected yield model was applied using RapidEye biomass inputs to estimate the crop yield as a percent of expected yield (RapidEye expected yield). At ACRE, the RapidEye expected yield has a strong relationship with observed expected yield where the calculated percent bias and mean absolute error are -4% and 6%, respectively. The experiment illustrates the potential of leveraging the utility of low-cost UASs to develop biomass and yield models at the field scale for application with satellite imagery in order to assess the impacts of excess water over multiple fields and growing seasons. The developed products can be used to support stakeholders by

providing early assessments of soybean development associated with impacts from ILA, and to identify infrastructure needs to address the long-term impacts of in-field ponding on crop yields and support NASS by reducing the labor and costs to conduct large surveys.

6.2 Conclusions

Four hypotheses were proposed in Chapter 1. The responses to each hypothesis statement are summarized below:

1. Estimates of flood magnitude will be reduced by simulating land inundation processes, because surface depressions play a critical role in the volume of water reaching the channel in large river basins.

Confirmed. Representation of inundated land area within the VIC model reduced the magnitude of the simulated 50-year flood by 31% in the Red River basin. The above hypothesis was tested in the Buffalo River, a subcatchment of the Red River of the North basin and expanded the tested hypothesis to the Red River basin. The study in the Buffalo River showed, by representing inundated land area in the VIC model, the magnitude of peak flows was reduced, and simulated goodness of fit statistics were improved when compared to alternative scenarios. By not representing ILA simulated discharge had a tendency to overestimate high flow when compared to the observed discharge. Whereas, by representing ILA, simulated streamflow during high and low flow periods was improved when compared to the observed discharge. The analysis in the Red River showed that representing ILA improves the estimation of flood frequency, where the 50-year return period was 8% less than the observed compared to not representing ILA which was 23% more than the observed.

2. The seasonality of flood response has shifted in the Red River basin due to a changing climate but this shift has been mitigated by the influence of ILA.

Confirmed. Without representation of inundated land area within the VIC model, the occurrence of simulated May and June flood events was overestimated by 87%. The study in the Red River basin showed statistically significant increasing trends in summer peak flow events for all evaluated gaging stations using the Mann-Kendall test. There is no significant trend in the

magnitude of spring flood events that are associated with snow melt. In addition, a detected shift in peak flow occurrence was identified in the observed discharge data during the period of analysis. The detected shift was from a unimodal structure to a bimodal structure, where floods were occurring in the spring and summer seasons versus just in the spring season. The shift was also represented in simulated discharge when representing ILA. The reduced flood occurrence in May implies an increase of in-field flooding and is simulated when representing ILA. The in-field flooding has the potential to impact crop yield from excess water stress at early growth stages.

3. The impact of excess water stress on soybean yield is related to the above-ground biomass sensed from a UAS platform during early growth stages.

Confirmed. Soybean yield decline or gain associated with areas of in-field flood or high topographic wetness index were estimated with an overall percent bias 0.8% based on above-ground biomass for the R4-R5 growth stage. The above hypothesis was testing at research farm in west-central Indiana, where soybean experienced inundation during the growing season. In this study, proximal remote sensing was used to estimate above-ground biomass (g/m^2) and percent of expected yield (%). Results of the study showed that estimated above-ground biomass at the R4-R5 stage had low percent bias and root means square error of 0.8% and 72 g/m^2, respectively for varying genetic classes. In addition, decreased estimates of biomass and percent of expected yield were associated with observations of in-field flooding and high topographic wetness index.

4. Quantification of above-ground biomass by spaceborne platforms can quantify impacts to crop yield at sub-field scales.

Confirmed. Soybean yield decline and gain at sub-field scales were estimated with an overall percent bias of less than 0.1% based on above-ground biomass for the R4-R6 growth stage. The above hypothesis was tested at two research farms in west-central Indiana, where the impacts of excess water on soybean yield were analyzed by using low-cost UASs to design models at the field scale and applied to satellite imagery from RapidEye over larger areas from 2015 to 2019. The developed models were the RapidEye biomass and expected yield to estimate biomass (g/m^2) and percent of expected yield (%), respectively. Results of the study showed the RapidEye biomass

model at early reproductive stages, between R4-R6 show agreement with measured biomass with low percent bias and root mean square error of <0.1% and 69 g/m2, respectively. RapidEye expected yield when compared with observed expected yield had a calculated percent bias and mean absolute error of -4% and 6%, respectively. Decreased RapidEye estimates were associated with mapped observations of ILA and increased TWI, local depressions susceptible to ILA can impact expected yield by as much as 25%.

6.3 Future work

This study quantified the impacts of ILA on streamflow and crop development in the Red River basin and Indiana, respectively. Both agricultural locations are in the Upper Midwest, which means that we can link methods and findings related to ILA from both locations to better understand the potential risks and costs a changing climate has on its agricultural stakeholders. The results of the Red River suggest an increase in-field flooding in May. The techniques from Chapter 4 and 5 can be used to quantify the impacts of excess water on crop development in the Red River basin using remote sensing from UASs or satellites.

The IDA parameterization was developed using remotely sensed observations from the MODIS NRT Global Flood Mapping product, where high cloud coverage (>30%) limited retrievals of inundation extent during peak flow. Future work should consider the use of active and passive sensors to estimate ILA from future or ongoing missions such as Surface Water Ocean Topography (SWOT) or Soil Moisture Active Passive (SMAP). The microwave bands can penetrate clouds and be used to measure either the backscatter from active sensors or emitted microwave radiation from passive microwave radiometers which are sensitive to inundation on the land surface. Tests for trends in ILA over time were not calculated in this work. With continued monitoring and a longer time series of ILA, tests for trend could be used to better quantify the economic costs of in-field flooding over time, and help farmers make decisions about needed drainage infrastructure.

The impacts of ILA on soybean development were evaluated at ACRE over a five-year period. The ACRE fields provide future opportunities for the continuation of monitoring and quantifying the impacts of excess water on crop development from UAS and satellite platforms and the opportunity to validate results with continued collection of in-situ data and mapping of ILA. The

crop models developed and validated in this work, were only tested on soybean using observed biomass and yield data as reference data to validate the remotely sensed estimates. Future work can test the crop models on other crops to analyze the impacts of excess water on crop development. Field monitoring can be continued by collection of soybean and corn data such as biomass samples at critical development stages and yield data after harvesting. The collected data can be used to develop and improve other crop models that may need to consider different genotypes. In addition, monitoring can be continued through measuring soil moisture and temperature and water table depth within ACRE fields which could help better understand crop water stress indices at ACRE.

APPENDIX A. SOURCE CODE REPOSITORIES

The links below provide access to GitHub repositories used for the work.

Repository for lake and wetland algorithm in the VIC model. Used for generating the inundated depth-area parameterization.
https://github.itap.purdue.edu/PHIGOrganization/VIC-LakeWetlandParameters

Repository for Land Information Systems (LIS) – VIC with lake and wetland algorithm.
https://github.itap.purdue.edu/PHIGOrganization/LIS-VIC_Purdue

Repository for Crop Image Extraction (CIE) and Vegetation Index Derivation (VID).
https://github.itap.purdue.edu/PHIGOrganization/CIE-and-VID

APPENDIX B. ARCHIVED DATA

The links below provide links to archived data collected throughout the study.

Monitored soil moisture and temperature data at the Agronomy Center for Research and Education (ACRE).
https://purr.purdue.edu/publications/3313/2

UAS imagery (RGB) from research farm in west-central Indiana.
https://purr.purdue.edu/publications/3319/1

Field images from time lapse camera from field at ACRE.
/fortress/group/phig/student backups/sdsmith/phd/crops/ACRE_Field_Images/